ÉCOLE DE TECHNOLOGIE SUPÉRIEURE
UNIVERSITÉ DU QUÉBEC

MANUSCRIPT-BASED THESIS
PRESENTED TO
ÉCOLE DE TECHNOLOGIE SUPÉRIEURE

IN PARTIAL FULFILLEMENT OF THE REQUIREMENTS FOR
THE DEGREE OF DOCTOR OF PHILOSOPHY
Ph. D.

BY
Morteza NAJJARI

CHARACTERIZATION OF EDGE-CONTACT INFLUENCE ON TRIDIMENSIONAL ELASTOHYDRODYNAMIC FILM SHAPE, PRESSURE, STRESS AND TEMPERATURE DISTRIBUTIONS

MONTRÉAL, SEPTEMBER 26 2014

BOARD OF EXAMINERS

THIS THESIS HAS BEEN EVALUATED

BY THE FOLLOWING BOARD OF EXAMINERS

Mr. Raynald Guilbault, Thesis Supervisor
Mechanical Engineering Department at École de technologie supérieure

Mrs. Natalia Nuño, President of the Board of Examiners
Automated Production Engineering Department at École de technologie supérieure

Mr. Hakim Bouzid, Member of the jury
Mechanical Engineering Department at École de technologie supérieure

Mr. Olivier Bonneau, External Evaluator
Mechanical Engineering Department at Université de Poitiers

THIS THESIS WAS PRENSENTED AND DEFENDED

IN THE PRESENCE OF A BOARD OF EXAMINERS AND PUBLIC

SEPTEMBER 22 2014

AT ÉCOLE DE TECHNOLOGIE SUPÉRIEURE

ACKNOWLEDGMENT

I would like to offer my sincere gratitude to my thesis supervisor, Raynald Guilbault, for his technical, financial and moral support throughout these years. His excellent advice, support and friendship have been invaluable on both academic and personal level, for which I am extremely grateful.

My special thanks go to my family for their strong support, encouragement and love which were essential for completion of my PhD program. Despite the geographical distance, you were always nearby.

I would like to thank the jury members who evaluated my thesis; Prof. Natalia Nuño (École de technologie supérieure), Prof. Hakim Bouzid (École de technologie supérieure), Prof. Olivier Bonneau (Université de Poitiers). Your comments were constructive and reflect the fact that always there is room for improvement.

CHARACTERIZATION OF EDGE-CONTACT INFLUENCE ON TRIDIMENSIONAL ELASTOHYDRODYNAMIC FILM SHAPE, PRESSURE, STRESS AND TEMPERATURE DISTRIBUTIONS

Morteza NAJJARI

RÉSUMÉ

Ce projet de doctorat étudie l'influence du contact de bord sur la pression, l'épaisseur du film de lubrifiant, la température et la distribution des contraintes des contacts en ligne de dimension finie sous le régime de lubrification élastohydrodynamique (LEH). Ce type de contact représente une source fréquente de problèmes dans les structures d'ingénierie telles que les engrenages, les cames et les roulements, puisque les surfaces de contact non conformes dans ces structures subissent une pression intense pendant le transfert de charge par des zones de contact relativement petites. De plus, ils provoquent des zones de concentration de contraintes aux extrémités. En conséquence, une modification de profil devient nécessaire.

La présente étude analyse l'influence des frontières libres sur les caractéristiques du régime LEH pour des contacts en ligne de dimension finie. La première phase de la recherche développe un modèle numérique général 3D du régime LEH incluant les effets thermiques et non-newtonien du problème. Une méthode semi-analytique (SAM) basée sur la théorie de Boussinesq pour des espaces semi-infinis est combinée à un procédé de correction des frontières libres pour fournir une description rapide et précise des conditions de contact de bord. Une expansion modifiée en différences finies du terme de Couette contenu dans l'équation de Reynolds garantit la stabilité du calcul, tandis que l'expression Carreau définit la réponse de fluidification par cisaillement du lubrifiant. L'impact des frontières libres sur la distribution tridimensionnelle des contraintes est également étudié par l'extension de la procédure de correction de frontière libre pour évaluer les niveaux de contraintes de surface et sous la surface en utilisant SAM. Les données sur la répartition des contraintes dérivées de cette procédure sont alors mis en contraste avec les résultats de la méthode des éléments finis (MEF) en utilisant une comparaison factorielle à deux niveaux. Trois facteurs sans dimension à savoir le minceur du contact, rapport de longueur de contact et la charge sont examinés. La comparaison montre que le nouveau modèle développé dans cette thèse fournit un haut niveau de précision dans l'évaluation des distributions de contraintes, tout en calculant plus de 125 fois plus rapide que des simulations MEF. Ce modèle puissant est ensuite utilisé pour étudier et établir l'influence de différentes modifications de profils de rouleau sur la forme de film LEH, les distributions de pression et la température. En se basant sur une série d'analyses détaillées des différentes corrections de profil de rouleau, il est constaté qu'un grand rayon couronnant combiné avec des coins arrondis fournit l'ajustement de profil le plus efficace.

Dans la dernière étape de cette étude, ce modèle nouvellement développé est combiné avec une optimisation par essaim de particules (PSO) multi-objectif pour arriver aux formules établissant les rayons du couronnement et du coin arrondi, qui peuvent être appliquées à la conception rapide des rouleaux optimaux. Les formules prennent en compte trois facteurs sans dimension - minceur, charge, et la viscosité du lubrifiant - et les coefficients pour les formules sont dérivés à partir des résultats PSO en utilisant une conception factorielle à cinq niveaux. En optimisant simultanément trois fonctions objectives - l'uniformité de la pression de contact, la stabilité de l'épaisseur du film, et la capacité de charge maximale - les prédictions de ces formules garantissent des modifications optimales de profil. Cette étude contribue à la compréhension de l'influence du bord sur les caractéristiques de LEH des contacts en ligne fini, tandis que propose un modèle robuste pour les corrections de profil axiales des problèmes de contact lubrifié.

Mots-clés: Lubrification Élastohydrodynamique, contact de bord, fluide non-newtonien, l'épaisseur du film, la pression, la température, la contrainte, optimisation, PSO.

CHARACTERIZATION OF EDGE-CONTACT INFLUENCE ON TRIDIMENSIONAL ELASTOHYDRODYNAMIC FILM SHAPE, PRESSURE, STRESS AND TEMPERATURE DISTRIBUTIONS

Morteza NAJJARI

ABSTRACT

This doctoral project investigates edge contact influence on pressure, lubricant film thickness, temperature, and stress distribution of finite line contacts under an elastohydrodynamic lubrication (EHL) regime. This type of contact represents a common source of problems in engineering structures such as gears, cams and roller bearings, since non-conforming contact surfaces in such structures undergo intense stresses while transferring loads through relatively small contact areas. Additionally, they induce stress concentration zones at their extremities; as a result, profile modification becomes necessary.

The present study investigates influence of free edges on EHL characteristics of finite line contacts. The initial stage of the research develops a 3D numerical model for the thermal, non-Newtonian EHL of general contact problems. A semi-analytical method (SAM), based on the Boussinesq half-space theory, is combined with a free boundary correction process to provide a fast and precise description of edge contact conditions. A modified finite difference expansion of the Couette term of the Reynolds equation guarantees computational stability, while the Carreau expression defines the shear-thinning response of the lubricant. Free boundary impact on tridimensional stress distribution is also investigated by extending the free-edge correction procedure to evaluate the levels of surface and subsurface stresses using SAM. The stress distribution data derived from this procedure are then contrasted with Finite Element Method (FEM) results using a two-level factorial comparison. Three dimensionless factors — contact slenderness, contact length ratio, and load — are examined. The comparison shows that the new model developed in this thesis provides a high level of precision in the evaluation of stress distributions, while computing more than 125 times faster than FEM simulations. This powerful model is then used to investigate and establish the influence of different roller profile modifications on EHL film shape, pressure and temperature distributions. Based on a series of detailed analyses of different roller profile corrections, it is found that a large radius crowning combined with rounding corners provides the most effective profile adjustment.

In the last step of this study, this newly developed model is combined with a multi-objective particle swarm optimization (PSO) to arrive at formulas establishing crowning and corner rounding radii, which can be applied to the rapid design of optimal rollers. The formulas take into account three dimensionless factors — slenderness, load, and lubricant viscosity — and coefficients for the formulas are derived from the PSO results using a five-level factorial design. By concurrently optimizing three objective functions — contact pressure uniformity, film thickness stability, and maximum load capacity — the predictions of these formulas guarantee optimal profile modifications. This study contributes to the understanding of edge influence on EHL characteristics of finite line contacts, while offering a robust model for axial profile corrections of lubricated contact problems.

Keywords: Elastohydrodynamic lubrication, edge-contact, non-Newtonian fluid, film-thickness, pressure, temperature, stress, optimization, PSO.

TABLE OF CONTENTS

Page

LIST OF TABLES

Page

LIST OF FIGURES

LIST OF SYMBOLS

a	half-length of a cell
b	half-width of a cell
C	half-width of Hertzian contact
c_p	specific heat of the fluid
c_{pa}	specific heat of body a
c_{pb}	specific heat of body b
c_1, c_2	Learning factors
D	Dimensionality of the problem
D_{eq}	Equivalent roller diameter
E	Young modulus
E'	equivalent modulus
$f_{i,j,k,l}$	flexibility matrix
G	dimensionless material parameter
G_f	lubricant modulus
$gbest$	Global best
h_0	minimum film thickness in rolling direction
H_c	Central film thickness
$H_{const.}$	Film thickness at axial constriction
k	thermal conductivity of fluid
$k_{a,b}$	thermal conductivity of bodies a and b
L	roller length
L_1, L_2	length of bodies 1 and 2
L_{rc}	dimensionless contact length ratio
L_{ro}	length of the rounded corner
n	slope in the lubricant shear-thinning zone
p	fluid pressure
p_0	maximum dry pressure
p'_0	maximum plain stress dry pressure

P', P''	mirrored pressures
P_{kl}	cell constant pressure
P_{Hertz}	Maximum Hertzian contact pressure
P_{spike}	Axial pressure spike
$pbest$	Personal best
R	equivalent roller radius
R_x	Equivalent radius in rolling direction
R_y, R_c	Crowning radius (in y direction)
R_r	Rounding radius
r_1, r_2	Random numbers
r_c	Dimensionless crowning radius
r_r	Dimensionless rounding radius
r_l	Dimensionless rounder corner length
S_0	dimensionless slope of viscosity-temperature relationship
S_l	dimensionless contact slenderness
T_{bulk}	bulk temperature
T_0	ambient temperature
$u_{a,b}$	velocities of surfaces a and b
u_e	rolling speed
U	dimensionless speed parameter
u_{ij}	deflection of a cell
v_i	Swarm velocity
$vgbest$	Virtual global best
w	total load
W	dimensionless load parameter
x_i	Swarm particle
y_d	distance from the roller end
x, y, z	local coordinate system
x_g, y_g, z_g	global coordinate system
$\overline{x}, \overline{y}, \overline{z}$	relative position

z_0	dimensionless viscosity-pressure index
α	pressure-viscosity coefficient
β	density-temperature coefficient
γ	viscosity-temperature coefficient
η	lubricant viscosity
$\eta_{0,1}$	shear-independent viscosity
Λ	limiting shear-pressure coefficient
ψ	Guilbault’s correction factor
ρ	density
ν	Poisson’s ratio
$\rho_{a,b}$	density of solids a and b
τ_L	limiting shear stress
λ	stress transition factor
τ_{max}	maximum shear stress
σ_{ij}	stress tensor
$\mathbf{\Phi}$	Lagrange shape function
ζ	spatial radius
ω	Inertia weight

INTRODUCTION

This document presents research works dedicated to elastohydrodynamic lubrication (EHL) taking place in non-conformal contacts. The study examines the influence of solid-fluid interactions appearing at the ends of finite line contacts on pressure, lubricant film thickness and temperature, and stress tridimensional distributions. As a concluding contribution, the developments exposed in the first parts of the thesis lead to a correction tool for optimal design of cylindrical rolling contact elements.

The scientific contributions resulting from this research are covered in three published (or submitted for publication) articles. These papers compose the chapters of the present document.

Background overview

Rolling contact elements, such as bearings and gears are widely used in industrial equipment to transfer force through contact surfaces in relative motion. The two most important problems associated with rolling contact elements are (*i*) undesired friction, which wastes a portion of the transmitted energy, and (*ii*) contact fatigue caused by repeated contact loads, which results in surface material losses producing gradual changes of the initial shapes, and ultimately leading to machine failures. The annual cost associated with friction energy and material losses is estimated at more than $100 billion in the United States alone (Mang et al., 2011).

Figures 0.1 and 0.2 illustrate the process of contact fatigue failure with some examples. Flaking failures of bearings occur when the surface of the raceway and the rolling element peels off due to excessive load, or improper mounting (Figure 0.1a). Figure 0.1b shows spalling failures, which occur when a tapered roller bearing experiences undue stress as a result of misalignment or heavy loading. Gears commonly fail due to pitting (surface damage caused by cyclic contact stress). Figure 0.2a presents initial pitting on a helical gear, where misalignment caused surface pits to form in over-stressed areas. Destructive pitting (Figure 0.2b) is the advanced stage of pit growth. Destructive pitting ultimately results in complete destruction of the tooth profiles, causing the operation to become extremely rough and noisy.


(a) (b)

Figure 0.1 (a) Flaking failure (Taken from Koyo catalogue),
(b) Spalling failure (Taken from TIMKEN catalogue)

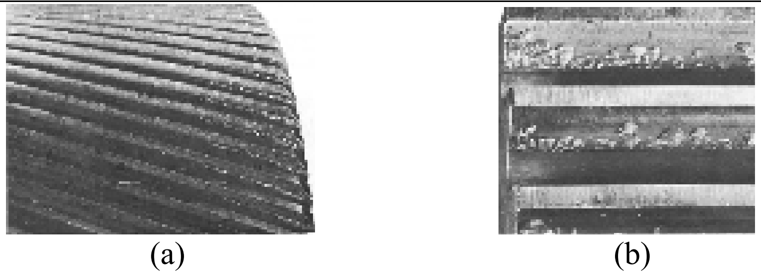
(a) (b)

Figure 0.2 (a) Initial pitting, (b) Destructive pitting
(Taken from Shipley, 1967)

Contact fatigue may originate from surface or subsurface regions. Under Hertzian conditions, the maximum shear stress appears at a short distance beneath the surface. Therefore, the material inner regions undergo fatigue crack initiation and propagation (Johnson, 1987). These cracks propagate toward the surface, leading to material separation. On the other hand, non-Hertzian contact conditions, resulting from free boundary nearness, asperity contacts, or surface sliding may bring the maximum stress values close to the surface, causing cracks to initiate in that region (Bold et al., 1992; Olver, 2005). However, under any conditions, the overall stress distribution controls the contact fatigue life (Littmann and Widner, 1965; Elsharkawy and Hamrock, 1991; Ioannides et al., 1999; Nelias et al., 1999; Dong et al., 2009).

Since they force the load to be distributed over a relatively small contact area, non-conforming contact conditions generate intense pressures. In rolling contact elements, contact pressures commonly reach up to 1.5 GPa. This pressure level corresponds to the weight of five male African elephants supported over a surface the size of the Canadian dime. With such high operating pressures, it is not surprising that contact surface deteriorations are common during the lifespan of these elements.

In many gears and roller bearings, contact happens along finite length lines. This type of contact presents stress concentration near the extremities (Figure 0.3a) drastically reducing the service life (Johnson, 1987). Usually, an axial crowning is provided (Figure 0.3b) to reduce edge-stress concentration, and more evenly distribute the load over the complete contact length. Moreover, an axial crowning allows the system to tolerate slight misalignments, and therefore function for longer periods of time (Hamrock and Anderson, 1983).

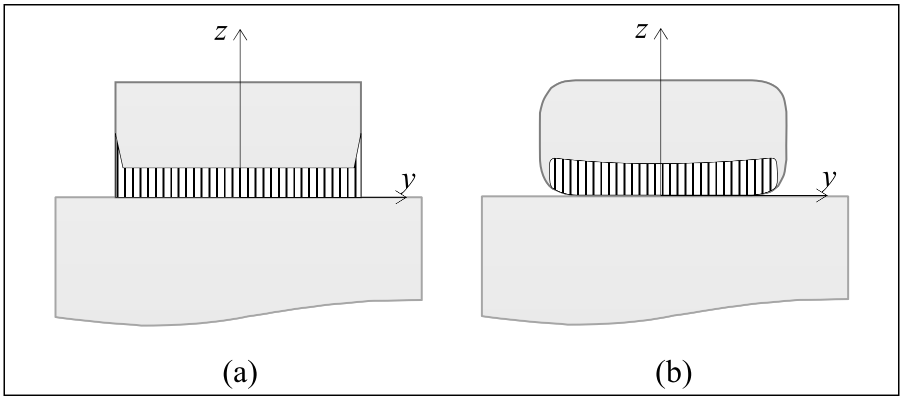

Figure 0.3 (a) Cylindrical roller, (b) Profiled roller

Rolling contact elements usually operate under lubricated conditions. Lubricants produce viscous oil films over contact areas which prevent metal-on-metal contact, and therefore, play an important role in controlling surface degradation (Figure 0.4). Elastic deformations of the contact interface caused by the extreme pressure generate an almost parallel gap for the fluid to pass through. This phenomenon is designated as elastohydrodynamic lubrication (EHL). This lubrication regime modifies the dry pressure distributions associated with elastostatic contact conditions. With pressure distributions of the order of GPa and film thickness in the micrometer range, it is easy to conceive that the lubricant properties may be affected from point to point over the contact area.

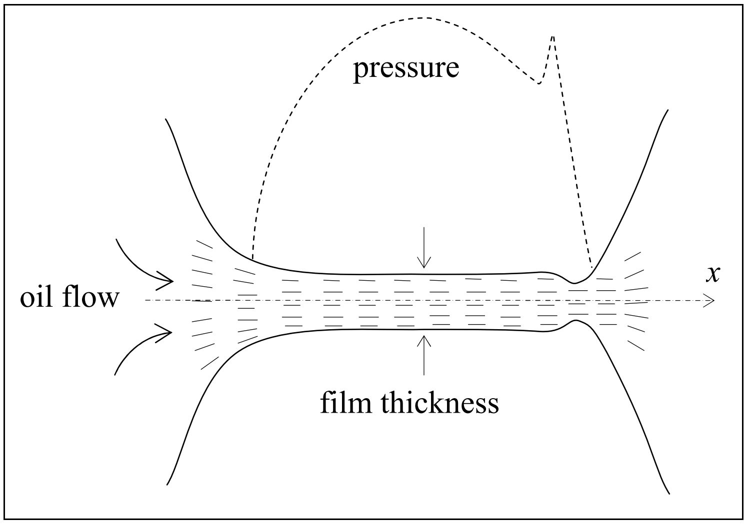

Figure 0.4 Elastohydrodynamic lubrication

Wymer and Cameron (1974) were pioneers in the experimental investigation of EHL of finite line contacts. They introduced optical interferograms of oil film shape for rollers with and without end profiling (Figure 0.5). Figure 0.5 illustrates different fluid film conditions existing over the roller contact area. These authors demonstrated that minimum film thickness tend to exist at roller ends, and in the case of straight rollers, film breakdowns are likely to occur at the edges.

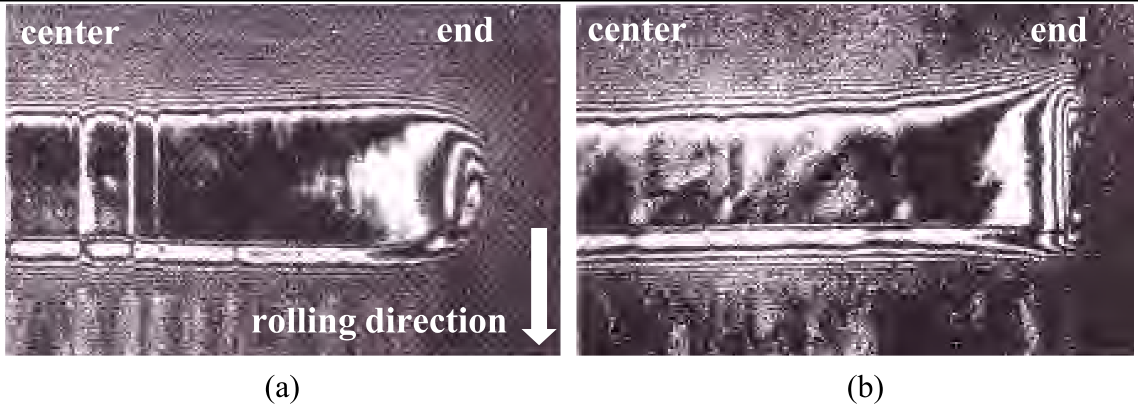

Figure 0.5 EHL footprints of finite line contacts, (a) Profiled end,
(b) Straight roller (Taken from Wymer and Cameron, 1974)

Over the past decades, many researchers worked on extensive mathematical modeling of the impact of edge contact on rolling contact elements (Lundberg and Palmgren, 1947, 1949, Nikpur and Gohar, 1975, Nayak and Johnson, 1979, Hartnett and Kannel, 1981, Reusner, 1987, Chen et al., 2001). Studies on this topic demonstrated that a logarithmic roller axial profile provides the best edge-stress reduction. However, all those profiling calculations were established based on elastic half-space theory, which does not take into consideration the influence of free boundaries.

Although during the past five decades many researchers addressed EHL problems associated with elliptical contacts and infinite line contacts (Figure 0.4 illustrates this condition), so far, only a few recent studies have investigated the EHL of finite line contacts (Chen et al., 2006, Lugt and Morales-Espejel, 2011, Zhu and Wang, 2011). Current EHL theory successfully predicts film thickness and pressure distributions in rolling direction (or flow direction in Figure 0.4) at the roller axial mid-position. However, the film thickness and pressure variations along the axial direction, particularly near the edges, cannot be accurately evaluated using the existing EHL analytical knowledge. Therefore, introducing corrective procedures to design axial profile of rolling contact elements, in such a way that lubricant behavior and free edge influence are taken into consideration remains indispensable.

At the present time, no analytical approach is able to satisfactorily produce optimum roller profiles under EHL conditions including free edge influence; the governing equations are highly nonlinear, and require numerical approaches, making the task difficult and often time consuming.

Research problem

Precise evaluation of oil film thickness and pressure distribution near the edge of a finite line contact under EHL regime is essential for accurate fatigue life estimation. Experimental work by Wymer and Cameron (1974) revealed a contrast in edge state between rollers with and without axial profiles. Chen et al. (1997) examined rollers with Lundberg profile under EHL conditions, and introduced the concept of optimum crowning. Mostofi and Gohar (1983) were the first to develop a numerical solution for the EHL of axially profiled rollers. Later, refinements of this approach appeared in Kuroda and Arai (1985), Xu et al. (1998), Park and Kim (1998), Kushwaha et al. (2002), Sun et al. (2004), Zhu et al. (2012). However, to the author's knowledge, none of these studies have successfully corrected the problem of edge-pressure overestimation inherent to the half-space formulation forming the basis of their models.

Actually, the elastic half-space approach effectively predicts contact stress and deformation distributions at a distance far away from the roller ends, where plain strain conditions apply. On the other hand, this approach remains unable to describe the situation near the roller ends. In reality, when the roller presents a sharp end, while the mating surface extends beyond it (Figure 0.3a), stress concentration occurs at the free boundary (Johnson, 1987). Conversely, the plane stress condition at the free edges of coincident-end rollers permits slight axial expansion and, consequently, reduces the edge pressure (Figure 0.6).

In order to tackle this problem and accurately simulate the free boundary influence, the first chapter of the thesis introduces an elastic quarter-space modeling strategy into the representation. Figure 0.7 shows a typical elastic quarter-space problem.

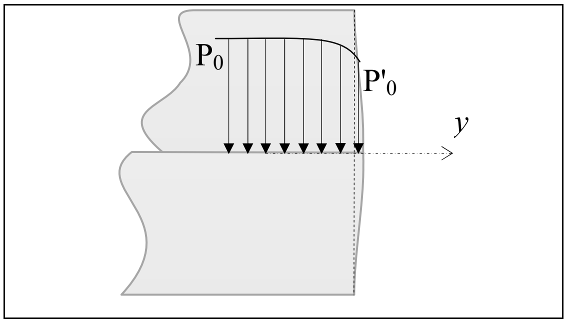

Figure 0.6 Rollers with coincident ends

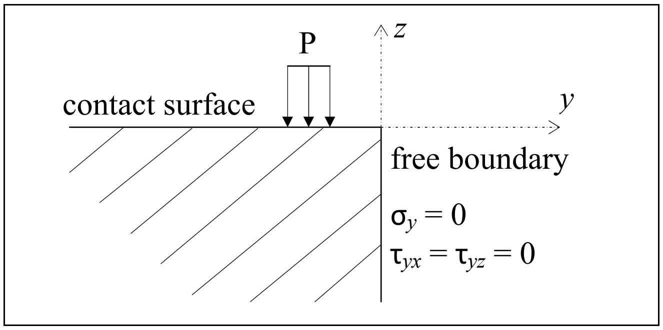

Figure 0.7 Elastic quarter-space problem

When the original Boussinesq force-displacement relationship (half-space formulation) is applied, it generates artificial shear and normal stress along traction-free boundaries. Hetenyi (1960, 1970) proposed a numerical correction method that implies an iterative mirrored load solution to release the model free-boundaries, and obtain accurate results. First, mirrored loads are introduced with respect to the *xz* plane to remove the artificial shear stress from the free boundary (Figure 0.8). At the same time, this operation results in a doubling of the artificial normal stress (σ_y). Hence, a second stage mirrored solution superimposes a $-\sigma_y$ distribution with respect to the *xy* plane, resulting in an additional σ_z distribution (Figure 0.9).

Thus, through a repetitive solution alternating between the horizontal and vertical planes, both artificial shear and normal stresses are finally eliminated.

More recently, based on the Hetenyi's approach, Guilbault (2011) introduced a simple corrective coefficient which accomplishes an equivalent free-boundary correction, but eliminates the iterative procedure; the coefficient multiplies the mirrored loads to simultaneously eliminate the artificial shear and normal stress influence on displacements, resulting therefore in significantly lower computational cost, while preserving the precision. The first stage of the present study analyses the response of the Guilbault's correction method when introduced in thermal EHL modeling of finite line contacts.

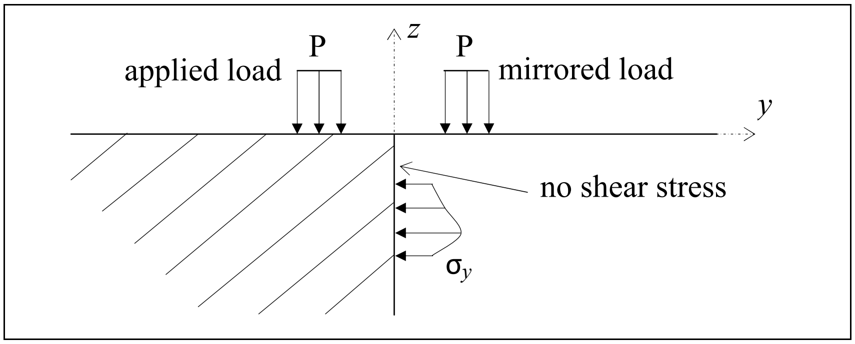

Figure 0.8 Mirrored solution with respect to *xz* plane

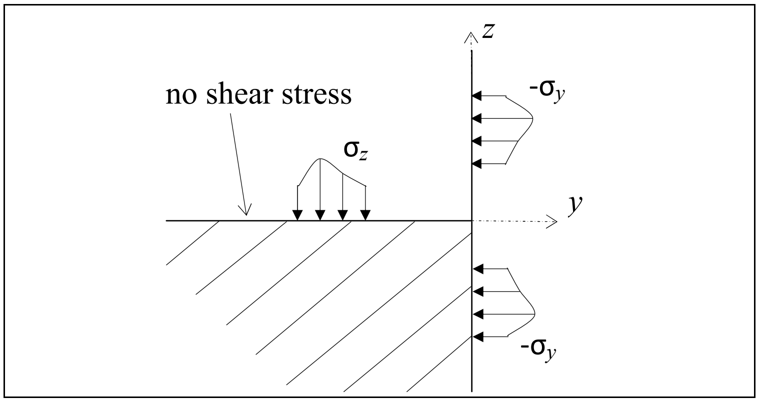

Figure 0.9 Mirrored solution with respect to *xy* plane

In addition to the lubricant film conditions, the contact pressure distribution determines the subsurface stress tridimensional field. While the finite element method (FEM) represents a common simulation approach to any stress evaluations, for contact problem, obtaining the necessary precision exploiting this option requires very fine meshes often leading to unreasonable calculation times. On the other hand, the half-space theory, which deals with contact pressure calculations, also offers closed-form expressions for stress calculations (de Mul et al., 1986; Johnson, 1987). In this case again, the original half-space stress expressions cannot account for the free boundaries of a finite line contact, and consequently leads to unrealistic stress values close to contact extremities. Hence, developing an efficient procedure for proper evaluation of the internal stress fields close to the body limits represents the second challenging aspect of the problem tackled in the present research.

Profile crowning aims to eliminate edge pressure and stress concentration. However, when the applied load exceeds the crowned profile design load, the edge effect reappears as a dominant problem, and the contact zone takes on a “dog bone” shape (similar to Figure 0.5b). Under EHL condition, an optimum geometry correction (maximizing the load carrying capacity) should yield longitudinally uniform film thickness and pressure distributions, and ensure that no edge stress increase develops over the load operating range. The last part of the study investigates this aspect of the line contact EHL problem, and focuses on the development of simple formulas for determining optimal crowning profiles. The realization of this portion of the research combines the numerical thermal EHL model developed in the thesis first parts with the particle swarm optimization (PSO) evolutionary algorithm.

Objectives

The main research objectives are:

i- To develop and validate a precise thermal 3D EHL model integrating the edge influence on pressure, lubricant film thickness and temperature, and stress distributions produced under finite line contact conditions.

ii- To investigate the behavior and consequences of profile modifications in non-conformal rolling element EHL, and identify optimal corrections.

These global objectives involve the following sub-objectives:

1. Develop a numerical thermal EHL model for point or line contacts integrating non-Newtonian lubricant physical behavior.

2. Integrate the free-boundary influence in the EHL model.

3. Develop a numerical model for determination of tridimensional contact stress fields.

4. Investigate edge contact impacts on surface and subsurface stress distributions under EHL conditions.

5. Investigate and establish the influence of different common roller profile corrections under EHL conditions on film shape, pressure, and temperature distributions.

6. Develop a design tool based on PSO for optimal profile correction of cylindrical rolling contacts.

Organization

The objectives outlined above are addressed in Chapters 1 to 3. Since this research thesis is arranged as a manuscript-based document, each of these chapters presents the analyses and developments already published in (or submitted as) a journal paper. The chapter presentation preserves the article structure, and only adapts the text form to guaranty the required document continuity.

Chapter 1 develops the thermal EHL model designed to simulate the edge effects in line contacts. To the author’s knowledge, this model is the first able to characterize the free-edge influence on EHL film. In addition to its accuracy, the developed model offers rapid solution for EHL problems involving low-to-extreme pressures. The chapter also includes a detailed numerical investigation of the potential influence of solid-fluid interactions on pressure, film thickness, and temperature near the contact zone extremities of finite line contact. This part of the investigation examines and compares the response of crowned roller with rounded corners to the well-known logarithmic modification. This work has been published in *Tribology International* journal (Najjari and Guilbault, 2014, “*Edge contact effect on thermal elastohydrodynamic lubrication of finite contact lines*”).

Chapter 2 presents the preparation of a semi-analytical model developed to characterize contact stress fields affected by discontinuities inherent to finite line contact problems. The analysis examines the relation existing between contact half-width and transition of the axial stress from a plane strain condition in the inner body region towards a plane stress state at a free boundary. The chapter includes a detailed validation of the model based on a two-level factorial comparison contrasting the model stress prediction with results obtained from FEM analyses. The validation considers three dimensionless factors: the contact slenderness, the contact length ratio, and the load. This part of the study has been published in *Tribology International* journal (Najjari and Guilbault, 2014, “*Modeling the edge contact effect of finite contact lines on subsurface stresses*”).

Chapter 3 discusses the preparation of the design tool for optimal roller profile corrections. The research works presented in Chapter 3 combine the 3D thermal EHL model constructed in the previous chapters to a modified version of the particle swarm optimization (PSO) algorithm to develop formulas for rapid design of optimal roller profiles. Based on Chapter 1 conclusions demonstrating that a crowned roller with rounded corners can generate uniform film thickness and pressure distributions equivalent to that produced by a logarithmic profile, Chapter 3 focuses on the crowned roller form, and develops formulas offering instant evaluations of the shape definition parameters. In order to generalize the application range of the formulas, a dimensional analysis reduces the basic dimensions to dimensionless parameters (slenderness and load). The analysis also integrates the lubricant viscosity contributions. The final outcome is a rapid design-tool defining corrections that maximize EHL load-carrying capacity. This part of the thesis has been submitted to the journal of *Mechanism and machine theory* (Najjari and Guilbault, 2014, "*Formula derived from particle swarm optimizations (PSO) for optimum design of cylindrical roller profile under EHL regime*").

Finally, the two last sections conclude the document, summarize the important scientific contributions of the thesis and formulate some recommendations for future developments in the domain.

CHAPITRE 1

ARTICLE 1: EDGE CONTACT EFFECT ON THERMAL ELASTOHYDRODYNAMIC LUBRICATION OF FINITE CONTACT LINES

Morteza Najjari and Raynald Guilbault

Department of Mechanical Engineering, École de technologie supérieure,
1100 Notre-Dame Street West, Montréal, Québec, Canada H3C 1K3

This Article was published in Tribology International Journal in March, 2014

1.1 Abstract

Minimum lubricant film thickness and maximum pressure every so often appear close to roller ends. This study combines the Boussinesq-Cerruti half-space equations with a free boundary correction procedure for precise modeling of edge contact conditions. The thermal EHL model developed associates this representation to a standard finite difference of the energy equation, and to a modified finite difference expansion of the Couette term of the Reynolds equation. To complete the model, the Carreau expression describes the shear-thinning response of the lubricant. The investigation includes different roller profile corrections. The results show that a large radius crowning modification combined with a rounding of the corners constitutes the most effective profile adjustment.

Keywords: Thermal EHL, non-Newtonian lubrication, finite line contact, edge contact.

1.2 Introduction

An elastohydrodynamic lubrication regime (EHL) develops when high pressures (compared to Young modulus of the bodies) generate significant surface deformations, impacting the lubricant film shape. Usually, in real applications such as gears, cams and roller bearings, contact lines are of a finite length, a condition which leads to the edge contact problem, with the most severe case arising between contacting surfaces of different lengths. To reduce the damaging effect of finite contact lines, mechanical designers commonly round off or axially profile the surfaces close to the body ends. The well-known studies published by Gohar and Cameron (1963, 1967), Wymer and Cameron (1974) and Bahadoran and Gohar (1974) are among the very few to have investigated the finite line contact problem. Their experimental investigations analyzed the effects of roller geometry on EHL lubricant film shape and thickness. For instance, the optical fringe obtained by Wymer and Cameron (1974) demonstrated that the film thickness thins down near the roller ends. Even though recent reviews (Chen et al., 2006; Lugt and Morales-Espejel, 2011; Zhu and Wang, 2011) show that analyses of infinite line contact and point contact problems have been well developed over the past decades, the early finite line contact numerical simulations (Mostofi and Gohar, 1983; Kuroda and Arai, 1985; Xu et al., 1998; Park and Kim, 1998) were limited to light or moderate loads. More recent publications have examined the influence of assembly precision and surface modifications. For example, Kushwaha et al. (2002) investigated the influence of alignment on the film shape between rollers and raceways; Chen et al. (2001) studied the effect of crowning and logarithmic roller end profiles, and Liu and Yang (2002), and Sun and Chen (2004) analyzed the thermal EHL of finite line contact under heavy loads with the multigrid approach developed by Lubrecht (1987). Recently, Zhu et al. (2012) presented a mixed EHL investigation including realistic geometries and surface roughness effects on finite line contact modeling. Xue et al. (2012) carried out experimental EHL studies of finite rollers with logarithmic end profiles under heavy loads, and found that the film at the roller ends may be thinner than the outlet film at the mid-length position.

While increasing the treatment sophistication of the Reynolds equation, the advent of the multigrid approach facilitated numerical investigations of high pressure EHL problems, and consequently, the description of the lubricant behavior in finite line contact conditions. However, in addition to the oil flow perturbations accounted for in the Reynolds equation, the free surfaces at the ends of a contact line also strongly affect the deformation of the loaded surfaces. Nevertheless, to the author’s knowledge, the potential localized solid-fluid interactions have never been thoroughly described.

Under dry contact conditions, the free boundaries have a significant influence on the contact stresses and deformation (Johnson, 1987). For example, the finite length roller-half space contact condition is well known to generate high stress concentration at the roller limits. Conversely, the plane stress condition at the free boundaries of coincident end rollers permits small axial expansions, and consequently, local contact pressure reductions, which may be approximated by Eq. (1.1) (Johnson, 1987).

General contact solutions are often based on the classical elastic half-space theory (Boussinesq-Cerruti), which establishes the relation between the surface tractions and displacements. However, because of the underlying half-space assumption, when employed without any correction, the relation produces incorrect pressure increases near free edges. Over four decades ago, Hetényi (1960, 1970) proposed a correction process involving a shear stress elimination from mirrored pressure distributions, in combination with an iterative treatment for normal stress correction. Recently, Guilbault (2011) introduced a correction factor (Eq. 1.2) which multiplies the mirrored pressures to simultaneously correct the shear and normal stress influence on displacements, thereby guaranteeing significantly lower calculation times as compared to a complete Hetényi process.

$$p_0' \approx (1-\nu^2)\,p_0 \tag{1.1}$$

$$\psi = 1.29 - \frac{1}{1-\nu}\left(0.08 - 0.5\nu\right) \tag{1.2}$$

This paper presents a detailed numerical investigation of the potential influence of solid-fluid interactions on the pressure, film thickness and temperature distributions at the ends of finite contact lines. The study develops a model combining accuracy and high solution speed for low- to extreme-pressure EHL problems. In this model, the general non-Hertzian contact solution presented by Hartnett (1980) to calculate surface deformations and pressure distributions is completed with the Hetényi shear stress elimination process and the Guilbault correction factor for the relief of the normal stress effect on the free boundaries. While a standard finite difference formulation ensures an energy equation solution, a simple algorithm based on a modified forward finite difference iterative method, presented by Cioc (2004), resolves the Reynolds equation for the thermal EHL part of the global solution. The section following the model preparation compares the numerical results to experimental measurements published by Wymer and Cameron (1974). In the third section, the free boundary correction contribution is analyzed in two steps: first using only the mirrored pressures for shear correction, and thereafter integrating Guilbault correction factor for a complete correction. The last section investigates the influence of common roller profile axial modifications.

1.3 Model preparation and governing equations

1.3.1 Contact problem

The general dry contact problem resolution procedure is well described and validated by Guilbault (2011). The EHL model developed in the present paper uses the same algorithm: the solution domain is divided into constant pressure cells, and the flexibility matrix written for the resulting mesh. The pressure cells are mirrored with respect to the free boundaries, and their influence is integrated into the flexibility matrix to eliminate the free boundary artificial shear stress. To remove the remaining normal stress influence, each mirror cell contribution is multiplied by Guilbault’s factor prior to its integration into the flexibility matrix. This last operation completely releases the boundaries.

1.3.2 Thermal EHL problem

Assuming that the lubricant flow is parallel to the x-axis and that the roller length coincides with the y-axis (see Figure 1.1), and considering the following hypotheses, the Reynolds equation is given by Eq. (1.3).

- The film thickness and fluid density are time-independent
- The surface speed in the y direction is negligible

$$\frac{\partial}{\partial x}\left(\frac{\rho h^3}{\eta}\frac{\partial p}{\partial x}\right)+\frac{\partial}{\partial y}\left(\frac{\rho h^3}{\eta}\frac{\partial p}{\partial y}\right)=12u_e\frac{\partial(\rho h)}{\partial x} \tag{1.3}$$

where u_e is the entraining speed (x-axis), and the pressure boundary conditions are: pressure equal to zero at the body limits as well as at positions far before the inlet and after the outlet ($p = 0$ at $y = \pm L/2$, x_{min} and x_{end}) and pressure gradient equal to zero after the outlet $p = \partial p/\partial x = 0$ at x_{end}.

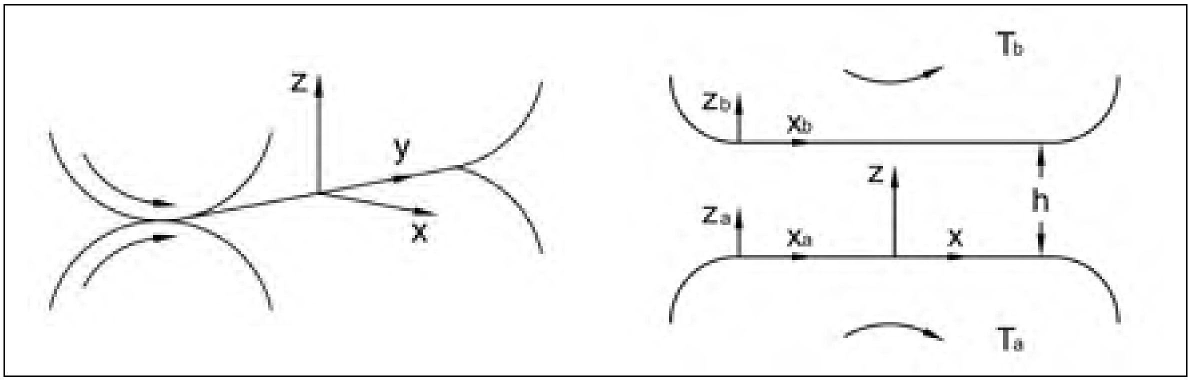

Figure 1.1 Coordinate system

1.3.3 Lubricant modeling

1.3.3.1 Viscosity-pressure-temperature relationship

The shear-independent viscosity is often expressed by one of the following two variants of the Roelands equation (Eqs. 1.4a and 1.4b). Eq. (1.4b) is however considered more accurate, but nevertheless, Sadeghi and Sui (1990), Lee and Hsu (1993) and Hsu and Lee (1994) employed Eq. (1.4a). For the model validation, section 1.4.2 repeats the tests published by Sadeghi and Sui (1990), Lee and Hsu (1993), Hsu and Lee (1994), Guilbault (2013) and compares the temperatures and friction coefficients obtained with published values. Therefore, for consistency, during this comparison, the present model also uses Eq. (1.4a). For all other calculations of this study, Eq. (1.4b) is preferred.

$$\eta_1(p,T) = \eta_0 \exp\left\{\left(\ln(\eta_0)+9.67\right)\left(-1+\left(1+5.1\times10^{-9}p\right)^{z_0}\right)+\gamma(T_0-T)\right\} \tag{1.4a}$$

$$\eta_1(p,T) = \eta_0 \exp\left\{\left(\ln(\eta_0)+9.67\right)\left(\left(\frac{T-138}{T_0-138}\right)^{-S_0}\left(1+5.097\times10^{-9}p\right)^{z_0}-1\right)\right\} \tag{1.4b}$$

where z_0 is related to α as follows:

$$z_0 = \frac{\alpha}{5.1\times10^{-9}\left(\ln(\eta_0)+9.67\right)} \tag{1.5}$$

1.3.3.2 Rheological model

The influence of severe shear conditions leading to a shear-thinning response of the lubricant is also well-established (Guilbault, 2013), and is often described by the Carreau expression. On the other hand, the limiting shear stress is nearly proportional to the pressure, and influenced by the temperature. Equation 1.6 establishes the limiting shear stress. The value of Λ oscillates around 0.04 - 0.08. Incorporating Eq. 1.6 into the Carreau relation leads to a simple and accurate rheological model (Guilbault, 2013).

$$\tau_L = \Lambda p \tag{1.6}$$

$$\eta = \min\left[\eta_1\left[1+\left(\frac{\eta_1}{G_f}\dot{\chi}\right)^2\right]^{\frac{(n-1)}{2}}, \frac{\tau_L}{\dot{\chi}}\right] \tag{1.7}$$

1.3.3.3 Density-pressure-temperature relationship

The equation proposed by Dowson and Higginson (1959) for a compressible fluid formulates the density-pressure-temperature relationship:

$$\rho(p,T) = \rho_0\left[1+\frac{0.6\times10^{-9}p}{1+1.7\times10^{-9}p}\right]\left(1-\beta(T-T_0)\right) \tag{1.8}$$

1.3.4 Energy equation

Neglecting the heat conduction along *x* and *y* directions, the energy equation within the lubricant film is written as:

$$k\frac{\partial^2 T}{\partial z^2} = \rho c_p u\frac{\partial T}{\partial x} - \beta T u\frac{\partial p}{\partial x} - \eta\left(\frac{\partial u}{\partial z}\right)^2 \tag{1.9}$$

Where

$$u=-\frac{1}{2\eta}\frac{\partial p}{\partial x}z(h-z)+u_a\left(\frac{h-z}{h}\right)+u_b\frac{z}{h} \tag{1.10}$$

The heat repartition between the loaded solids is calculated during the solution of the energy equation, which is written for solid bodies as follows (Eq. 1.11):

$$k\frac{\partial^2 T}{\partial z^2}=\rho c_p u\frac{\partial T}{\partial x} \tag{1.11}$$

The solution process ensures that the temperature inside the solids at a depth greater than $3C$ is equal to the bulk temperature (T_{bulk}). Moreover, if the bulk temperatures of bodies a and b are assumed to be equal to the ambient temperature (T_0), the boundary conditions are:

$$T_a\big|_{z_a=-3C}=T_0\ ,\ T_b\big|_{z_b=3C}=T_0 \tag{1.11a}$$

$$k_a\frac{\partial T}{\partial z_a}\bigg|_{z_a=0}=k\frac{\partial T}{\partial z}\bigg|_{z=0}\ ,\ k_b\frac{\partial T}{\partial z_b}\bigg|_{z_b=0}=k\frac{\partial T}{\partial z}\bigg|_{z=h} \tag{1.11b}$$

1.3.5 Film thickness

The EHL film thickness is classically formulated as given by Eq. 1.12 a.

$$h(x,y)=h_0+g(x,y)+\frac{2}{\pi E'}\iint_{\Omega}\frac{p(x',y')dx'dy'}{\sqrt{(x-x')^2+(y-y')^2}} \tag{1.12a}$$

where h_0 corresponds to the initial body separation, $g(x,y)$ represents the axial profile of the roller, and finally, the integral term is the elastic deformation of the contact surfaces, established here with the model of Guilbault (2011). Therefore, when adopting the discretization process of the contact model (Guilbault, 2011), the solution domain is discretized into constant pressure rectangular cells. The film shape expression then becomes:

$$h_{i,j} = h_0 + g_{i,j} + \frac{2}{\pi E'} \sum_{k=1}^{n_x} \sum_{l=1}^{n_y} f_{i,j,k,l} p_{k,l} \tag{1.12b}$$

where $f_{i,j,k,l}$ is known as the deformation matrix (Hartnett, 1980).

1.3.6 Load

The load balance equation (Eq. 1.13) ensures the load equilibrium over the solution domain. This equation is expressed as:

$$\iint_{\Omega} p(x,y)dxdy = w \tag{1.13}$$

1.3.7 Numerical thermal EHL Model

1.3.7.1 Modified forward iterative method

To determine the pressure distribution within the lubricant film, the Reynolds equation (Eq. 1.3) must simultaneously be solved with the equations for film thickness (Eq. 1.12 b), lubricant properties (Eqs. 1.7 and 1.8) and load balance (Eq. 1.13). The solution of the energy equation (Eqs. 1.9 and 1.11) gives the temperature within the fluid and the solid bodies. Therefore, since the viscosity, the density, the pressure and the temperature are nonlinearly interconnected elements, the solution of the equation system is extremely sensitive, and may rapidly become unstable when submitted to high loads. Consequently, special approaches, such as the combination of the line relaxation scheme and the multigrid method, are required to overcome instability problems. The forward iterative method is probably the simplest approach used in the past to solve this nonlinear problem. Unfortunately, in presence of heavy loads resulting in pressures greater than 1 GPa, the method was rapidly proven to be unstable. However, recently Cioc (2004) observed that the instability was related to the Couette term finite difference formulation, and thus suggested a modified approach capable of overcoming the solution instability for pressures higher than 1 GPa; the modified method separates the pressures of finite difference mesh points *i*, *i-1* and *i+1* between the two consecutive iterations *k-1* and *k*. The Couette term is thus written as in Eq. 1.14:

$$\left.\frac{\partial(\rho h)}{\partial x}\right|_{i,j}^{k}=\frac{(\rho h)_{i,j}^{k}-(\rho h)_{i-1,j}^{k}}{\Delta x}$$
$$=\frac{1}{\Delta x}\left[\begin{array}{c}\rho_i\left(f_{i,j,i-1,j}p_{i-1,j}^{k}+f_{i,j,i,j}p_{i,j}^{k}+f_{i,j,i+1,j}p_{i+1,j}^{k}\right)-\\ \rho_{i-1}\left(f_{i-1,j,i-1,j}p_{i-1,j}^{k}+f_{i-1,j,i,j}p_{i,j}^{k}+f_{i-1,j,i+1,j}p_{i+1,j}^{k}\right)+\\ \rho_i\left(h_{i,j}^{k-1}-f_{i,j,i-1,j}p_{i-1,j}^{k-1}-f_{i,j,i,j}p_{i,j}^{k-1}-f_{i,j,i+1,j}p_{i+1,j}^{k-1}\right)-\\ \rho_{i-1}\left(h_{i-1,j}^{k-1}-f_{i-1,j,i-1,j}p_{i-1,j}^{k-1}-f_{i-1,j,i,j}p_{i,j}^{k-1}-f_{i-1,j,i+1,j}p_{i+1,j}^{k-1}\right)\end{array}\right] \tag{1.14}$$

Figure 1.2 presents the flowchart of the modified iterative method developed by Cioc (2004).

1.4 Model validation

The model validation involves a comparison along the two axes: the film thicknesses in the rolling direction (*x*-axis), at the mid-length section ($y = 0$), and along the initial contact line (*y*-axis) are compared to those published by Wymer and Cameron (1974). The geometry of the roller and the lubricant properties corresponding to the experiments of Wymer and Cameron (1974) are given in Table 1.1.

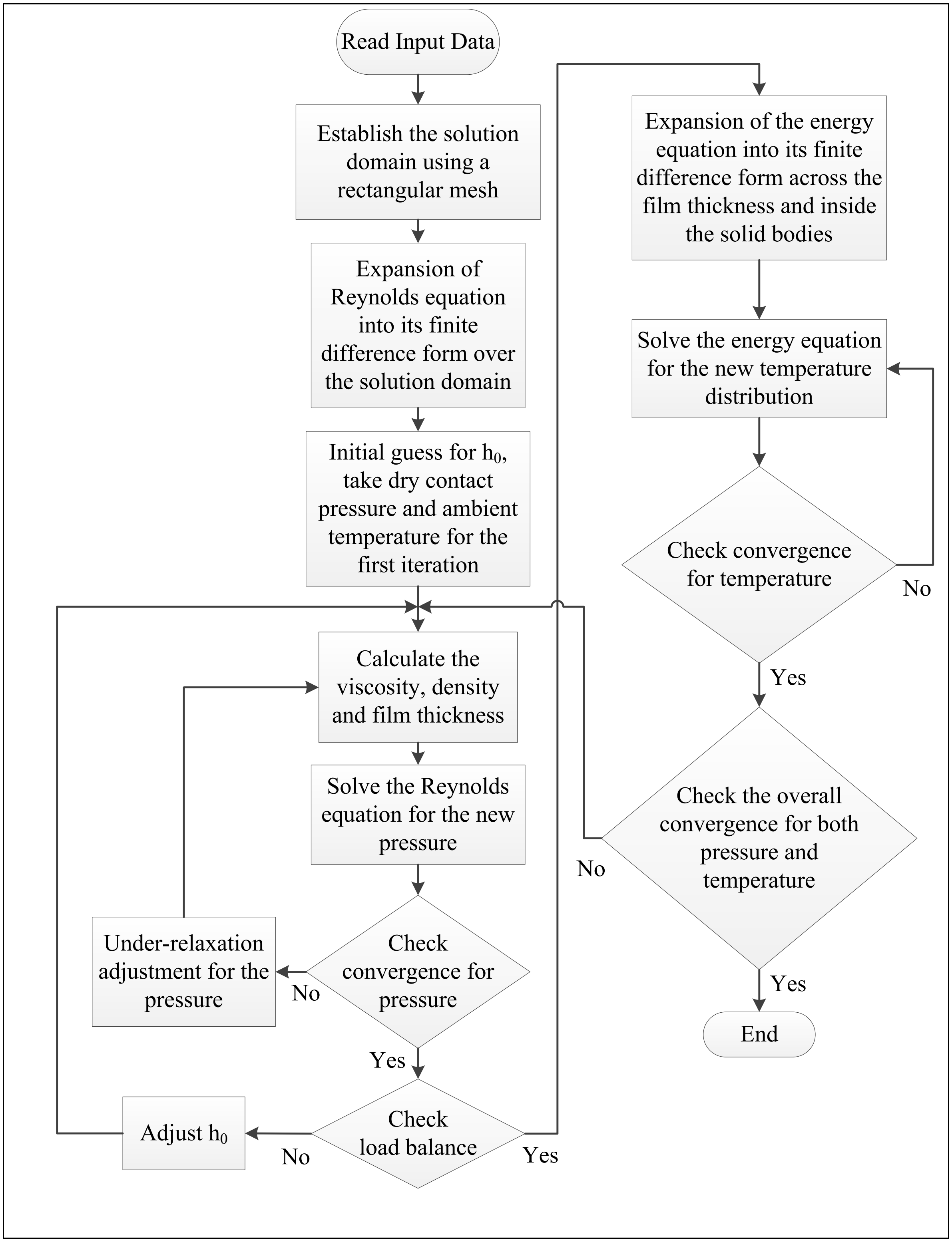

Figure 1.2 Flowchart for model solution

The roller profile approximation is identical to that of Sun and Chen (2006). Since the precise information was not available in the study, Sun and Chen assumed that the location of the first measured point in the Wymer and Cameron's experiments was located at $y_d = 0.2$mm. However, the lateral film constriction they calculated did not precisely coincide with the experimental results. Their assumption is therefore adjusted in this study to $y_d = 0.1$mm. Figure 1.3 draws the resulting axial modification of the roller profile. As mentioned by Wymer and Cameron (1974), Shell HVI 650 mineral oil was used during the experiments. The lubricant properties are obtained from Evans and Johnson (1986).

After validation with experimental measurements, the temperature distributions and friction coefficients obtained from the model were compared to numerical values published by Sadeghi and Sui (1990), Hsu and Lee (1993, 1994) and Guilbault (2013). The roller and the lubricant properties definition of Sadeghi and Sui (1990) are given in Table 1.2.

For the following results, the label "No-Correction" refers to calculations made without accounting for the mirrored pressure or Guilbault's correction factor. The designation "Mirror Correction" refers to results obtained after the integration of the mirrored pressure cell contribution into the flexibility matrix. Finally, the label "Complete Correction" identifies the values established from calculations incorporating both the mirrored pressure cell contribution and Guilbault's factor into the flexibility matrix.

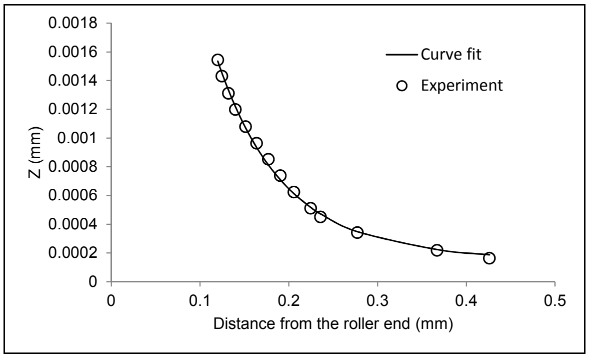

Figure 1.3 Roller profiling

Table 1.1 Roller and lubricant properties (Wymer and Cameron, 1974; Evans and Johnson, 1986)

Roller		**Lubricant**	
Radius *R*	4.1 mm	Ambient temperature T_0	313 K
Length *L*	13.7 mm	Viscosity at 303 K	0.900 Pa.s
Total cone angle	7.9°	Viscosity at 393 K	0.015 Pa.s
Young modulus *E*	206 GPa	Visc.-Press. coef. α at 303 K	30.2 GPa^{-1}
Poisson ratio ν	0.3	Visc.-Press. coef. α at 393 K	16.4 GPa^{-1}
Density ρ	7850 kg/m^3	Density ρ at 313 K	888 kg/m^3
Thermal conduct. *k*	46 W/(m.K)	Density ρ at 373 K	853 kg/m^3
Specific heat *c*	470 J/(kg.K)	Thermal conduct. *k*	0.125 W/(m.K)
Glass		Specific heat *c*	2000 J/(kg.K)
Young modulus *E*	75 GPa	Modulus *G* at 303 K	$0.1 + 3.0\times P$ GPa
Poisson ratio ν	0.22	Slope factor* *n* at 313 K	0.570
Density ρ	2500 kg/m^3	Slope factor *n* at 373 K	0.993
Thermal conduct. *k*	0.78 W/(m.K)		
Specific heat *c*	840 J/(kg.K)	* The values were taken from Guilbault (2013)	

Table 1.2 Roller and lubricant properties, from Sadeghi and Sui (1990)

Roller		**Lubricant**	
Equivalent radius *R*	20 mm	Ambient temperature T_0	313 K
Young modulus *E*	200 GPa	Viscosity at T_0	0.04 Pa.s
Poisson ratio ν	0.3	Visc.-Press. coef. α	15.9 GPa^{-1}
Density ρ	7850 kg/m^3	Visc.-Temp. coef. γ	0.042 K^{-1}
Thermal conduct. *k*	47 W/(m.K)	Density ρ	846 kg/m^3
Specific heat *c*	460 J/(kg.K)	Density-Temp. coef. β	6.4×10^{-4} K^{-1}
		Thermal conduct. *k*	0.14 W/(m.K)
		Specific heat *c*	2000 J/(kg.K)

1.4.1 Film thickness comparison

The central film thickness in the rolling direction is presented in Figure 1.4. The graph in Figure 1.4 includes three dimensionless speeds. The results were established with a complete relief of the free boundaries at the ends of the roller (Hetényi and Guilbault corrections). The calculated results show high correspondence with the experiments. Figure 1.5 shows the film thickness in the axial direction. The calculations again include three dimensionless speeds. The graph also compares the results obtained with a complete relief of the free boundaries to the no-correction conditions. The film thickness distributions are in close agreement; the constriction location is well predicted by the model regardless of the condition of the boundaries at the ends of the roller. In fact, because of the precision of the experimental measurements, and the axial profile modification of the roller, which reduces the end influence, it is difficult to describe the contribution of the free boundaries to the simulation results with a high level of certainty. Nevertheless, the curves indicate that because of the rigidity reduction associated with the complete correction, the axial constriction shape and position are affected by the free boundary representation. Therefore, since the film thickness is significantly lower at the roller ends than at the central outlet position, an accurate depiction of the boundary behavior is very important.

1.4.2 Temperature and coefficient of friction comparison

The simulations integrate one dimensionless load W ($=1.3\times10^{-4}$) and four dimensionless speeds U (1.8×10^{-11}, 3.6×10^{-11}, 5.5×10^{-11} and 7.3×10^{-11}). The material parameter is $G = 3500$. Table 1.3 compares the maximum mid-film and average temperature rise, and the dimensionless minimum film thickness evaluated at the central position of the roller ($y = 0$) to the reference values. Table 1.3 indicates that compared to the result of Sadeghi and Sui (1990), the maximum difference for the maximum mid-film temperature increase is 4°C (within 8% margin of error). On the other hand, considering the maximum average temperature rise, compared to Lee and Hsu (1993) the difference is less than 2°C. Finally, the

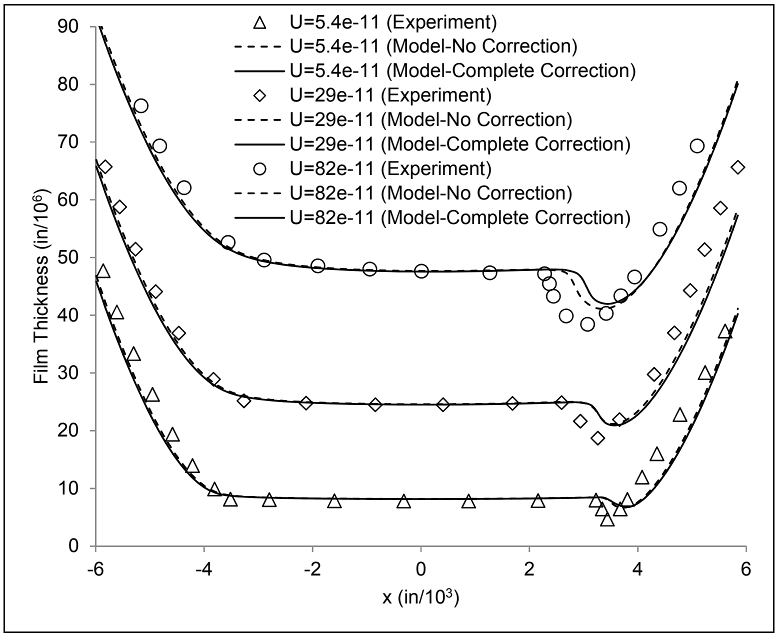

Figure 1.4 Central film thickness in rolling direction

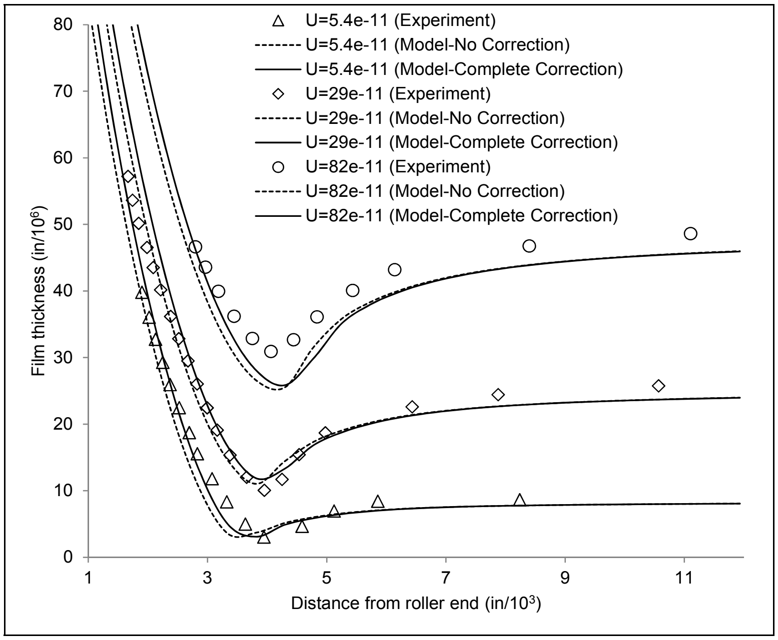

Figure 1.5 Film thickness in the axial direction

maximum deviation of the minimum film thickness is 8.3% (case of U=1.8×10^{-11} and 30% slip). All simulations integrated a complete relief of the free boundaries.

Table 1.3 Temperature comparison for W=1.3×10^{-4}

U	Slip (%)	Maximum mid-film temperature increase (°C)				Maximum average temperature increase (°C)			Dimensionless minimum film thickness		
		Sadeghi (1990)	Hsu-Lee (1994)	Guilbault (2013)	Model	Lee-Hsu (1993)	Guilbault (2013)	Model	Sadeghi (1990)	Hsu-Lee (1994)	Model
1.8 ×10^{-11}	0	0.91	-	0.43	0.53	-	0.43	0.49	0.0555	-	0.0600
	10	10.64	-	14.66	14.71	-	12.64	12.52	0.0551	-	0.0585
	20	31.61	-	31.55	32.54	-	27.17	27.8	0.0526	-	0.0564
	30	46.57	-	44.55	46.09	-	38.35	39.47	0.0502	-	0.0544
3.6 ×10^{-11}	0	2.76	-	1.59	3.28	-	1.59	2.63	0.0891	-	0.0924
	10	26.64	27.28	28.16	28.42	21.31	22.94	22.51	0.0867	0.0871	0.0893
	20	53.46	51.17	51.02	52.48	40.00	41.38	41.61	0.0831	0.0834	0.0860
	30	71.12	67.19	66.90	69.03	53.09	54.27	54.83	0.0803	0.0808	0.0832
5.5 ×10^{-11}	0	6.15	-	3.34	7.00	-	3.34	5.34	0.1145	-	0.1155
	10	40.37	39.54	40.43	40.30	29.76	32.15	30.89	0.1118	0.1078	0.1113
	20	69.95	67.50	66.66	67.83	50.09	52.67	52.01	0.1077	0.1035	0.1073
	30	89.10	85.50	84.11	86.09	64.46	66.45	66.08	0.1037	0.1001	0.1039
7.3 ×10^{-11}	0	9.97	-	5.27	10.43	-	5.27	7.83	0.1351	-	0.1358
	10	51.33	51.18	50.26	50.46	38.77	39.59	37.77	0.1305	0.1201	0.1304
	20	82.95	79.70	78.45	80.42	59.76	61.29	60.16	0.126	0.1156	0.1260
	30	102.67	99.18	96.78	99.73	73.28	75.58	74.67	0.1226	0.1119	0.1226

Figures 1.6 and 1.7 compare the coefficients of friction (load W=1.3×10^{-4} and material parameter G=3500) at different rolling speeds to those published in Sadeghi and Sui (1990) and Lee and Hsu (1993). The curves demonstrate a very good agreement.

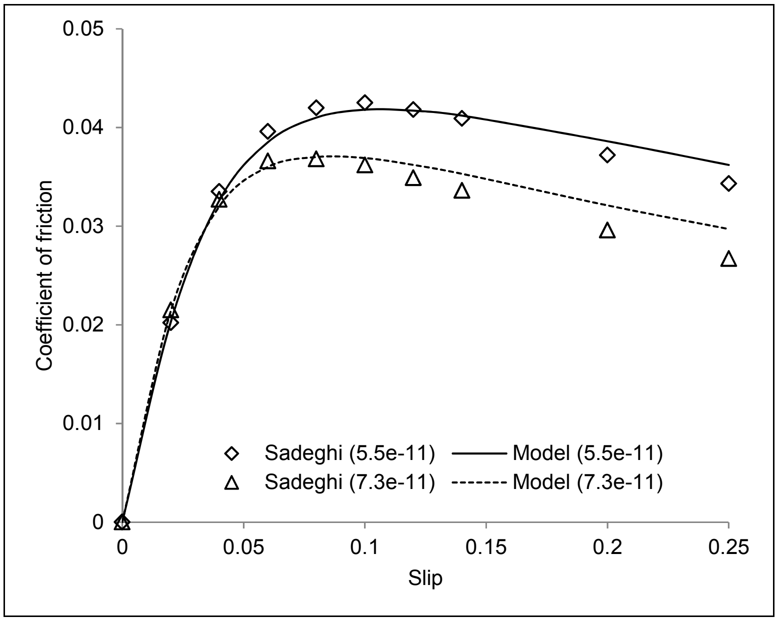

Figure 1.6 Friction coefficient for W=1.3×10^{-4}, G=3500

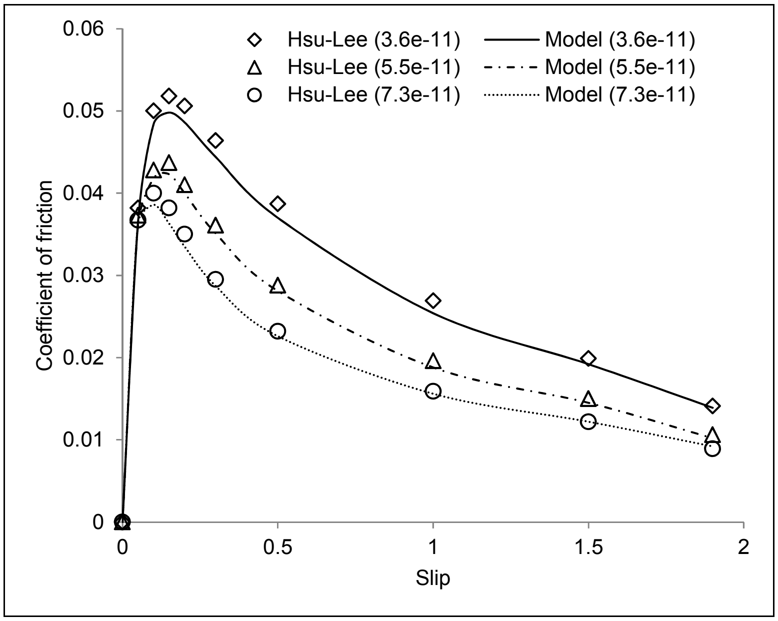

Figure 1.7 Friction coefficient for W=1.3×10^{-4}, G=3500

1.5 Profiled roller

Cylindrical bodies are often designed with axial crown profiles in order to compensate for misalignment errors. The ends are also often rounded or chamfered to eliminate stress concentrations resulting from edge contact. Logarithmic profiles represent another alternative to smooth contact pressure distributions. In this section, five roller profile sample cases are examined and compared to unprofiled roller responses (crowned, rounded corners, crowned with rounded corners, chamfered corners and logarithmic profile). The general properties of the roller and lubricant are as shown in Table 4. For all simulations, the load and speed are 8000 N (corresponding to a maximum Hertz pressure of 1.25 GPa) and 7.5 m/s, with the slip ratio equal to 20%. The computational domain stretches from $x_{min} = -3C$ to $x_{end} = 1.5C$ in the x direction, while half of the roller length is considered in the y direction. Along the z-axis, the solution domain includes the film thickness and extends to a depth of $3C$ into both solids.

The model convergence is illustrated in Table 1.5 for the coincident end straight roller case. N_x and N_y correspond to the number of divisions along the x- and y-axes, respectively. The left column of the table illustrates the influence of N_x, and the right column shows the influence of N_y. Although the pressure variation is less than 0.3% for the different mesh sizes, the central film thickness convergence trend demonstrates the more significant influence of the mesh size. The value variations indicate that the solution stabilizes between the 120×80 and 120×100 meshes. Therefore, comparing all film thicknesses to the 120×100 solution leads to the precision levels shown in the table. Table 1.5 also includes the calculation times. Thus, when accounting for the time aspect, the 120×80 mesh assuring a precision of 99.8% appears to be the optimal option, while the 100×40 mesh with a precision higher than 88% represents an efficient trade-off. All of the results presented in this section were obtained with the mesh size 120×80. Along the z-axis, the film thickness and solid bodies were described by 30 and 20 nodes, respectively.

Table 1.4 Roller and lubricant properties, from Guilbault (2013)

Roller		**Lubricant**	
Radius R	17.5 mm	Ambient temperature T_0	313 K
Length L	10.0 mm	Viscosity at 313 K	0.19580 Pa.s
Young modulus E	200 GPa	Viscosity at 373 K	0.01664 Pa.s
Poisson ratio ν	0.3	Visc.-Press. coef. α at 313 K	20.2031 GPa^{-1}
Density ρ	7850 $\mathrm{kg/m}^3$	Visc.-Press. coef. α at 373 K	14.8490 GPa^{-1}
Thermal conduct. k	46.6 W/(m.K)	Density ρ at 313 K	890 $\mathrm{kg/m}^3$
Specific heat c	475 J/(kg.K)	Density ρ at 373 K	876 $\mathrm{kg/m}^3$
		Thermal conduct. k	0.14 W/(m.K)
		Specific heat c	1880 J/(kg.K)
		Modulus G at 313 K	7.0 MPa
		Modulus G at 373 K	0.9 MPa
		Slope factor n at 313 K	0.570
		Slope factor n at 373 K	0.993

Table 1.5 Mesh convergence

Mesh refinement along x					Mesh refinement along y				
N_x×N_y	p_{center} (MPa)	h_{center} (μm)	h_{center} Precision (%)	Calculation Time (min)	N_x×N_y	p_{center} (MPa)	h_{center} (μm)	h_{center} Precision (%)	Calculation Time (min)
50×40	1280.1	1.084	32.7	0.82	120×60	1279.8	0.652	99.4	28.02
60×40	1279.8	0.981	48.6	1.72	120×80	1279.7	0.649	99.8	59.08
70×40	1278.1	0.902	60.8	2.07	120×100	1279.8	0.648	100	137.9
80×40	1280.9	0.833	71.5	2.63					
90×40	1281.2	0.769	81.3	3.47					
100×40	1280.8	0.723	88.4	5.87					
110×40	1281.1	0.675	95.8	7.52					
120×40	1280.9	0.658	98.5	8.68					

1.5.1 Crowned roller

The axial crowning modification is defined by a crowning radius R_y. Therefore, when the roller radius is R_x, the profile modification $g(x,y)$ is given by:

$$g(x,y) = R_x - \sqrt{\delta^2 - x^2} \tag{1.15}$$

where $\delta = R_x - \left(R_y - \sqrt{R_y^{\ 2} - y^2}\right)$.

For this section, the crowning radius is R_y = 560 mm. Figure 1.8(a) illustrates the modification. Because of the symmetry, only half of the domain is considered in the computations. This case is similar to the point contact problem, since the film thickness forms the horse-shoe shape. Figure 1.8 shows the axial film thickness, pressure and temperature at $x = 0$. The results presented in Figure 1.8 were obtained with no correction, a mirror correction and a complete correction of the free boundaries of the roller.

Figure 1.8(b) indicates that the correction effect is localized near the roller end. At $Y/L = 0.456$, the graph reveals that the 0.317 pressure estimated with no correction is reduced to close to zero as soon as the mirror or the complete correction are integrated into the calculations. At the first non-zero pressure point established with the complete correction procedure ($Y/L = 0.443$), compared to the no-correction case, the mirror correction induces a pressure reduction of 11.5%, while the complete correction reduces the pressure by 21.1%. The maximum film thickness increases are 51.7% and 69.0% at the roller end ($Y/L = 0.494$) for the mirror and complete correction, respectively. The effect of the correction procedure on the temperature is less significant, and limited to 1.2% for the mirror correction and 2.3% for the complete correction at $Y/L = 0.443$.

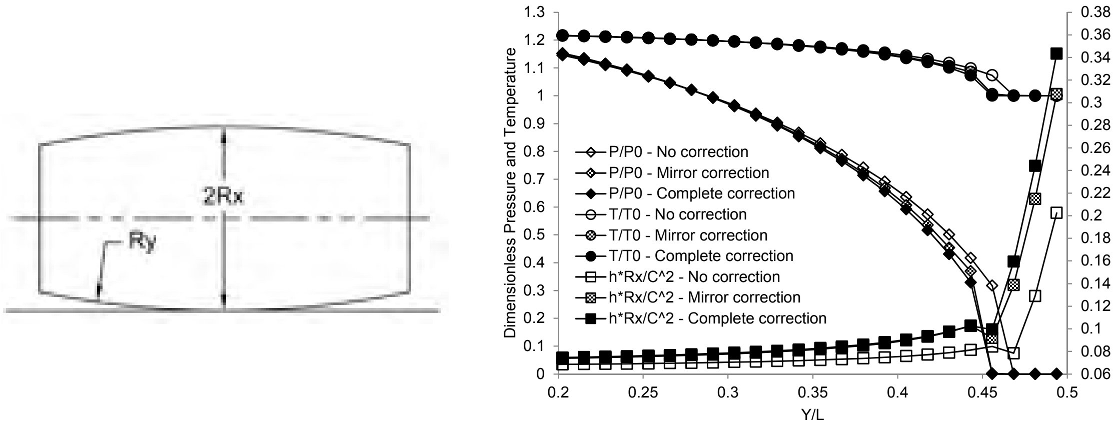

(b)

Figure 1.8 Correction effect for crowned roller

1.5.2 Roller with rounded corners

For this case, a rounding radius of 30 mm is added at a distance of 1 mm from the roller end. Figure 1.9(a) illustrates the modified roller. The curves in Figure 1.9(b) demonstrate that the lateral pressure spike is not sharp for this case. In addition, the graph shows that the 0.452 pressure estimated at $Y/L = 0.468$ with no correction is reduced to 0.183 and to zero with the mirror correction and complete correction procedures, respectively. Furthermore, at the first non-zero pressure point established with the complete correction procedure ($Y/L = 0.456$), the pressure is reduced by 11.2% with the mirror correction and by 16.0% with the complete correction, when compared to the no-correction calculations. The film thickness at the roller end ($Y/L = 0.494$) is increased by 33.3% with the mirror correction and by 47.6% with the complete correction. Finally, at $Y/L = 0.456$ the temperature values present a 0.8% and a 1.7% reduction for the mirror correction and the complete correction, respectively.

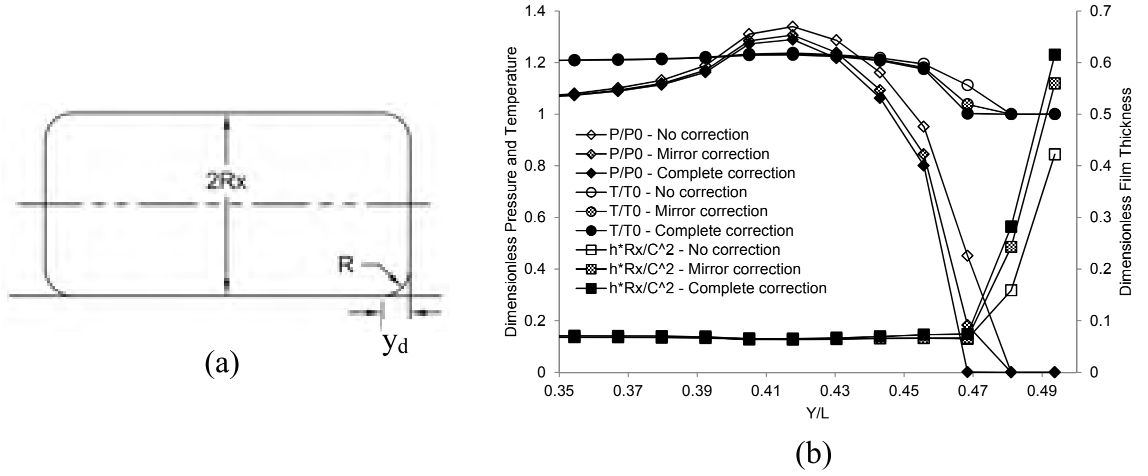

(a)

(b)

Figure 1.9 Correction effect for roller with rounded corners

1.5.3 Crowned roller with rounded corners

For this roller shape (Figure 1.10(a)), a crowned profile (R_y = 1500 mm) is combined with a rounded corner (rounding radius of 30 mm at a distance of 1 mm from the roller end). Figure 1.10 presents the pressure, the temperature and film thickness evaluations along the axial direction. For the modeled shape, the no-correction condition resulted in a 0.287 pressure at $Y/L = 0.456$, while when including the mirror or complete corrections the pressures obtained reduce to zero. At the first non-zero pressure point found with the complete correction procedure ($Y/L = 0.443$), the mirror and complete corrections produce pressure reductions of 10.6% and 15.6%, respectively, when compared with the no-correction case. At the same location, the corresponding temperature reductions are 1.2% and 1.7%. Finally, at the roller ends (at $Y/L = 0.494$), the film thickness increases by 15.1% and 21.4% when incorporating the mirror and complete corrections, respectively.

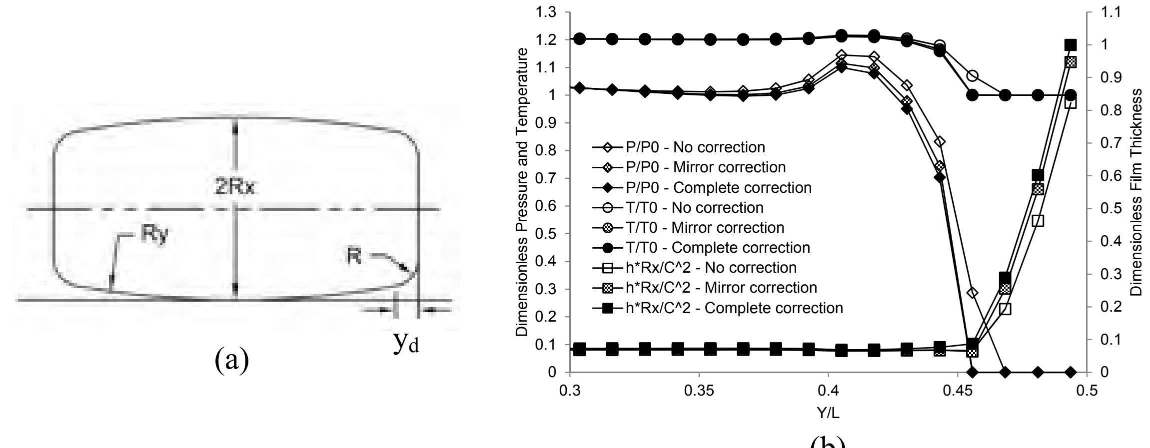

(a)

(b)

Figure 1.10 Correction effect for crowned roller with rounded corners

1.5.4 Roller with chamfered corners

This roller profile modification involves a 5° chamfering applied at a 0.5 mm distance from the roller end (Figure 1.11(a)). Figure 1.11 presents the pressure, temperature and film thickness curves. Because of the profile shape, the figure shows no considerable difference between the mirror and complete correction results. Compared to the results of the uncorrected condition at $Y/L = 0.443$, the pressure spike is reduced by 11.3%, while the temperature decreases by 2.2%, and the film thickness increases by 7.7%. More importantly, for the uncorrected free boundary condition, the results predict a complete collapse of the lubricant film close to the chamfer beginning ($Y/L = 0.456$). Nevertheless, as evaluated with the correction processes, the bodies remain separated.

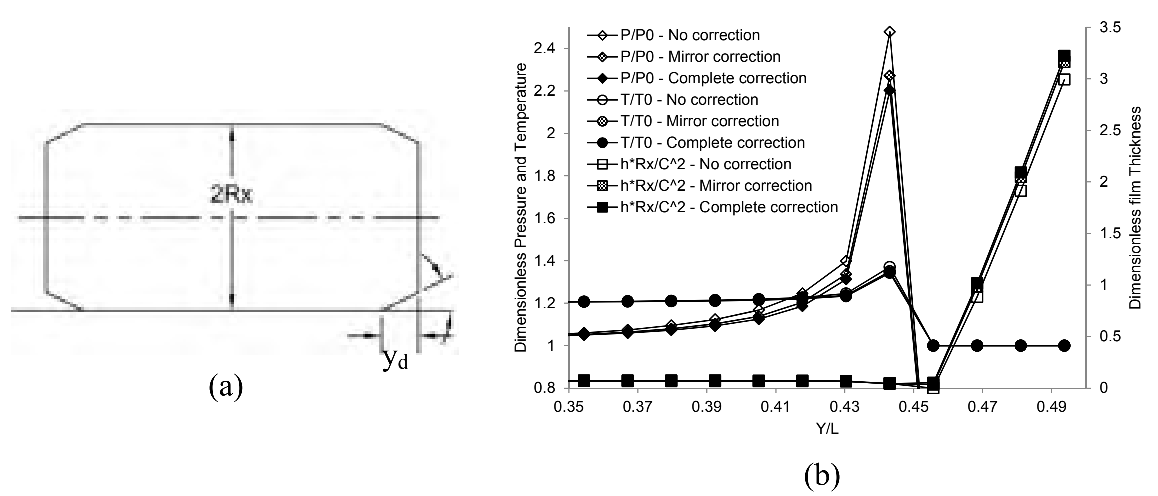

(a)

(b)

Figure 1.11 Correction effect for roller with chamfered corners

1.5.5 Logarithmic profile

This section analyzes the Lundberg profile, well known for its smoothing of pressure distributions. Although the pressure and temperature distributions are more uniform, as compared to the previous cases, a lateral film constriction remains visible. The correction process has a significant effect on the results. As shown in Figure 1.12, the estimated pressure value near the roller extremity obtained without any free boundary relief is 0.293 (at *Y/L* = 0.494), while the mirror and complete correction processes predict a null pressure at this location. At the first non-zero pressure point found with the complete correction procedure (*Y/L* = 0.481), the mirror correction generates a pressure reduction of 22.0%, when compared with the no-correction case. This reduction increases to 32.0% with the complete correction. At the same point, the maximum temperature reduction is 2.4% for the mirror correction and 4.1% for the complete correction. Moreover, the film constriction predicted at the roller boundary for the no-correction case is moved toward the center when the free boundaries are not artificially restrained. The completely corrected minimum film thickness is 9.3 times higher than the uncorrected value.

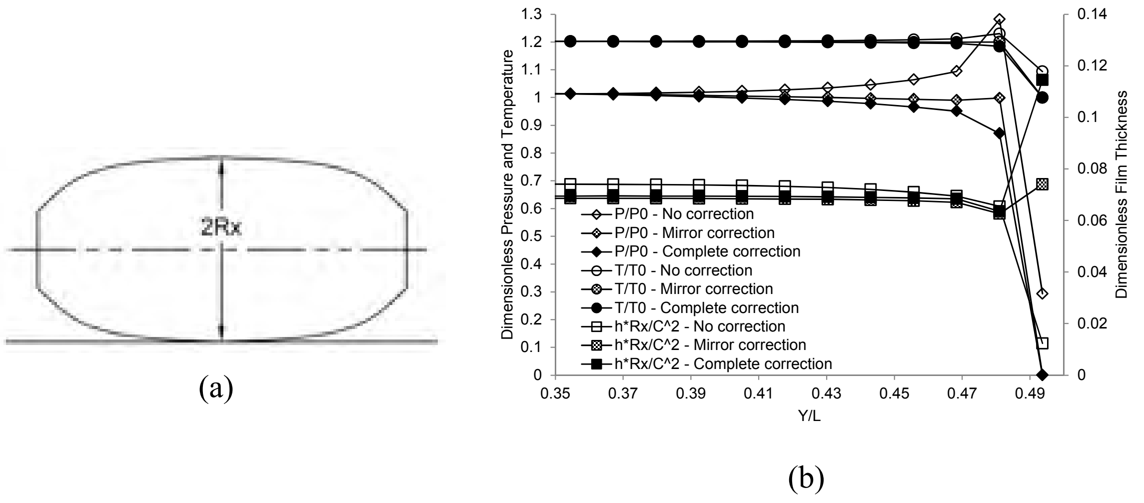
(a)
(b)

Figure 1.12 Correction effect for roller with logarithmic profile

1.5.6 Non-profiled roller

The free edge effect of non-profiled rollers is evaluated following two conditions: 1- coincident ends, and 2- non-coincident ends. These two conditions are common in cam and gear applications.

1.5.6.1 Coincident end

When the boundaries of two contacting bodies coincide, the free surface expansion causes a pressure reduction at the extremities. Figure 1.13 shows the pressure, temperature and film thickness distributions. The curves clearly indicate that the pressure drop at the boundary ($Y/L = 0.494$) is predicted only when the correction process is integrated into the simulations; the uncorrected boundary pressure is 2.6 times the pressure calculated with the mirror correction, and 4.1 times that of the complete correction. At the same point, the temperature evaluated with the no-correction condition is more than 1.2 times the temperatures evaluated with the mirror or complete correction procedures. In addition, over the $0.400 \leq Y/L \leq 0.494$

range, the average film thickness increases by 1.9 % and 4.4% with the mirror and complete correction, respectively.

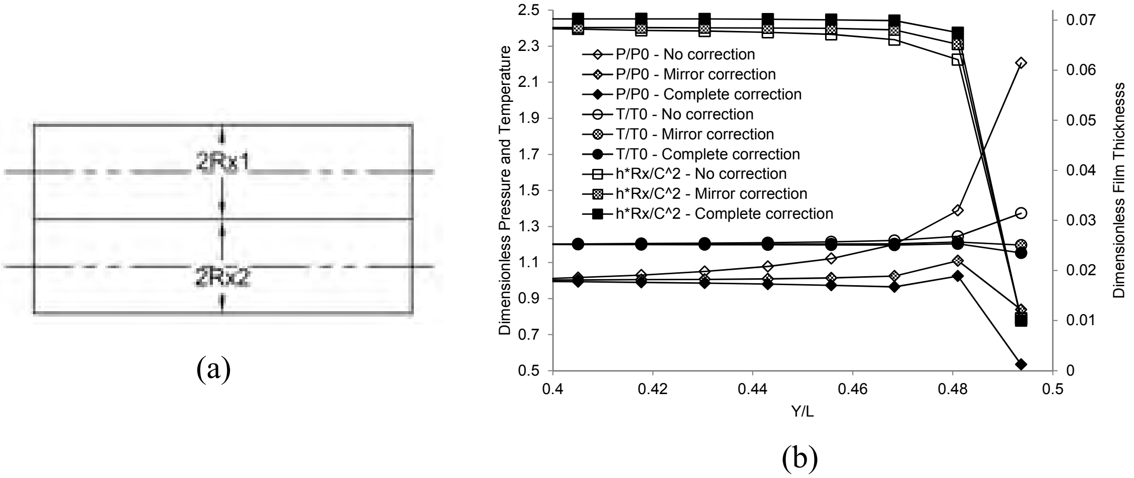

(a)

(b)

Figure 1.13 Correction effect for unprofiled coincident roller ends

1.5.6.2 Non-coincident end

This condition arises when the mating surface extends beyond the roller boundaries. In this case, the pressure domain remains unchanged. However, to simulate the influence of the longer cylinder, the flexibility matrix only integrates the mirrored pressure cells and Guilbault's correction factor for the shorter roller. Figure 1.14 presents the results. As with the previous case, the minimum film thickness occurs at the roller end ($Y/L = 0.494$). The partial mirror correction reduces the edge pressure by 37.6%, while the complete correction produces a 48.4% decrease. At the same position, the temperature calculated with the mirror and complete corrections are 92.9% and 90.5% of the non-corrected condition. Over the $0.400 \leq Y/L \leq 0.494$ range, the average film thickness increases by 1.1% and 1.5% with the mirror and complete correction, respectively.

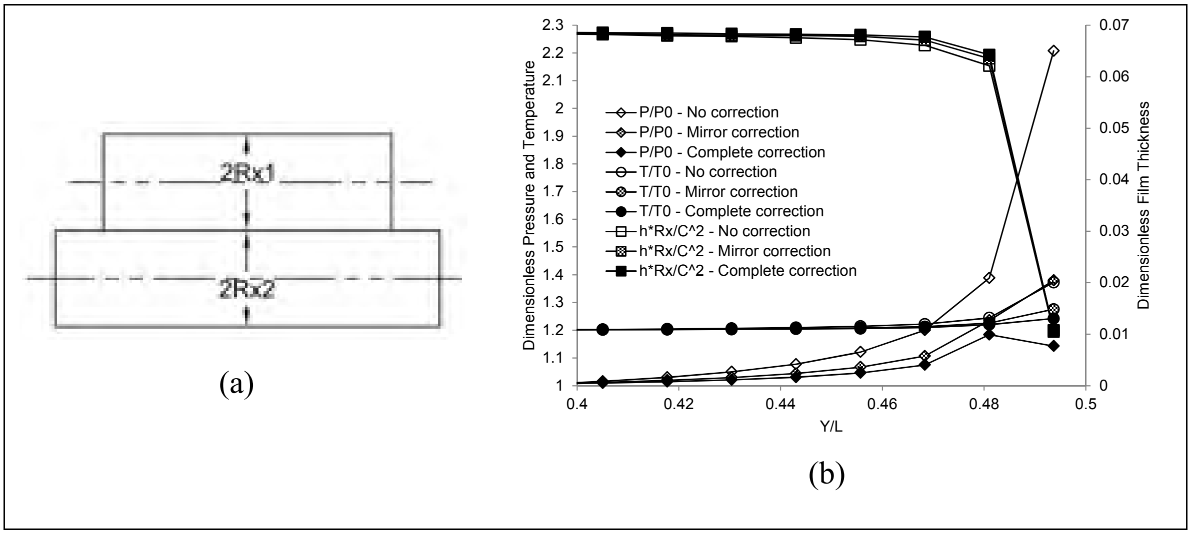

(a)

(b)

Figure 1.14 Correction effect for unprofiled non-coincident roller ends

Figure 1.15 compares the seven cases studied; the film thickness (*H*), pressure (*P*) and temperature (*T*) contour plots obtained with a complete relief of the free boundaries of the roller are juxtaposed to show the influence of the profile modification. In addition, Table 1.6 gives the film thickness, pressure and temperature values evaluated along the contact line at the mid-length position and at the constriction location.

Table 1.6 Film thickness, pressure and temperature at mid-length position and constriction location along contact line

	H (10^{-6} m)			P (GPa)			T (ºC)		
	Mid-Length	Constric.	$H_{cons.}/H_{M\text{-}L}$	Mid-Length	Constric.	$P_{cons.}/P_{M\text{-}L}$	Mid-Length	Constric.	$T_{cons.}/T_{M\text{-}L}$
Crowned	0.6643	0.9211	1.39	1.6239	0.4165	0.26	112	62.9	0.56
Rounded	0.6648	0.6031	0.91	1.2777	1.6302	1.28	103.2	112.1	1.09
Crowned with rounded	0.6607	0.6362	0.96	1.4212	1.3634	0.96	107	106.2	0.99
Chamfered	0.6594	0.3952	0.60	1.2668	2.7863	2.20	102.9	147.5	1.43
Logarithmic	0.6428	0.5893	0.92	1.3121	1.1004	0.84	104.1	97.7	0.94
Unprofiled-coincident	0.649	0.0921	0.14	1.2797	1.2959	1.01	103.2	103.7	1.00
Unprofiled-noncoincident	0.6374	0.0989	0.16	1.2358	1.4969	1.21	102	115.7	1.13

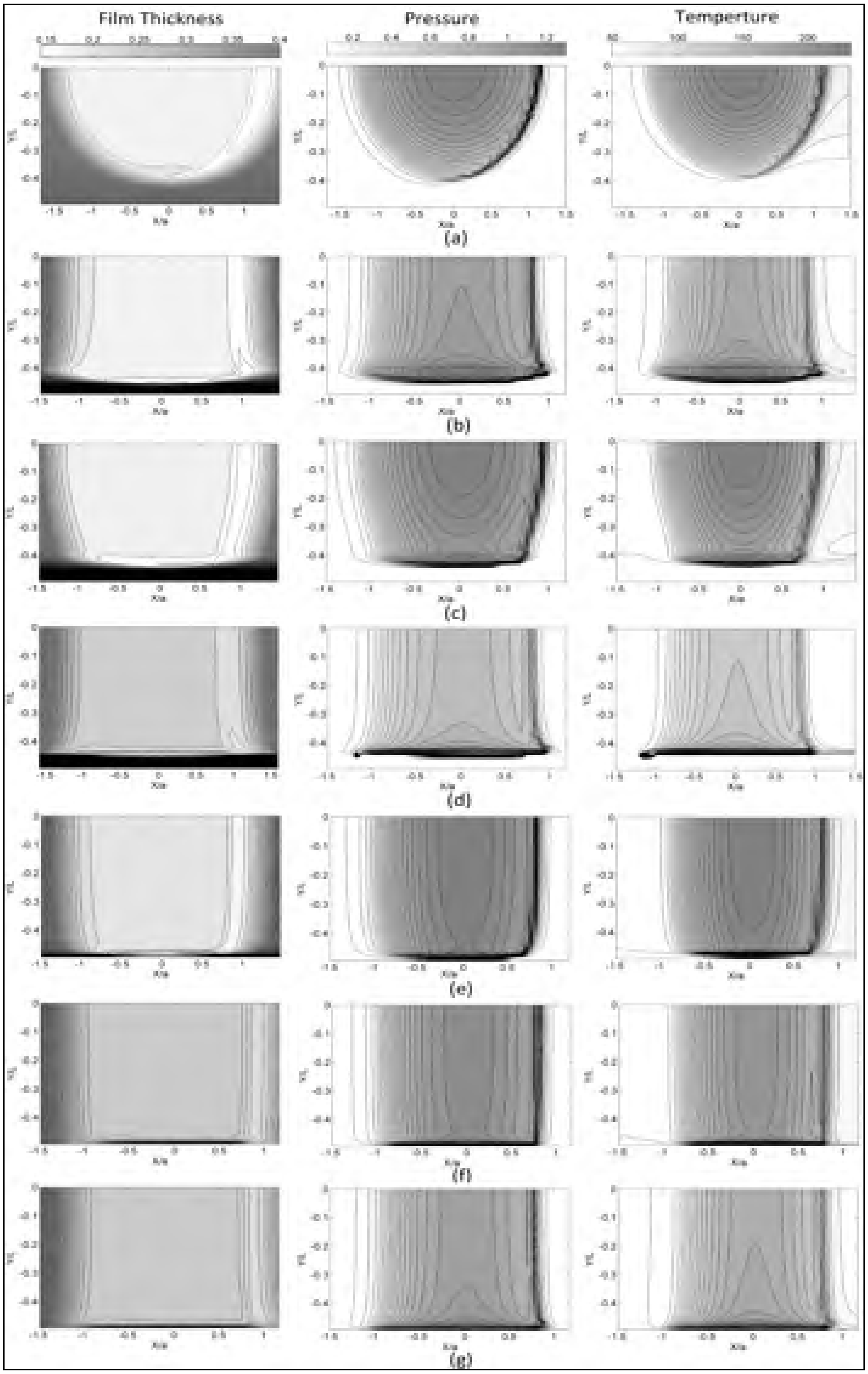

Figure 1.15 Contours of film thickness, pressure and temperature
(a) crowned, (b) rounded corners, (c) crowned with rounded corners,
(d) chamfered corners, (e) logarithmic, (f) unprofiled, coincident ends,
(g) unprofiled, non-coincident ends

The values of Table 1.6 clearly demonstrate that profiling the roller reduces the pressure and increases the film thickness at the constriction location. On the other hand, the modification has inverse consequences at the mid-length position. Therefore, it is rational to assume that an optimal profile modification would lead to a pressure ratio between the pressure at the constriction and the pressure at the mid-length position ($P_{\text{cons.}}/P_{\text{M-L}}$) being close to a unitary value. Hence, Table 1.6 shows that the crowned roller with rounded ends and the logarithmic profile are the most efficient options among the cases studied. Table 1.6 also indicates that the temperature ratio follows a behavior similar to the pressure response. Additionally, the film thickness ratio reveals that the film at the constriction position is thinner with a logarithmic modification than with a roller with a crowned rounded end. Therefore, even though the study did not involve any profiling optimization, the results suggest that a large radius crowning modification combined with rounded ends probably represents the most advantageous profile alteration.

In addition to the optimal mechanical response of the modification, since the pressure values at some points largely exceeded the 1 GPa limit of the original finite difference formulation of the Reynolds equation, Table 1.6 also demonstrates the numerical stability of the modified method promoted in this study.

1.6 Conclusions

The influence of the edge on pressure distribution has been well documented for dry contacts. Conversely, the lubrication problem involving finite contact lines has undergone much less investigation. Moreover, the high pressure condition presents a particularly challenging problem, since resolving the Reynolds equation may rapidly lead to unstable computations.

This paper has presented an efficient solution approach to the problem of thermal lubricated edge contacts submitted to high pressures. The model includes a standard finite difference solution of the energy equations, combined with a modified finite difference treatment of the Reynolds equation; to eliminate computation instability, the finite difference expansion of the Couette term of the Reynolds equation is distributed over successive iterations during the solution process. The modified iterative method results in a very stable, precise and simple calculation approach. Finally, a non-Hertzian contact representation completes the model, while the solution procedure integrates the non-Newtonian response of the lubricant by means of the Carreau expression.

The general non-Hertzian contact representation is based on the Boussinesq and Cerruti solution, complemented by a correction procedure to eliminate the shear and normal internal stresses artificially generated on the traction-free surfaces defining any finite contact line. The final contact simulation offers fast calculations and precision, and ensures a particularly efficient description of edge contact conditions.

The first sections of the paper validate and evidence the accuracy of the evaluation made with the complete thermal elastohydrodynamic model, through a comparison with experimental measurements and numerical results obtained from the literature.

The third part of the paper investigates the consequences of edge contact on the film thickness, pressure and temperature distributions. The study demonstrates the importance of an accurate representation of the free boundaries. For example, the Hartnett non-Hertzian contact model applied without any free boundary relief predicted a null film thickness at the contact edge of the chamfered roller. Conversely, both Hetényi's partial mirror correction and complete procedures indicated that while presenting a substantial constriction, the film thickness separates the surfaces along the complete contact line. Likewise, for the straight rollers with non-coincident ends, the pressure distributions reveal the significant consequence of an inadequate treatment of the free boundaries; at the constriction position, the partial mirror correction reduces the pressure evaluation by 37.6%, while the complete relief showed a reduction of 48.4% as compared to the non-corrected conditions. Similarly, with coincident ends, the non-corrected representation leads to pressure overestimations of 160% and 310%, as compared to partial mirror correction and complete correction, respectively. The obvious influence of the free boundary calls for precise modeling. Therefore, since the combination of the correction factor of Guilbault (2011) with the Hetényi shear stress correction does not increase the calculation times, and offers accurate estimations, the procedure is recommended for reliable descriptions of elastohydrodynamic conditions of finite contact lines.

The last part of the study utilizes the proposed thermal model to investigate the influence of axial profiling. The analysis includes seven common roller profile forms and contact conditions. In summary, the simulations show that chamfering the ends generates high-pressure concentration, leading to a complete collapse of the film thickness close to the chamfer beginning. On the other hand, assuming that an optimal profiling should produce constant maximum pressure along a contact line, the well-known logarithmic modification and a crowning profiling combined with a rounding of the corner were shown to offer the best pressure distributions. In addition, the crowned with rounded corner profile also ensures a more uniform film thickness along the contact line. Hence, the simulations presented suggest that a large radius crowning modification combined with a rounding of the corners probably represents the most effective profile adjustment.

CHAPITRE 2

ARTICLE 2: MODELING THE EDGE CONTACT EFFECT OF FINITE CONTACT LINES ON SUBSURFACE STRESSES

Morteza Najjari and Raynald Guilbault

Department of Mechanical Engineering, École de technologie supérieure,
1100 Notre-Dame Street West, Montréal, Québec, Canada H3C 1K3

This Article was published in Tribology International Journal in June, 2014

2.1 Abstract

Finite contact line conditions lead to subsurface stress distributions determined by the free boundaries. Combined with a correction procedure, Semi-Analytical Methods (SAMs) accurately include the free boundary effects, and represent a rapid alternative to the Finite Element Method (FEM) for contact pressure calculation. This paper extends the free boundary correction procedure to the evaluation of surface and subsurface stresses from SAMs. The investigation integrates a validation based on a two-level factorial comparison confronting the stress distributions established with the developed procedure to results obtained from FEM models. The comparison examines three dimensionless factors, and shows that the stress distributions are evaluated with a high level of precision. The model also offers evaluation more than 125 times faster than FEM simulations.

Keywords: subsurface stresses, finite line contact, edge influence, quarter-space.

2.2 Introduction

Non-conformal contact interfaces undergo severe stress fields (Sadeghi, Jalalahmadi et al. 2009). Finite contact line conditions existing in applications such as gears or cams may present additional stress concentrations close to the associate free boundaries and resulting edges (Najjari and Guilbault 2014). Under Hertzian conditions, the maximum shear defining the contact critical area appears at a short distance beneath the surface. The presence of free boundaries, asperity contact or sliding (non-Hertzian contact) may affect the location of the maximum value of the stresses (Bold, Brown et al. 1992; Olver 2005). However, under any conditions, the surface and subsurface stress distributions are controlling factors of the contact fatigue life. Therefore, accurate rolling contact fatigue life prediction requires precise descriptions of stress fields near discontinuity zones (Lundberg and Palmgren 1947; Lundberg and Palmgren 1949; Littmann and Widner 1965; Elsharkawy and Hamrock 1991; Ioannides, Bergling et al. 1999; Nélias, Champiot et al. 1999; Dong, Ning et al. 2009).

Since contact pressure distribution evaluation is essential for obtaining the surface and subsurface stress fields, under non-Hertzian contact conditions, numerical modeling becomes inevitable. The Finite Element Method (FEM) often appears as the easiest approach. Nevertheless, obtaining the necessary precision requires very fine FEM meshes, normally resulting in prohibitive calculation times. Alternatively, semi-analytical methods (SAMs) based on the Boussinesq-Cerruti solution for point tractions acting on elastic half-space represent an efficient way to deal with the pressure distribution problem. The half-space assumption also offers closed-form expressions for stress calculation (de Mul, Kalker et al. 1986; Johnson 1987). However, this approach is obviously unable to account for finite contact interfaces, and, consequently, leads to non-realistic values close to or at the contact extremities. Hence, when applied to such conditions, SAMs need to be corrected. For the pressure calculation, Hetényi (Hetenyi 1960; Hetényi 1970) proposed the application of virtual mirrored pressures for shear stress elimination and an iterative treatment for normal stress correction. Recently, Guilbault (Guilbault 2011) introduced a correction factor (Eq. 2.1) which multiplies the mirrored pressures to simultaneously correct the shear and normal stress influence on the surface displacements. Compared to the complete Hetényi process, because it eliminates the iterative treatment, this last procedure drastically reduces the calculation times. Once the corrected pressure distribution is established, the surface and subsurface stresses may be evaluated with the closed-form expressions available in the literature (Love 1929; M'Ewen 1949; Smith and Liu 1954; Sackfield and Hills 1983; Kalker 1986; Ahmadi, Keer et al. 1987; Sourty, Sullivan et al. 2002). However, to the author's knowledge, the literature provides no particular adaptation procedure for those expressions, and therefore, the underlying half-space assumption once again leads to unsound stress evaluations close to the body limits.

$$\psi = 1.29 - \frac{1}{1-\nu}(0.08 - 0.5\nu) \tag{2.1}$$

This paper introduces a simple complementary correction procedure for surface and subsurface stress evaluation in real delimited bodies. The study includes a validation section in which a two-level factorial comparison incorporating three dimensionless factors confronts the stress distributions established with the developed procedure to results obtained from FEM models.

2.3 Contact of two elastic bodies

2.3.1 Pressure distribution

The general dry contact problem resolution procedure is well described and validated in Ref. (Guilbault 2011). In the present paper, the contact pressure distributions are obtained from the same algorithm. Figure 2.1 illustrates the procedure when applied on two of the free boundaries (F_{b1} and F_{b2}) of a roller/rectangular body contact problem: the solution domain is divided into constant pressure cells of lengths $2a$ and $2b$ in the x and y directions, and the flexibility matrix written for the resulting mesh. Equation 2.2 gives the flexibility coefficients for a cell ij of the surface, when a pressure (P) is applied on a cell kl. In order to account for the body limits, the pressure cells are mirrored with respect to the free boundaries (P' for F_{b1} and P'' for F_{b2}), and their influence integrated into the flexibility matrix. The first correction eliminates the free boundary artificial shear stress. To remove the remaining normal stress influence, each mirror cell contribution is multiplied by Guilbault's factor (ψ, Eq. 2.1) prior to its integration into the flexibility matrix. This last operation completely releases the boundaries. Equation 2.3 establishes the relation between the pressure distribution and the surface displacement at position (i, j).

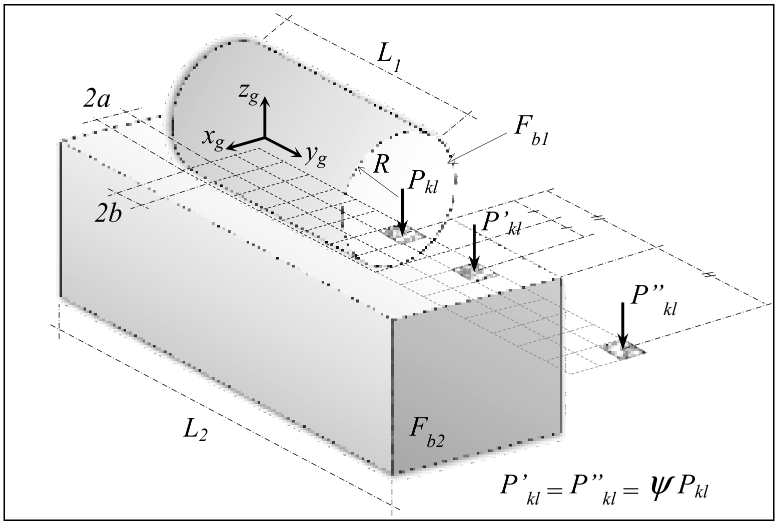

Figure 2.1 Roller and rectangular body contact

$$f_{ij,kl} = \left\{ \begin{array}{l} (x_{ik}+a)\ln\left[\dfrac{(y_{jl}+b)+\sqrt{(x_{ik}+a)^2+(y_{jl}+b)^2}}{(y_{jl}-b)+\sqrt{(x_{ik}+a)^2+(y_{jl}-b)^2}}\right]+ \\ (x_{ik}-a)\ln\left[\dfrac{(y_{jl}-b)+\sqrt{(x_{ik}-a)^2+(y_{jl}-b)^2}}{(y_{jl}+b)+\sqrt{(x_{ik}-a)^2+(y_{jl}+b)^2}}\right]+ \\ (y_{jl}+b)\ln\left[\dfrac{(x_{ik}+a)+\sqrt{(x_{ik}+a)^2+(y_{jl}+b)^2}}{(x_{ik}-a)+\sqrt{(x_{ik}-a)^2+(y_{jl}+b)^2}}\right]+ \\ (y_{jl}-b)\ln\left[\dfrac{(x_{ik}-a)+\sqrt{(x_{ik}-a)^2+(y_{jl}-b)^2}}{(x_{ik}+a)+\sqrt{(x_{ik}+a)^2+(y_{jl}-b)^2}}\right] \end{array} \right\} \tag{2.2}$$

$$u_{ij} = \left(\frac{1-\nu^2}{\pi E} \right) \sum_{k=1}^{n_x} \sum_{l=1}^{n_y} f_{ij,kl} \, p_{kl} \tag{2.3}$$

2.3.2 Stress distribution

The expressions for the surface and subsurface stress produced by a contact pressure acting on a rectangular patch on the surface of an elastic half-space were first presented by Love (Love 1929). Based on these expressions, the stress tensor at any point $p(x_p, y_p, z_p)$ of the half-space resulting from pressures distributed over constant pressure cells *kl* is written as presented by Eqs. 2.4 to 2.10 (Sourty, Sullivan et al. 2002):

$$\sigma_{mn}\Big|_{\bar{x},\bar{y},\bar{z}} = \left(\frac{1}{2\pi} \right) \sum_{k=1}^{n_x} \sum_{l=1}^{n_y} p_{kl} \begin{pmatrix} A_{mn}(\bar{x}+a,\bar{y}+b,\bar{z}) + A_{mn}(\bar{x}-a,\bar{y}-b,\bar{z}) \\ -A_{mn}(\bar{x}-a,\bar{y}+b,\bar{z}) - A_{mn}(\bar{x}+a,\bar{y}-b,\bar{z}) \end{pmatrix} \tag{2.4}$$

With

$$A_{xx}(x,y,z) = 2\nu \left[\tan^{-1}(\frac{xz}{y\zeta}) - \tan^{-1}(\frac{x}{y}) \right] - \tan^{-1}(\frac{y}{x}) + \tan^{-1}(\frac{yz}{x\zeta}) + \frac{xyz}{\zeta(x^2+z^2)} \tag{2.5}$$

$$A_{yy}(x,y,z) = 2\nu \left[\tan^{-1}(\frac{yz}{x\zeta}) - \tan^{-1}(\frac{y}{x}) \right] - \tan^{-1}(\frac{x}{y}) + \tan^{-1}(\frac{xz}{y\zeta}) + \frac{xyz}{\zeta(y^2+z^2)} \tag{2.6}$$

$$A_{zz}(x,y,z) = -\tan^{-1}(\frac{y}{x}) - \tan^{-1}(\frac{x}{y}) + \tan^{-1}(\frac{yz}{x\zeta}) + \tan^{-1}(\frac{xz}{y\zeta}) - \frac{xyz}{\zeta(x^2+z^2)} - \frac{xyz}{\zeta(y^2+z^2)} \tag{2.7}$$

$$A_{xy}(x,y,z) = (2\nu-1)\ln(\zeta+z) - \frac{z}{\zeta} \tag{2.8}$$

$$A_{xz}(x,y,z) = \frac{yz^2}{\zeta(x^2+z^2)} \tag{2.9}$$

$$A_{yz}(x,y,z) = \frac{xz^2}{\zeta(y^2+z^2)} \tag{2.10}$$

where $\zeta = \sqrt{x^2+y^2+z^2}$, $\overline{x} = x_k - x_p$, $\overline{y} = x_k - y_p$ and $\overline{z} = z_p \quad (z_p \geq 0)$.

Figure 2.2 shows the 3D stress state obtained for a quarter-space defined by one free boundary, when treated with the previous equation. As before with the pressure calculation, the half-space assumption generates artificial normal and shear stresses on the free surface. In reality, σ_{yy}, σ_{yz} and σ_{yx} are null at the free boundary. Therefore, once the pressure distribution is evaluated, the stress distribution computation also demands a free boundary stress elimination.

As suggested by Hetényi (Hetenyi 1960; Hetényi 1970), mirroring the pressure eliminates the shear stress σ_{yz}. Actually, since the pressure distribution resulting from the correction procedure for the contact surface displacement along the z-axis (section 2.2) incorporates the mirrored pressure influence, the final σ_{zz}, σ_{yz} and σ_{yx} distributions are also shaped by these mirror pressures. Their contribution is therefore combined to the pressure cell contribution for the evaluation of Eqs. 2.7, 2.8 and 2.10.

The free boundary normal stress σ_{yy} effect on the contact surface rigidity is compensated by an overcorrection of the shear contribution introduced by the correction factor ψ (Eq. 2.1). However, ψ exerts no real influence on σ_{yy}. On the other hand, as demonstrated by Hetényi (Hetenyi 1960; Hetényi 1970), this stress component could be eliminated from the free surface by the addition of an inverse analogous distribution. Nevertheless, since compared to σ_{yz} and σ_{zz} the influence of σ_{yy} remains of lower importance, and in order to optimize the calculation times, it seems preferable to simply set σ_{yy} to zero all over the free surface. Its distribution in the *y*-axis direction remains however to be corrected; the plane stress state close to the free boundary evolves to a plain strain state towards the internal body positions. The body shape and dimensions of the stress-affected region control this transition. Since σ_{yy} shows more or less a constant amplitude along the *y*-axis, the present analysis merely considers that the reduction from the inner body region towards the zero value at the free boundary follows a constant radius curved transition. To account for the body shape and stress-affected region, this radius is fixed at γ times the contact half-width (γ C). All calculations below considered γ to be equal to 15. Section 2.4.5 examines and validates this choice.

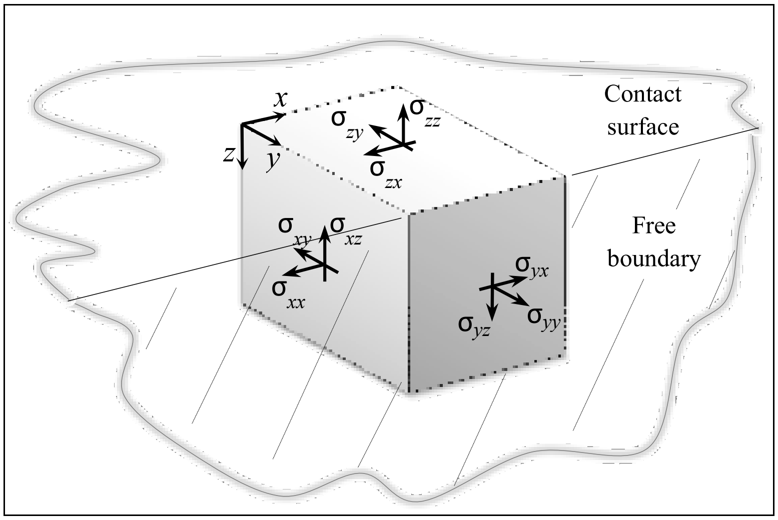

Figure 2.2 3D stress state

2.4 Stress model validation

The finite element method is recognized for its general precision and reliability. This study considers that with sufficiently fine meshes, contact FEM models offer valuable estimates of the contact pressures and associated stress distribution. This validation section compares the results obtained from the proposed model to FEM values. The analysis integrates a two-level factorial comparison combining three dimensionless factors. The dimensionless approach generalizes the validation. The factors are the contact slenderness $S_l = R/L_1$, the contact length ratio $L_{rc} = L_2/L_1$ and the load $W = w/(E'L_1R)$, where $E' = \left(\frac{1-\upsilon_1^2}{E_1} + \frac{1-\upsilon_2^2}{E_2} \right)^{-1}$. In all the following simulations, the material properties are E=200 GPa and ν=0.3 for both bodies.

2.4.1 Geometry definition

The two-level factorial comparisons with three factors leads to the eight cases defined in Table 2.1. To cover the coincident and non-coincident end conditions, L_{rc} is set to 1 and 1.4, while with values of 0.2 and 2, S_l describes long and short roller problems. Finally, W equals 1.036×10^{-5} and 9.366×10^{-5} which represents maximum Hertzian pressures of 200 and 600 MPa, respectively. The studied cases are designated by descriptive abbreviations: *C* and *NC* correspond to coincident and non-coincident ends, respectively, while *S* and *L* indicate short or long roller conditions. The maximum Hertzian pressure completes the designation. For example, the S600NC case corresponds to a short roller, a 600 MPa maximum Hertzian pressure and non-coincident end condition.

Table 2.1 Case studies

	$L_{rc} = 1$		$L_{rc} = 1.4$	
W	$S_l = 2$	$S_l = 0.2$	$S_l = 2$	$S_l = 0.2$
1.036×10^{-5}	S200C	L200C	S200NC	L200NC
9.366×10^{-5}	S600C	L600C	S600NC	L600NC

2.4.2 FEM model preparation

All 3D FEM analyses were realized with the ABAQUS software. Figure 2.3 shows a sample model of the non-coincident end condition. Using the *xz* and *yz* symmetry planes, the quadratic wedge element (15 nodes) meshes only integrate a quarter of each body. The models also assure a smaller element size close to the free boundaries by means of a bias division approach. The non-coincident end conditions generate local singularities, which under purely elastic simulations lead to stress concentration increases inversely proportional to the element size. Therefore, to compensate for the plastic deformation influence neglected in the FEM models, the mesh size in the singularity region was decreased until the calculated pressure reached a maximum value of 1.7 times the yield strength (contact elastic limit based on the Tresca criteria). It was assumed that local plastic deformation would redistribute the load and maintain the pressure below this elastic-plastic transition. This strategy resulted in minimum element lengths of 12.5 μm and 35 μm along the radial and axial directions, respectively. The following validation imposes the same contact elastic limit to the proposed modeling approach. In all simulations, the bottom surface of the lower body was fixed, while the load was applied on the top surface of the upper body. Finally, the contact interfaces assured frictionless conditions.

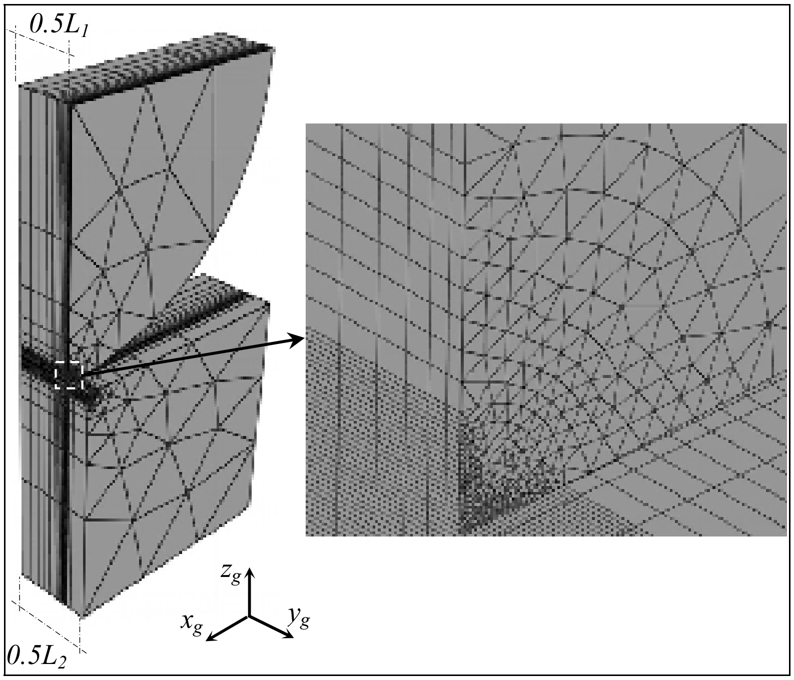

Figure 2.3 FEM model

2.4.3 Surface and subsurface stress results

Figure 2.1 illustrates the model tangent plane division in contact cells. For purposes of comparison, this tangent plane meshing is adjusted to the FEM mesh sizes (60 divisions along *x* and 30 along *y* for all cases). For the FEM simulations, 30 divisions along the *z*-axis complete the model. As with the FEM models, the proposed modeling approach also incorporates a bias factor in the *y* direction. However, since this approach offers a higher precision level than the FEM for contact modelling, the bias factor is simply adjusted to produce the free edge pressure obtained from the FEM models.

To illustrates the model precision for pressure calculation, Figure 2.4(a) compares the half-contact width pressure distribution obtained at the mid-section (*y*=0) for cases S200C and S600C to the Hertz theory and FEM results, whereas 2.4(b) presents the maximum pressure values along the contact lines close to the free boundary zones for the coincident end case, S200C, and the non-coincident condition, S200NC. The charts in Figure 2.4 show a high correspondence among the results, and, therefore demonstrate the reliability of the correction procedure proposed in Ref. (Guilbault 2011).

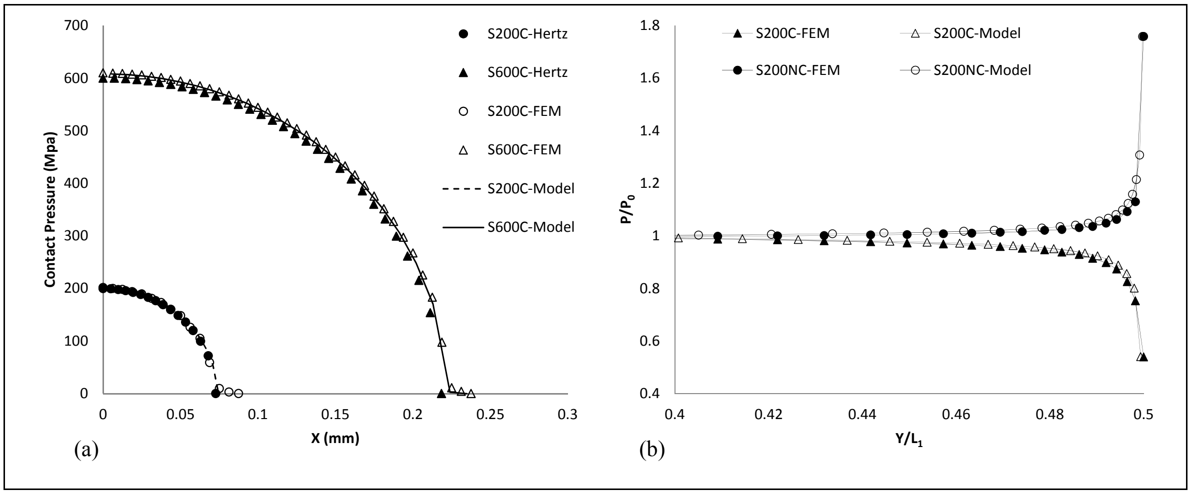

Figure 2.4 Pressure comparison (a) mid-section (*y* = 0), (b) along the contact lines (*x* = 0)

Figure 2.5 plots the subsurface stresses calculated at the mid-section of the S200C case. The average differences for σ_{xx}, σ_{yy}, σ_{zz} and the maximum shear stress (τ_{max}) are 1.5%, 5.2%, 0.3% and 0.2%, respectively. Figure 2.6 shows the equivalent curves at the free surface of the upper body. The corresponding average differences for σ_{xx}, σ_{zz} and τ_{max} are 0.6%, 5% and 10.4%. However, since τ_{max} plays a significant role in rolling contact fatigue, it is important to mention that the correspondence between the proposed model and the FEM simulation at the τ_{max} maximum value is 96.6%. The surface stresses along the centerlines are depicted in Figure 2.7. The curves indicate that the plane strain-to-plane stress transition assumption leads to a good agreement between the model and FEM results; the average differences in Figure 2.7 are limited to 3.2%, 7.8%, 0.3% and 6.8% for σ_{xx}, σ_{yy}, σ_{zz} and τ_{max}, respectively.

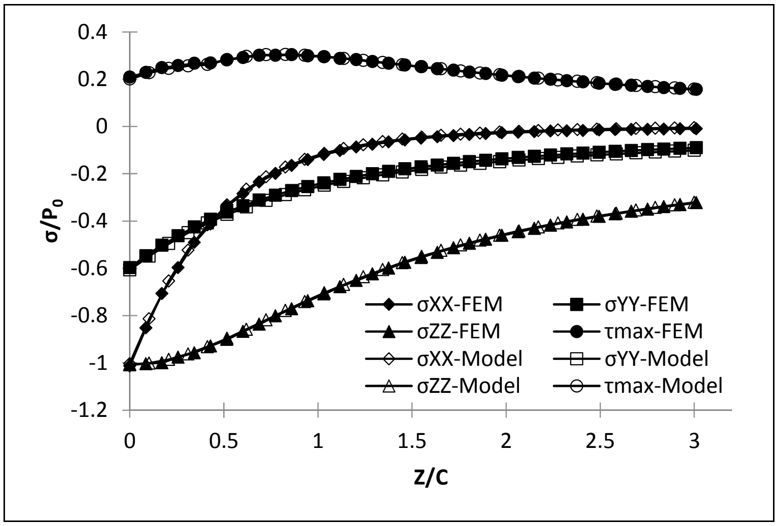

Figure 2.5 Internal subsurface stresses at mid-section - S200C

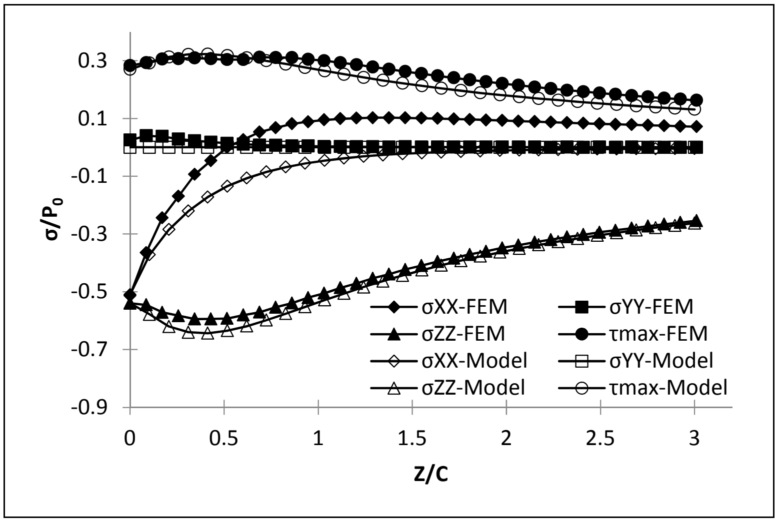

Figure 2.6 Subsurface stresses at upper body free boundary (*y*=0.5L_1) - S200C

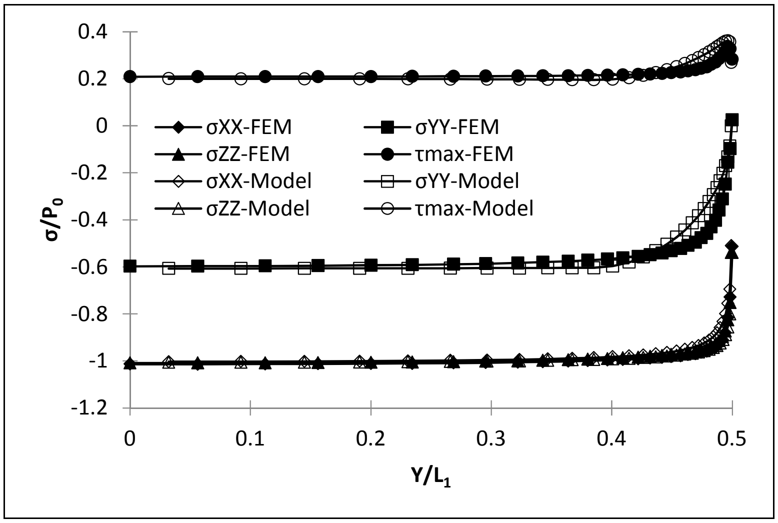

Figure 2.7 Surface stresses along the contact lines (*x*=0) - S200C

To illustrate the model capacities for the non-coincident end problem, Figures 2.8 to 2.10 present the subsurface and surface stress distributions established for S200NC. Since the stress distributions at the mid-section remain unaffected compared to the coincident end conditions, the chart is not repeated. Figure 2.8 plots the internal stresses calculated below the contact line in the lower body at the upper body free surface position (beneath the stress concentration). The corresponding average differences for σ_{xx}, σ_{yy}, σ_{zz} and τ_{max} are 4.3%, 6.1%, 3.9% and 4.0%, respectively. Figure 2.9 shows the same stresses calculated for the upper body (at the free surface). For this case, the average differences are 3.9% and 11% for σ_{zz} and $\tau_{\max}$, respectively. On the other hand, the average difference for σ_{xx} reaches 34.8%. However, again for this problem, the maximum value established for τ_{max} remains in good agreement with the FEM evaluation, with the difference being less than 2%. In reality, the maximum value of τ_{max} is mainly determined by σ_{zz}. Therefore, a precise evaluation of this stress component is vital. Figure 2.10 presents the surface stress distribution along the contact lines. Again, the curves reveal a high correspondence; the average differences for σ_{xx}, σ_{yy}, σ_{zz} and τ_{max} are 1.6%, 1.5%, 3.3% and 2.7%, respectively.

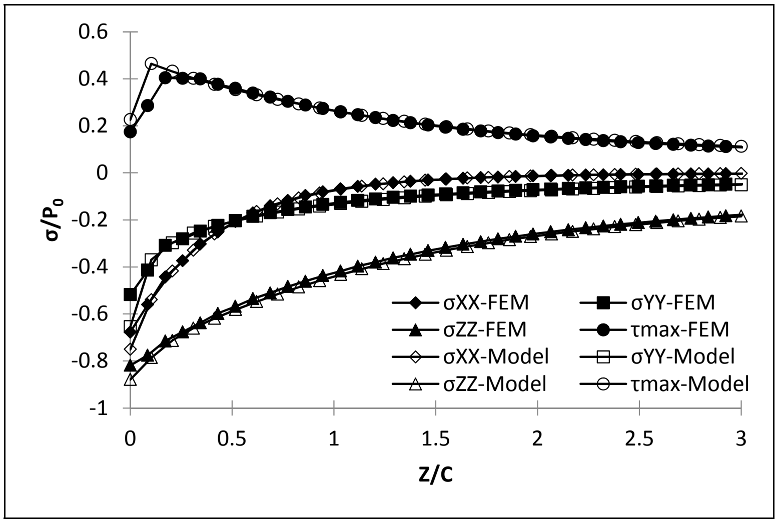

Figure 2.8 Lower body internal subsurface stresses at stress concentration zone (y=0.5L_1) - S200NC

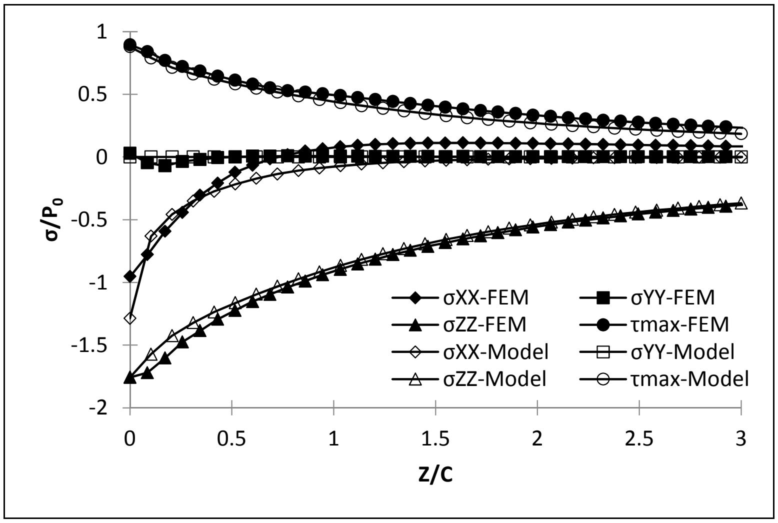

Figure 2.9 Upper body subsurface stresses at free surface (y=0.5L_1) - S200NC

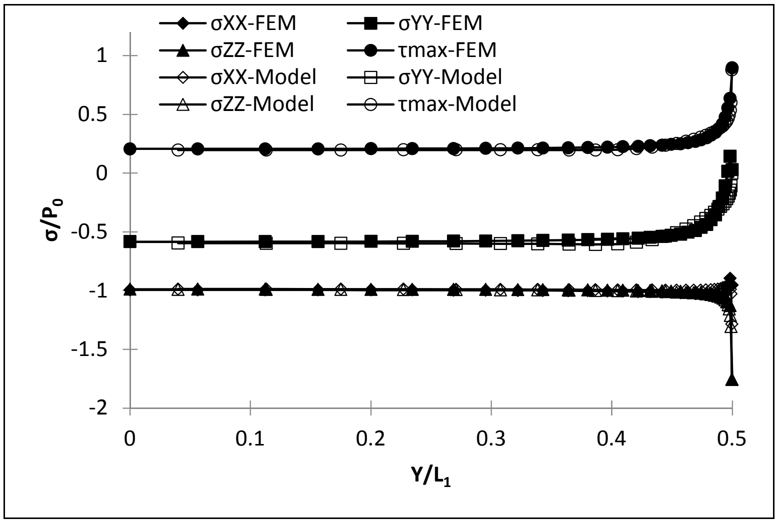

Figure 2.10 Surface stresses along contact lines (x=0) - S200NC

2.4.4 Dimensionless factor influence

This section examines the average relative difference between the model and FEM results for all cases in Table 2.1. The following graphs compare the stress distribution difference in percentage at the positions chosen in the previous section: the mid-section (y=0), the free boundary of the upper body and the corresponding position in the lower body (y=0.5L_1), for the subsurface stress distributions and along the contact lines (x=0) for the surface values.

Figure 2.11 shows the internal mid-section average subsurface stress differences. As demonstrated by the charts, σ_{xx}, σ_{zz} and τ_{max} present evaluations in close agreement (more than 96%) with the FEM reference results. Although the correspondence remains higher than 89%, σ_{yy} demonstrates slightly more apparent variations.

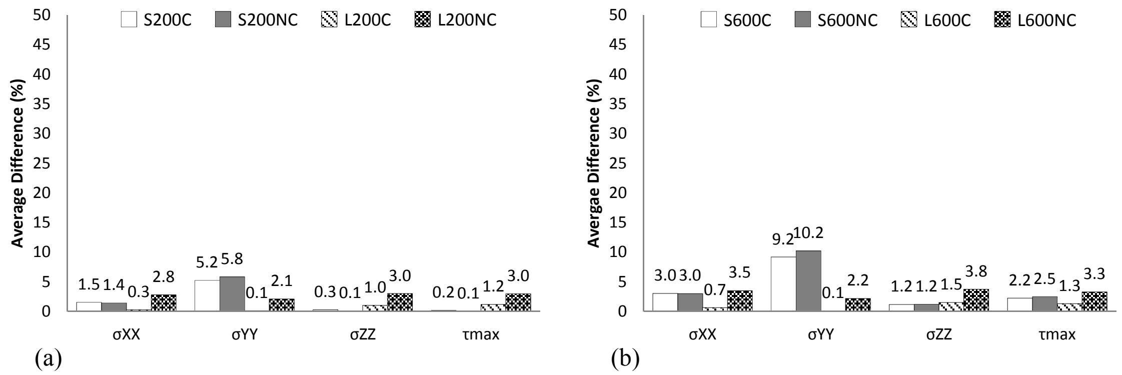

Figure 2.11 Internal subsurface stress comparison at mid-section (a) $W = 1.036\times10^{-5}$, (b) $W = 9.366\times10^{-5}$

Figure 2.12 describes the situation at the upper body free boundary (y=0.5L_1). Since the σ_{yy} values at this position are set to zero, the graphs do not include this component in the comparison. On the other hand, the proposed model includes no special adjustment for σ_{xx}. Therefore, under the non-coincident end conditions, it generates the more visible differences. However, considering the information given in Figure 2.9, we see that even with the highest relative variation of all stress components, the σ_{xx} distribution remains close to the reference FEM evaluations. The two other investigated stresses, σ_{zz} and τ_{max}, demonstrate high agreement for all eight studied dimensionless configurations: above 89% and 92% for the lower and higher loads, respectively.

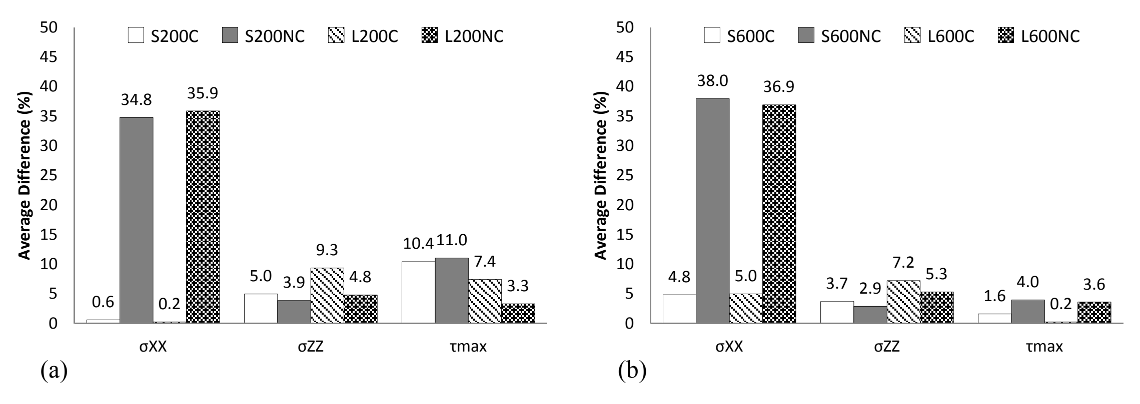

Figure 2.12 Subsurface stress comparison at upper body free boundary
(a) $W = 1.036{\times}10^{-5}$, (b) $W = 9.366{\times}10^{-5}$

Figure 2.13 compares the internal subsurface stresses calculated at the stress concentration zone in the lower body. The global correspondence is greater than 83%. Moreover, the σ_{zz} and τ_{max} evaluations appear to be even more precise, with a maximum difference of 12%. This maximum difference occurs with the L200NC case. However, increasing W or reducing S_l reduces this variation.

Finally, Figure 2.14 shows the differences evaluated at the surface along the contact lines. The maximum pressures are also included in the graphs. The precision demonstrated for this parameter is above 94%. The component σ_{zz}, which is controlled by the pressure, presents the same precision. The σ_{xx} evaluations also present values similar to the FEM results (above 96%). Moreover, the arc-form reduction of σ_{yy} towards the free boundary offers a good trend description, with a minimum correspondence higher than 88%. Finally, the surface evaluation of τ_{max} shows a precision higher than 91%. However, since the rolling contact fatigue problem is controlled by the maximum value of τ_{max} located beneath the surface, the real precision of τ_{max} should be evaluated from Figures 2.11 to 2.13. Figures 2.12 and 2.13 indicate that the proposed model assures a minimum precision higher than 88% when compared to the FEM results.

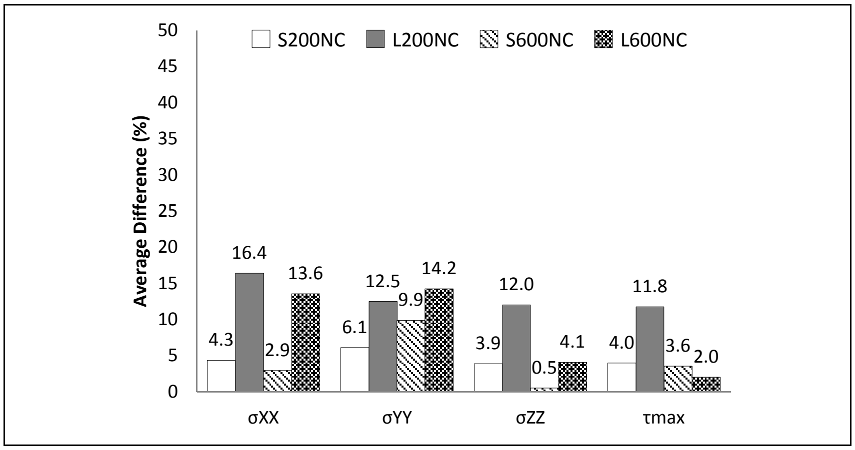

Figure 2.13 Lower body internal subsurface stress comparison at stress concentration zone (y=0.5L_1)

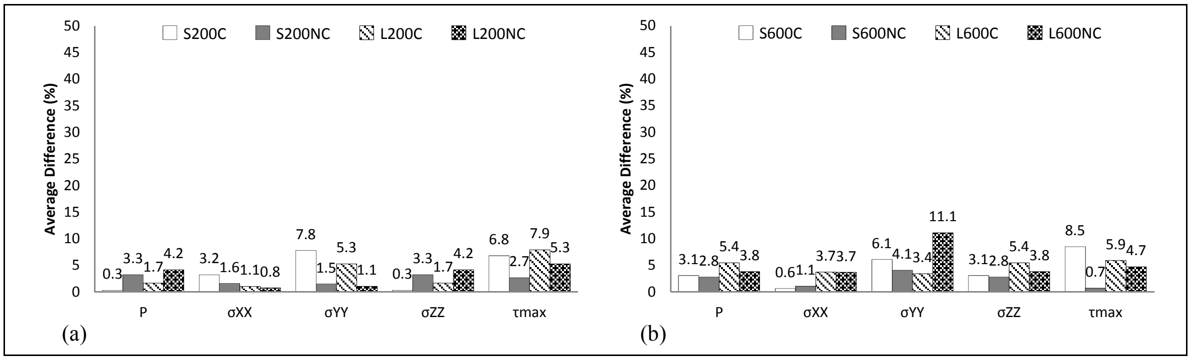

Figure 2.14 Surface stress comparison along contact lines
(a) $W = 1.036\times10^{-5}$, (b) $W = 9.366\times10^{-5}$

2.4.5 Plane strain to plane stress transition

In order to maintain high computation speeds, the results presented in the previous sections simulated the σ_{yy} evolution from a plane strain to a plain stress state towards the free boundary with a constant radius curved transition set to λC, with λ=15. The results showed that this assumption is suitable for the dimensionless cases of Table 2.1. To conclusively verify the acceptability of this approach, the FEM calculations presented below examine eight new dimensionless configurations taken outside the domain defined by the factor range of Table 2.1. Figure 2.15 illustrates the study domain. Since L_{rc} corresponds to the coincident or non-coincident end conditions, this factor remains fixed at the same values L_{rc} =1 or 1.4. The first four cases (1 to 4) evaluate the slenderness influence with S_l=0.1 and 4, while W is maintained at a mid-domain load of (4.162×10^{-5}), leading to a contact pressure of 400 MPa. The following four cases examine the load influence; W is set to (2.602×10^{-6}) and (2.602×10^{-4}) to generate contact pressures of 100 MPa and 1000 MPa, while S_l is fixed at the mid-domain value of 1.1. Figure 2.15 presents the studied configuration, where points 1 to 8 correspond to the following designations: case 1: S400C, case 2: L400C, case 3: S400NC, case 4: L400NC, case 5: M100C, case 6: M1000C, case 7: M100NC, and case 8: M1000NC.

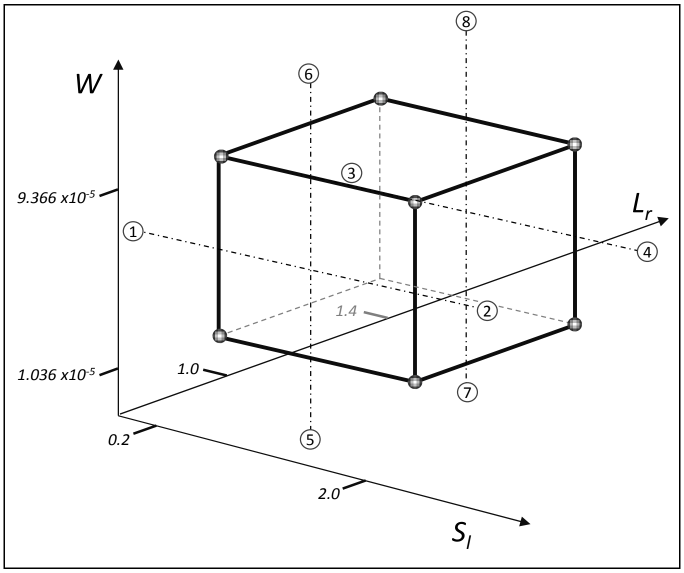

Figure 2.15 Dimensionless cases

The resulting σ_{yy} distributions established along the contact lines for both cases of Table 2.1 and the eight new cases are drawn in the graphs in Figure 2.16. This figure clearly demonstrates that, following an arc-form reduction, the σ_{yy} value reaches more than 90% of its central amplitude on average, at a distance close to 15 times the semi-width of contact (C). Therefore, the simple assumption of a constant radius curved reduction for σ_{yy} in the transition zone appears to be a good estimation of the real behavior.

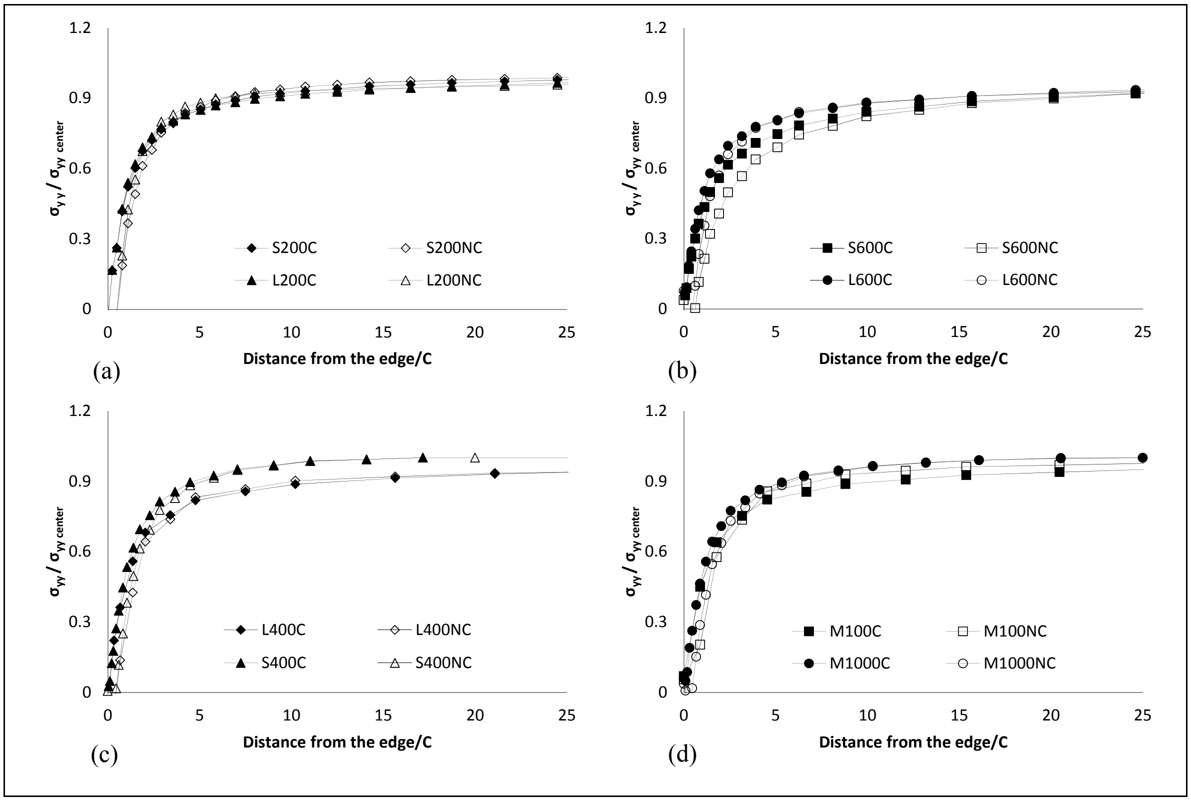

Figure 2.16 Plane strain-to-plane stress transition zone
(a) $W = 1.036\times10^{-5}$, (b) $W = 9.366\times10^{-5}$, (c) $W = 4.162\times10^{-5}$,
(d) $W = 2.602\times10^{-6}$ and $W = 2.602\times10^{-4}$

2.4.6 Calculation time comparison

The previous sections demonstrated the good precision levels obtained from the proposed correction procedure. However, the real worth of the method also largely depends on the associated calculation times. All the studied cases were solved on the same computer with the proposed model and by FEM simulations, concurrently. The FEM representation was optimized to offer converged solutions with the lowest computation times. On the other hand, the current model meshes were refined to reach the FEM precision on pressure estimates, and to assure calculation points at positions close to FEM nodes. On average, the FEM models involved 20,000 elements and 60,000 nodes. Table 2.2 reports the solution times obtained with both modeling approaches for the Table 2.1 cases. Table 2.2 clearly shows that the presented free boundary treatment established the contact pressure and associated subsurface stress distributions, by far faster than the FEM models. In fact, Table 2.2 indicates that, on average, the proposed model is more than 125 times faster than FEM simulations.

Table 2.2 CPU time(s)

Case	S200C	S200NC	L200C	L200NC	S600C	S600NC	L600C	L600NC
Model	25.5	47.6	26.3	47.4	25.1	48	25.9	47.7
FEM	3392	4307	3598	3943	4880	5247	4436	5090

2.5 Conclusion

Free boundary conditions have a dominant influence on the surface and subsurface stress distributions of finite line contact problems. Because when corrected to integrate the free boundaries, SAMs based on the half-space theory offer accurate and rapid evaluation of the contact interface displacements and pressure distribution, this paper extends the free boundary correction procedure to the surface and subsurface stress calculations in real delimited contact problems: with z normal to the contact interface, y in the direction of the principal axis of the contact area, and x perpendicular to y and z, once the pressure distribution is determined, virtual mirror pressures added to incorporate the free boundary influence on the displacement are also integrated in the σ_{zz}, σ_{yz} and σ_{yx} evaluation, whereas the normal (to the free boundary) component σ_{yy} is simply set to zero. The axial evolution σ_{yy} from a plane strain at the mid-section to a plane stress condition close to the free boundary is also corrected; the analysis demonstrates that the distribution follows an arc-form reduction from the inner body region towards the zero value at the free surface. The first observations suggested a radius equal to $15C$. This estimation was later verified and validated through FEM analyses; the proposed axial behavior offers a trend description in conformity with the FEM representation.

A comparison between FEM evaluations and the values resulting from the developed model also demonstrates the global precision of the complete procedure. A two-level factorial comparison constructed with three dimensionless factors (the contact slenderness S_l, the contact length ratio L_{rc} and the load W) generalizes the validation. The studied domain includes short and long rollers, coincident and non-coincident end conditions, while the W levels correspond to maximum Hertzian pressures of 200 and 600 MPa.

The σ_{xx}, σ_{zz} and τ_{max} comparison shows that at the contact area mid-position, the average correspondence between the proposed model and the FEM reference results is greater than 96%, while the correspondence for σ_{yy} remains greater than 89% for all studied dimensionless configurations. The σ_{zz} and τ_{max} distributions obtained at the free boundary of the upper body (y=0.5L_1) also demonstrate a high concordance with the FEM estimates: above 89% for the lower loads and 92% for the higher loads. At the corresponding position inside the lower body, the overall correspondence with FEM results remains above 83%, while the σ_{zz} and τ_{max} individual agreement presents a minimum value of 88%.

The developed correction procedure also offers very fast evaluations. A comparison of the calculation times obtained for the eight dimensionless configurations considered in this study indicated that the proposed approach established the contact pressure and associated stress distributions at least 125 times more rapidly than the FEM avenue. Therefore, this model certainly presents a powerful modeling option, particularly suited for profile optimization of rolling elements involving iterative search processes.

CHAPITRE 3

ARTICLE 3: FORMULA DERIVED FROM PARTICLE SWARM OPTIMIZATIONS (PSO) FOR OPTIMUM DESIGN OF CYLINDRICAL ROLLER PROFILE UNDER EHL REGIME

Morteza Najjari and Raynald Guilbault

Department of Mechanical Engineering, École de technologie supérieure,
1100 Notre-Dame Street West, Montréal, Québec, Canada H3C 1K3

This Article was submitted to the Journal of Mechanism and machine theory in May, 2014

3.1 Abstract

Roller profile corrections play an important role in EHL load capacity of cylindrical contacts. Recently, the authors demonstrated that when considering pressure distribution uniformity, crowning modifications combined with rounded corners offer similar performances to that of logarithmic profiles, while conceivably being less difficult to manufacture. This paper develops formulas establishing crowning and corner rounding radii for rapid design of optimal roller. These formulas amalgamate results obtained from multi-objective particle swarm optimizations (PSO) completed over a five-level dimensionless factorial design, with the factors being the slenderness, the load and the lubricant viscosity. Since the PSO optimizations integrated three concurrent objective functions: the contact pressure uniformity, the film thickness stability, and the maximum load capacity, the formula predictions guarantee optimal profile corrections.

Keywords: Optimum roller profile, thermal EHL, multi-objective, particle swarm optimization.

3.2 Introduction

The axial crowning of cylindrical rolling elements prevents contact pressure concentration near the extremities and compensates for slight misalignments (Hamrock and Anderson, 1983). A circular crowning profile eliminates edge stress concentrations at low to moderate loads, but develops edge effects under heavy loads. On the other hand, logarithmic profiling of rollers not only removes edge effects at low, medium and heavy loads, but also results in nearly uniform axial pressure distributions (Rahnejat and Gohar, 1979; Johns and Gohar, 1981). Recently, the authors of the present work studied the influence of edge contacts on thermal elastohydrodynamic lubrication (EHL) for different roller contact conditions, and demonstrated that a large radius crowning modification combined with a rounding of the corners is as effective as a logarithmic profile, while being probably easier to produce (Najjari and Guilbault, 2014).

Mechanical design problems relate to the sizing of machine elements to certain precise requirements. However, the numbers of unknowns (generally geometric dimensions) are commonly larger than the number of governing equations, thus leading to infinite numbers of potential solutions. In such situations, some of the unknowns may be assigned values based on experience or on the literature, and the system for the remaining unknowns solve. This strategy does not however guarantee optimal designs. On the other hand, optimization techniques allow the adjustment of more than one variable at a time, and therefore, the generation of the best solutions. This study implements a particle swarm optimization (PSO) approach to optimize the three geometric parameters defining a crowning profile correction, namely, the crowning radius, the rounding radius and the rounded corner distance. An optimal cylindrical roller profile design maximizes the load capacity, and offers uniform contact pressures and stable film thickness distributions along the roller length.

Many optimization research studies on various machine elements have been reported (Seireg, 1972), but very few documents have investigated rolling contact elements. Using a gradient-based search method, Seireg and Ezzat (1968) optimized the bearing length, radial clearance and average lubricant viscosity of a hydrodynamic journal bearing. Their design objective was to minimize both the oil supply and the temperature rise. Maday (1970) and Wylie and Maday (1970) studied optimum configurations for hydrodynamic bearings; they applied bounded variable methods to maximize the load carrying capacity of bearings. Later, Hirani et al. (2000) presented a design method for selecting the optimal diametric clearance and length of an engine journal bearing. The procedure controls the minimum film thickness, the maximum pressure and the maximum temperature. On the other hand, because of larger deformations, higher temperatures and piezoviscous effects, EHL conditions existing in roller bearings usually result in more complex tribological conditions.

Changsen (1991) described the application of a gradient-based numerical optimization technique to the design of cylindrical roller bearings. The author identified five design parameters to be optimized: the fatigue life, the wear life, the static load rating, the frictional moment and the spin-to-roll ratio. Since contact bearing fatigue degradation is the main failure mode in rolling, Changsen finally suggested a single-objective function, namely, the basic dynamic capacity with associated geometric constraints. Changsen also put forward the concept of the multi-objective optimization of rolling element bearings. More recently, evolutionary algorithms have been applied to the optimal design of rolling contact bearings. Chakraborty et al. (2003) employed a binary-coded genetic algorithm to solve Changsen’s formulation for maximizing the fatigue life of deep-groove and tapered-roller bearings. However, some of the considered optimization constraints later appeared to be unrealistic, and therefore, Rao and Tiwari (2007) introduced practical constraints. Kumar et al. (2009) developed an optimum design for cylindrical roller bearings with the help of real-coded genetic algorithm. They chose the basic dynamic load rating as the objective function, and included the roller profiling effect. Two logarithmic profile generating parameters were also considered. The optimization results showed that the multiplier of the logarithmic profile deviation parameter has a greater effect on the fatigue life, as compared to other geometric parameters. Gupta et al. (2007) used a genetic algorithm in a multi-objective framework for the design optimization of a deep-groove ball bearing. The authors simultaneously optimized three primary factors: the basic dynamic load rating, the basic static load rating and the EHL minimum film thickness. Savsani et al. (2009) later used a modified particle swarm optimization (PSO) approach to solve the same problem, and reported better results, compared to those of Gupta.

This paper develops formulas for the rapid design of optimal roller profiles. The formulas for their part derive from optimal results obtained during a multi-objective PSO campaign conducted with a five-level factorial design. This factorial design combines two dimensionless factors: the slenderness and the load, complemented by the lubricant viscosities of three mineral oil ISO grades (ISO-VG 100, 220 and 460). The final formulas establish the optimal crowning and corner rounded shape for rollers of any slenderness and load, resulting in EHL conditions inside the studied domain. The analysis validates the formulas through a comparison of the pressure and film thickness distributions for three lubricants, each with four combinations of slenderness and load selected in between the design evaluation points.

3.3 Thermal EHL model for rolling contacts with edge effects

The investigation presented by Najjari and Guilbault (2014) describes the edge effects of finite contact lines on thermal EHL. Using an accurate description of the free boundaries, the thermal EHL model developed by them offers precise simulations of edge contact conditions. The model also incorporates the Carreau expression to describe the shear-thinning response of the lubricant. Table 3.1 gives the roller material and lubricant properties considered by Najjari and Guilbault (2014). The present study makes use of the model developed by Najjari and Guilbault (2014), and integrates the lubricant shear-thinning properties provided in Table 3.1.

Table 3.1 Roller and lubricant properties, (Najjari and Guilbault, 2014)

Roller		**Lubricant**	
Diameter D_{eq}	12.0 mm	Ambient temperature T_0	313 K
Young modulus E	200 GPa	Visc.-Press. coef. α at 313 K	20.2031 GPa^{-1}
Poisson ratio ν	0.3	Visc.-Press. coef. α at 373 K	14.8490 GPa^{-1}
Density ρ	7850 kg/m^3	Density ρ at 313 K	890 kg/m^3
Thermal conduct. k	46.6 W/(m.K)	Density ρ at 373 K	876 kg/m^3
Specific heat c	475 J/(kg.K)	Thermal conduct. k	0.14 W/(m.K)
		Specific heat c	1880 J/(kg.K)
		Modulus G at 313 K	7.0 MPa
		Modulus G at 373 K	0.9 MPa
		Slope factor n at 313 K	0.570
		Slope factor n at 373 K	0.993

3.4 Particle swarm optimization algorithm

The PSO algorithm introduced by Eberhart and Kennedy (1995) belongs to the intelligent optimization technique group. The algorithm is inspired by a bird swarm searching for optimal food sources. In PSO, the moving direction of every single bird is influenced by 1- its current movement, 2- the best food source it found so far, and 3- the best food source any bird in the swarm ever experienced. In other words, the particles move based on their inertia, their personal knowledge and the social knowledge of the swarm. An important review published by Poli et al. (2007) describes the major developments and applications in the domain.

PSO initiates the process with a randomly distributed population of particles (potential solutions) over the search domain. Each particle is represented by its position $x_i = (x_{i0}, x_{i1}, \ldots, x_{iD})$, where D is the dimensionality of the problem. Its displacement velocity is written as $v_i = (v_{i0}, v_{i1}, \ldots, v_{iD})$. In order to prevent any escape from the search space, the particle velocity is also controlled by a limiting value ($v_{\max}$). For each particle i, the previous optimal position (last best fitness) is stored in $pbest_i = (pbest_{i0}, pbest_{i1}, \ldots, pbest_{iD})$. Among $pbest_i$, the swarm global best value is identified as $gbest = (gbest_0, gbest_1, \ldots, gbest_D)$. For each iteration, the new velocity and position of the particles are expressed as:

$$v_{id}^{new} = \omega \times v_{id}^{old} + c_1 \times r_1 \times (pbest_{id} - x_{id}^{old}) + c_2 \times r_2 \times (gbest_d - x_{id}^{old}) \tag{3.1}$$

$$x_{id}^{new} = x_{id}^{old} + v_{id}^{new} \qquad i = 1, 2, \ldots, n\,, \quad d = 1, 2, \ldots, D \tag{3.2}$$

where, n is the number of particles in the swarm, ω is the inertia weight, c_1 and c_2 are learning factors, and r_1 and r_2 are random numbers between 0 and 1. The impact of the previous velocity on the current one is controlled by ω. In other words, ω controls the global and local exploration abilities of the particles. A value between 0.8 and 1.2 has been reported to offer a promising balance between performance and convergence rate (Shi and Eberhart, 1998). Engelbrecht (2007) showed that a linear variation between 0.4 and 0.9 also offers an efficient alternative.

In the present analysis, c_1 and c_2 are set to 1.49618 and ω equals 0.72984. These values were set based on the article published by Clerc and Kennedy (2002) for multi-dimensional complex spaces. Moreover, as suggested by Cheng-San et al. (2008), to prevent premature convergence (stagnation), a virtual global best position vector (*vgbest*) is produced by averaging the previous best positions $pbest_i$ (Eq. 3.3). The fitness of this virtual best position is subsequently compared to that of the global best position *gbest*, and if the fitness of *vgbest* is better than the value representing *gbest*, *gbest* is replaced by *vgbest* in Eq. 3.1.

$$vgbest_d = \frac{\sum_{i=1}^{n} pbest_{id}}{n} \tag{3.3}$$

Schoene, Ludwig et al. (2012) proposed a procedure to handle particle escapes from the search space. The strategy simply returns the escapee particle back to the search space following the breakout path through a series of iterations producing backward displacements. Eq. 3.4 formulates the correction procedure:

$$\bar{x}_{id}^{k+1} = \bar{x}_{id}^{k} - \bar{v}_{id}^{k+1} \qquad k = 0, 1, ..., N \tag{3.4}$$

Where N is the limit number of correcting iterations and $\bar{v}_{id}^{k+1}$ is the corrected velocity calculated as:

$$\bar{v}_{id}^{k+1} = \alpha \bar{v}_{id}^{k} \qquad k = 0, 1, ..., N \tag{3.5}$$

Where α is a correction factor. The initial corrected position $\bar{x}_{id}^{0}$ is set to the first position x_{id}^{new} outside the search space, while the initial corrected velocity $\bar{v}_{id}^{0}$ is set to the velocity v_{id}^{new} that caused the particle breakout. Eq. 3.4 is solved iteratively until the particle position returns to the search space or until the limit number of iteration *N* is reached. Based on empirical tests, the authors suggested values of α = 0.54 and *N* = 4.

The swarm size is often set empirically based on the dimensionality and perceived difficulty of the problem. The literature (Poli, Kennedy et al., 2007) suggests values between 20-50. In this study, the swarm size (n = 25) is determined by a swarm density refinement process described later. Finally, the convergence criterion terminates the search after ten consecutive iterations of fitness fluctuations inferior to 1%. The following pseudo-code presents the PSO algorithm.

Algorithm 3.1 Particle swarm optimization

```
initialize randomly distributed swarm
for each particle in swarm do
    evaluate fitness
    $pbest_{id} = x_{id}^{0}$
    if fitness of $pbest_{id}$ is better than fitness of $gbest_{d}$ then
        $gbest_{d} = pbest_{id}$
    end
end
calculate $vgbest_{d}$ from Eq. 3.3
if fitness of $vgbest_{d}$ is better than fitness of $gbest_{d}$ then
    $gbest_{d} = vgbest_{d}$
end
while (number of iterations, or convergence criteria is not met) do
    for each particle in swarm do
        calculate $v_{id}^{new}$ from Eq. 3.1
        if $abs(v_{id}^{new})$ is greater than $v_{max}$ then
            $v_{id}^{new} = sign(v_{id}^{new}) \times v_{max}$
        end
        update new position from Eq. 3.2
        if $abs(x_{id}^{new})$ is greater than $x_{max}$ then
            correct new position from Eqs. 3.4 and 3.5
        end
        evaluate fitness
        if fitness of $x_{id}^{new}$ is better than fitness of $pbest_{id}$ then
            $pbest_{id} = x_{id}^{new}$
        end
        if fitness of $x_{id}^{new}$ is better than fitness of $gbest_{d}$ then
            $gbest_{d} = x_{id}^{new}$
        end
    end
    calculate $vgbest_{d}$ from Eq. 3.3
    if fitness of $vgbest_{d}$ is better than fitness of $gbest_{d}$ then
        $gbest_{d} = vgbest_{d}$
    end
end
```

3.5 Design variables

Figure 3.1 defines the crowned roller with rounded corners geometry. The characteristics of the roller profile can be defined by three dimensionless variables: the crowning radius $r_c = R_c / L$, the rounding radius $r_r = R_r / L$ and the rounded corner length $r_l = L_{ro} / L$.

In order to illustrate the profile form influence, Figure 3.2 presents along the roller half-length the axial pressure distributions and the central film thicknesses evaluated for different types of profiles. As shown in the graph, with a straight *Un-profiled* roller, a pressure spike appears near the roller extremities, producing a constriction resulting in a lubrication film thickness reduction close to a breakdown. On the other hand, while significantly increasing the central pressure, a *Crowned* profile eliminates the pressure spike at the roller end. The profile identified as *Rounded corners* exhibits a pressure spike near the roller effective length end similar to the un-profiled case. Moreover, the oil film shows a complete collapse, while the reduction of load carrying length of the roller causes higher pressure values. Figure 3.2 also includes a crowned with rounded corners form. The graphs demonstrate that this modification can reduce the pressure spike at the roller end and eliminate the associated lubricant film thickness reduction, while the pressure distribution contains no excessive central increase. In light of these examples, the properties characterizing an optimal roller profile design can be defined as follows. An optimal profile should:

1. flatten the pressure distribution and minimize the spike at the roller ends;
2. flatten the lubricant film distribution and maximize its thickness;
3. maximize the load capacity.

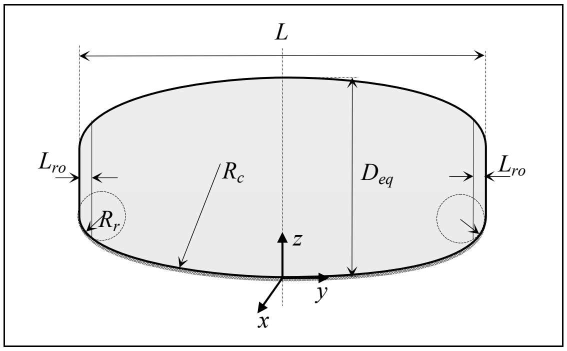

Figure 3.1 Roller geometry

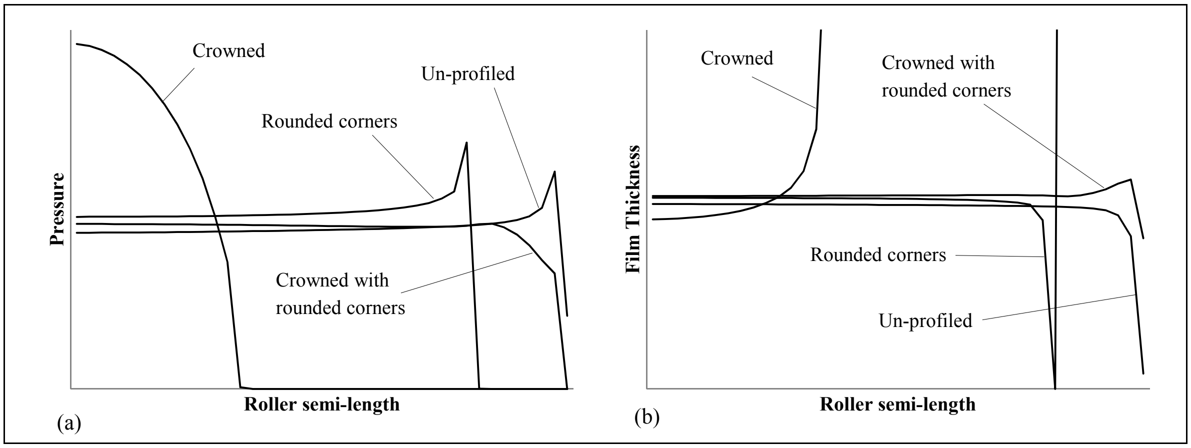

Figure 3.2 Profile effect on axial distribution of: (a) pressure, (b) central film thickness

The above properties lead to the following mathematical interpretation: the ratios P_{spike} /P_0, $H_{const.} /H_c$ and P_0 /P_{Hertz} should all be close to a unitary value. P_0 and P_{spike} are the maximum pressures at the roller center and at the pressure spike close to the roller ends, respectively. P_{Hertz} is the maximum Hertzian contact pressure established for an infinite contact line. H_c and H_{const} are the central film thickness and the film thickness at the constriction, respectively. These ratios can then be combined to form the fitness function presented in Eq. 3.6. An optimal profile form will therefore minimize this expression:

$$f(r_c, r_r, r_l) = \left|1 - \frac{P_{spike}}{P_0}\right| + \left|1 - \frac{H_{const.}}{H_c}\right| + \left|1 - \frac{P_0}{P_{Hertz}}\right| \tag{3.6}$$

The scrutinized space should be large enough to include all potential optimal solutions. The crowning radius (r_c) range starts from a reduction of the line contact to point contact conditions generating a maximal pressure equal to 1.3 times P_{Hertz}, and goes up to the quasi straight roller conditions defined by an R_c maximal value equal to 1.0e6 mm. The lower bound of the rounding radius (r_r) is set equal to the rolling radius $0.5D_{eq} = 0.5(D_1^{-1} + D_2^{-1})^{-1}$ where D_1 and D_2 are the diameters of cylinder 1 and 2, respectively. The upper bound is limited to 500 times the roller length. The rounded corner length (r_l) covers the no-rounded-corner conditions to 0.2 times the roller length. The studied ranges are then $\frac{w^2 E'^4}{1.5L(4\pi R_x(1.3P_{Hertz})^2)^3} \le r_c \le 1.0\times10^6 / L$, $R_x / L \le r_r \le 500$ and $0 \le r_l \le 0.2$. These ranges are initial limits, and could be extended whenever the search process tends to identify a global optimum outside the initial domain.

The five-level factorial design assembled for the prediction formula preparation includes two dimensionless factors: the contact slenderness $S_l = D_{eq}/L$ and the load $W = w/E'LD$, where $\frac{2}{E'} = \frac{1-\nu_1^2}{E_1} + \frac{1-\nu_2^2}{E_2}$. In order to cover the long and short roller conditions, the considered S_l values are 0.2, 0.4, 0.6, 0.8 and 1. W equals 1.63×10^{-5}, 3.66×10^{-5}, 6.50×10^{-5}, 1.02×10^{-4} and 1.46×10^{-4}. These loads represent maximum Hertzian pressures of 500, 750, 1000, 1250 and 1500 MPa, respectively. The optimization process is conducted for three mineral oils of ISO viscosity grade 100, 220 and 460. Table 3.2 gives the corresponding viscosities for two reference temperatures.

Table 3.2 Constituent lubricant viscosities (Pa s)

Temperature (K)	ISO VG		
	100	220	460
313	0.089000	0.195800	0.409400
373	0.009636	0.016640	0.026280

3.6 Optimization results

Preparatory swarm density refinements established the appropriate swarm size. The objective was to reduce the search process time, while preserving the optimization quality. Figure 3.3(a) shows the global fitness variation obtained with different swarm sizes. The charts indicate that swarms larger than 20 particles do not significantly improve the final global fitness (Eq. 3.6). Moreover, to better illustrate the swarm size influence, Figure 3.3(b) presents the r_c evaluations obtained with five swarm sizes as a function of the iteration number. The graph shows that all sizes converged to the same r_c, indicating therefore that PSO successfully found the global optimum. The curves also reveal that compared to 20 particles, a swarm size of 25 significantly reduces the number of iterations required to find the optimal r_c, while further increasing the number of particles roughly involved similar numbers of iterations to reach an equivalent precision. Therefore, in this study, the swarm size was set to 25 particles. Moreover, in order to increase the confidence level, three optimization runs were realized for each evaluated case, and the best solution selected as the optimal configuration.

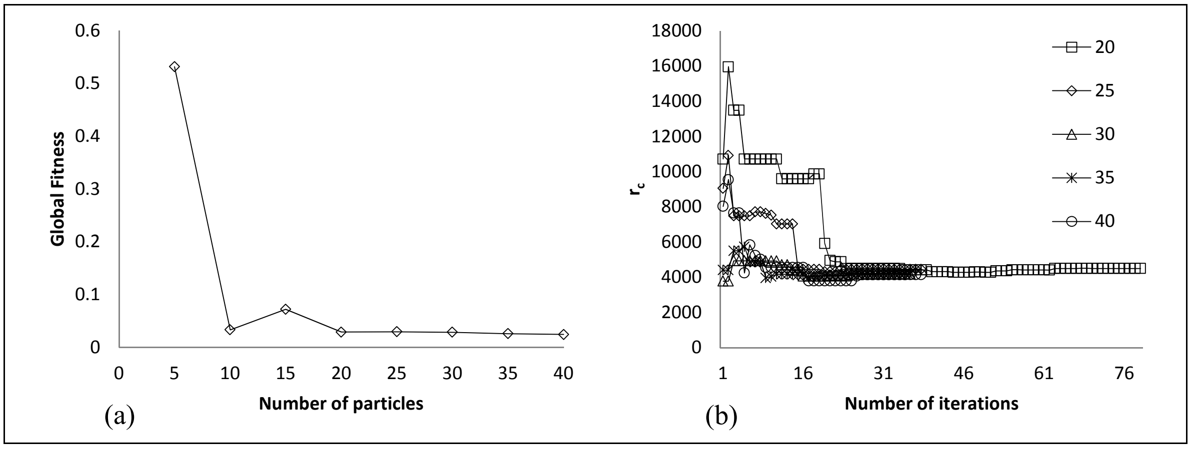

Figure 3.3 Swarm density refinement

Table 3.3 present the optimum values established for r_c, r_r, r_l and the three lubricants of Table 3.2. These results represent the constituent values for the preparation of the design formulas described in the next section.

Table 3.3 Optimum design variables

	r_c					r_r					r_l				
	W ($\times 10^{-5}$)					W ($\times 10^{-5}$)					W ($\times 10^{-5}$)				
	1.63	3.66	6.5	10.2	14.6	1.63	3.66	6.5	10.2	14.6	1.63	3.66	6.5	10.2	14.6
S_l	lubricant ISO-VG 100														
0.2	19917.7	18026.8	8868.3	6628.6	4258.5	2.944	78.494	12.885	29.987	11.833	0.0235	0.0843	0.0424	0.0809	0.0589
0.4	17390.8	8574.8	4473.0	2677.7	2132.3	28.412	48.696	18.046	12.845	31.966	0.0487	0.0847	0.0643	0.0657	0.1310
0.6	10181.2	5895.6	3266.4	2001.1	1317.3	13.562	42.682	33.787	32.474	10.849	0.0411	0.0912	0.1060	0.1292	0.0817
0.8	7725.8	4284.8	2423.7	1370.5	974.7	12.328	29.507	28.167	10.031	9.936	0.0413	0.0832	0.1062	0.0734	0.0850
1	6973.5	3371.7	1933.4	1128.1	803.6	23.585	36.616	49.857	11.050	16.123	0.0589	0.1070	0.1608	0.0822	0.1220
	lubricant ISO-VG 220														
0.2	19774.0	17698.9	9268.2	6527.0	4332.8	1.458	120.527	20.425	23.105	31.232	0.0153	0.1133	0.0531	0.0703	0.0997
0.4	19041.4	9016.2	4605.1	3147.1	2000.6	24.901	100.754	24.659	24.004	16.148	0.0404	0.1263	0.0757	0.0932	0.0882
0.6	12289.7	5969.0	3305.9	2083.7	1312.6	25.815	75.247	26.839	23.590	8.661	0.0492	0.1264	0.0930	0.1067	0.0721
0.8	8284.7	4329.7	2526.0	1499.9	1051.3	13.941	50.853	34.591	33.191	17.880	0.0416	0.1191	0.1186	0.1451	0.1201
1	7166.4	3472.8	1833.3	1154.7	797.0	24.564	44.150	13.017	11.519	10.465	0.0610	0.1194	0.0733	0.0840	0.0937
	lubricant ISO-VG 460														
0.2	19972.3	19618.9	10887.4	6242.9	4253.6	22.362	132.335	73.008	16.666	9.084	0.0733	0.1082	0.1050	0.0583	0.0502
0.4	14938.7	9105.2	3847.7	3026.7	1948.3	166.076	71.661	12.765	14.986	9.039	0.1578	0.1062	0.0630	0.0715	0.0637
0.6	9929.3	6078.0	3221.1	2042.8	1350.2	122.213	52.396	26.992	22.236	11.945	0.1583	0.1057	0.0953	0.1040	0.0852
0.8	7653.7	4583.9	2486.5	1517.9	1051.1	154.050	44.353	28.030	13.108	15.088	0.1908	0.1063	0.1069	0.0834	0.1080
1	5987.4	3681.1	1943.8	1270.0	809.0	142.411	38.629	23.760	21.270	11.673	0.1964	0.1068	0.1074	0.1196	0.0996

3.7 Optimum profile calculation

The results of Table 3.3 are combined by means of the quadratic Lagrange interpolation functions to predict the optimum profile variables (r_c, r_r and r_l). The two-dimensional version of the functions allows the connection of the constituent values r_c, r_r and r_l obtained for one lubricant viscosity grade, while the one-dimensional variant establishes the relation between the lubricant ISO grades.

Figure 3.4(a) illustrates the node indexing for the one-dimensional shape functions given by Eqs. 3.7-a, b and c. Eqs. 3.8-a, b and c give the evaluations at any given position x' between x'_1 and x'_2, where x' can be W, S_l or η.

$$\Phi_1(x') = \frac{(x' - x'_2)(x' - x'_3)}{(x'_1 - x'_2)(x'_1 - x'_3)} \tag{3.7a}$$

$$\Phi_2(x') = \frac{(x' - x'_1)(x' - x'_3)}{(x'_2 - x'_1)(x'_2 - x'_3)} \tag{3.7b}$$

$$\Phi_3(x') = \frac{(x' - x'_1)(x' - x'_2)}{(x'_3 - x'_1)(x'_3 - x'_2)} \tag{3.7c}$$

$$r_c(x') = \sum_{i=1}^{3} r_{ci} \Phi_i(x') \tag{3.8a}$$

$$r_r(x') = \sum_{i=1}^{3} r_{ri} \Phi_i(x') \tag{3.8b}$$

$$r_l(x') = \sum_{i=1}^{3} r_{li} \Phi_i(x') \tag{3.8c}$$

Figure 3.4(b) describes the node indexing for the two-dimensional shape functions determined from Eqs. 3.7 combined as prescribed by Eq. 3.9, and given by Eqs. 3.10-a, b and c. Eqs. 3.10-a, b and c produce the design variables for a combination of W and S_l.

$$\Phi_{i,j}(W, S_l) = \Phi_i(W)\Phi_j(S_l) \ , \ i, j = 1,2,3 \tag{3.9}$$

$$r_c(W,S_l)=\sum_{i=1}^{3}\sum_{j=1}^{3} r_{ci,j}\Phi_{i,j}(W,S_l) \tag{3.10a}$$

$$r_r(W,S_l)=\sum_{i=1}^{3}\sum_{j=1}^{3} r_{ri,j}\Phi_{i,j}(W,S_l) \tag{3.10b}$$

$$r_l(W,S_l)=\sum_{i=1}^{3}\sum_{j=1}^{3} r_{li,j}\Phi_{i,j}(W,S_l) \tag{3.10c}$$

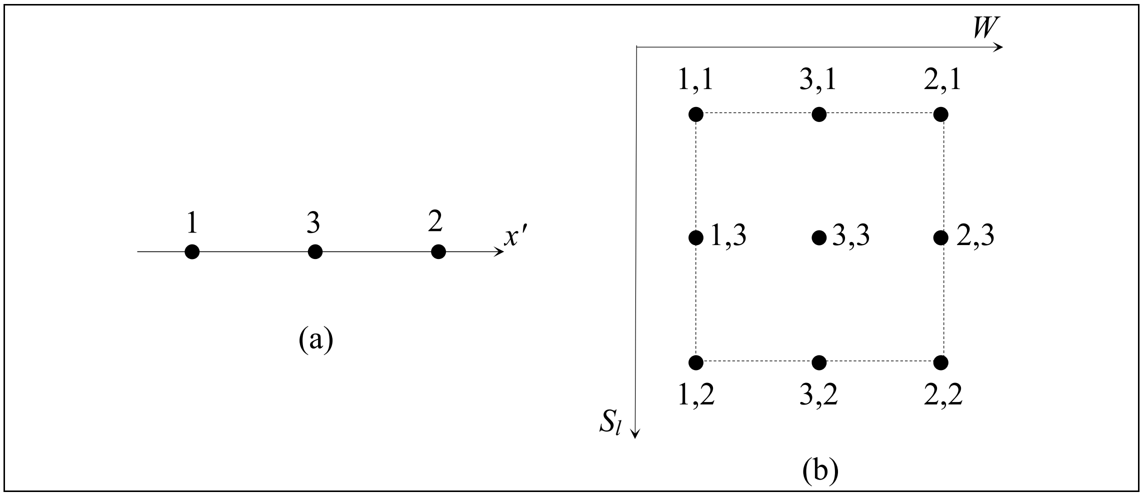

Figure 3.4 Node indexing for quadratic Lagrange shape function, (a) 1-D, (b) 2-D

The calculation procedure for selected *W*, S_l and η involves the following steps: 1- Evaluation of r_c, r_r and r_l for the three lubricants, Eqs. 3.10-a, and c; 2- One-dimensional evaluation through the viscosity ISO grades with respect to η by means of Eqs. 3.8-a, b and c.

3.8 Validation

This section compares the roller profiles predicted with the help of the formulas to the optimum profiles established with PSO. This comparison integrates the four test points indicated in Figure 3.5 for selected *W* and S_l. Since Eqs. 3.10-a, b and c account for nine constituent values at a time, the (W, S_l) domain is divided into four subareas. The validation points are thus selected in each subarea: Case 1 ($W = 2.34\times10^{-5}$and $S_l = 0.5$), Case 2 ($W = 12.7\times10^{-5}$ and $S_l = 0.3$), Case 3 ($W = 4.7\times10^{-5}$and $S_l = 0.9$) and Case 4 ($W = 8.6\times10^{-5}$and $S_l = 0.7$). The validation procedure encompasses two levels: first, the precision obtained with the two-dimensional Lagrange functions when varying *W* and S_l is evaluated for a constituent lubricant, and Cases 1 to 4 are examined for the ISO-VG 100 lubricant. Secondly, the one-dimensional Lagrange functions predictions are appraised when testing Cases 1 to 4 with two extraneous lubricants ISO-VG 150 and 320 selected in between the three constituent lubricants. The considered lubricant viscosities are given in Table 3.4.

Table 3.4 Tested lubricant viscosities (Pa s)

	ISO VG	
Temperature (K)	150	320
313	0.13350	0.28480
373	0.01310	0.02145

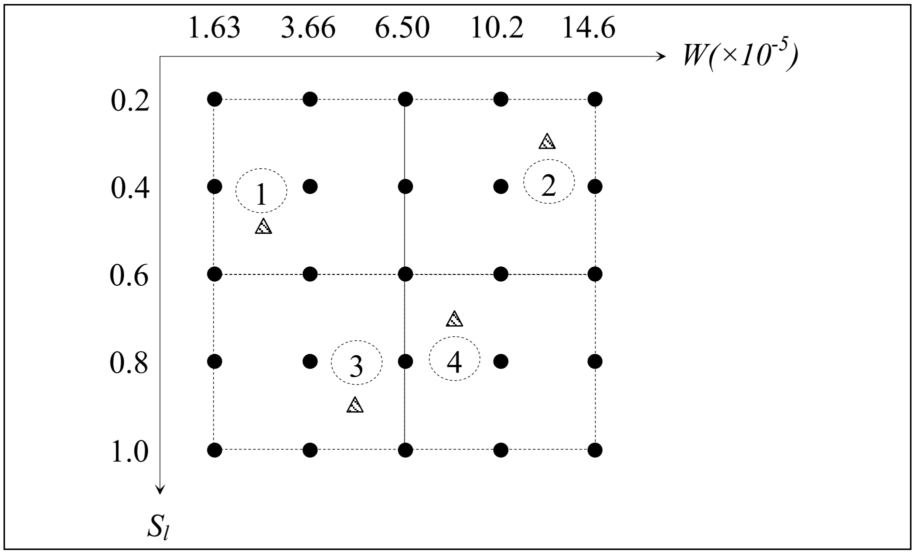

Figure 3.5 Validation points

Table 3.5 shows the design variable values predicted with Eqs. 3.10 and evaluated with the PSO approach for the lubricant ISO 100. For r_c the maximum deviation (-6.6%) appears with Case 1. On the other hand, while with Cases 2 and 4 the precision remains excellent for all three design variables, a rapid analysis of the values of Table 3.3 shows that S_l changes have strong impacts on r_r and r_l when W is lower than 6.5x10^{-5}. The table inspection also indicates and that the design variable response presents high-order variations. Therefore, the quadratic Lagrange functions can only assure a limited precision. Consequently, Cases 1 and 3 show noticeable r_r and r_l relative deviations. Nevertheless, the accuracy level could be improved by a simple additional subdivision of the domain below $W = 6.5\text{x}10^{-5}$. On the other hand, Figure 3.6 draws the pressure and film thickness axial distributions established for these first four cases. The curves clearly indicate that the imprecision observed on r_r and r_l in Cases 1 and 3 has no disadvantageous influence on the resulting pressure distributions and film thickness behavior. In addition, Table 3.5 presents the pressure spike to the central pressure and the axial film constriction to the central film thickness ratios. The pressure ratio values are all very close to 1, while the film ratios remain higher than 76%, even for Case 2, which corresponds to the highest load case (1.4 GPa).

Table 3.5 Lubricant ISO-VG 100

	Case 1			Case 2			Case 3			Case 4		
	PSO	Model	Devia. (%)	PSO	Model	Devia. (%)	PSO	Model	Devia. (%)	PSO	Model	Devia. (%)
r_c	11319.7	10570.4	-6.6	3327.0	3418.6	2.8	2748.8	2883.8	4.9	2079.9	2024.7	-2.7
r_r	116.872	36.880	-68.5	21.404	22.054	3.0	12.370	33.642	172.0	24.572	21.966	-10.6
r_l	0.1204	0.0694	-42.4	0.0887	0.0874	-1.5	0.0610	0.1063	74.3	0.1072	0.0967	-9.8
P_{spike}/P_0	1.000	1.001	-	1.004	1.004	-	1.001	0.997	-	1.000	0.998	-
$H_{const.}/H_c$	1.000	0.999	-	0.998	0.761	-23.7	0.995	0.999	-	0.998	0.816	-18.2

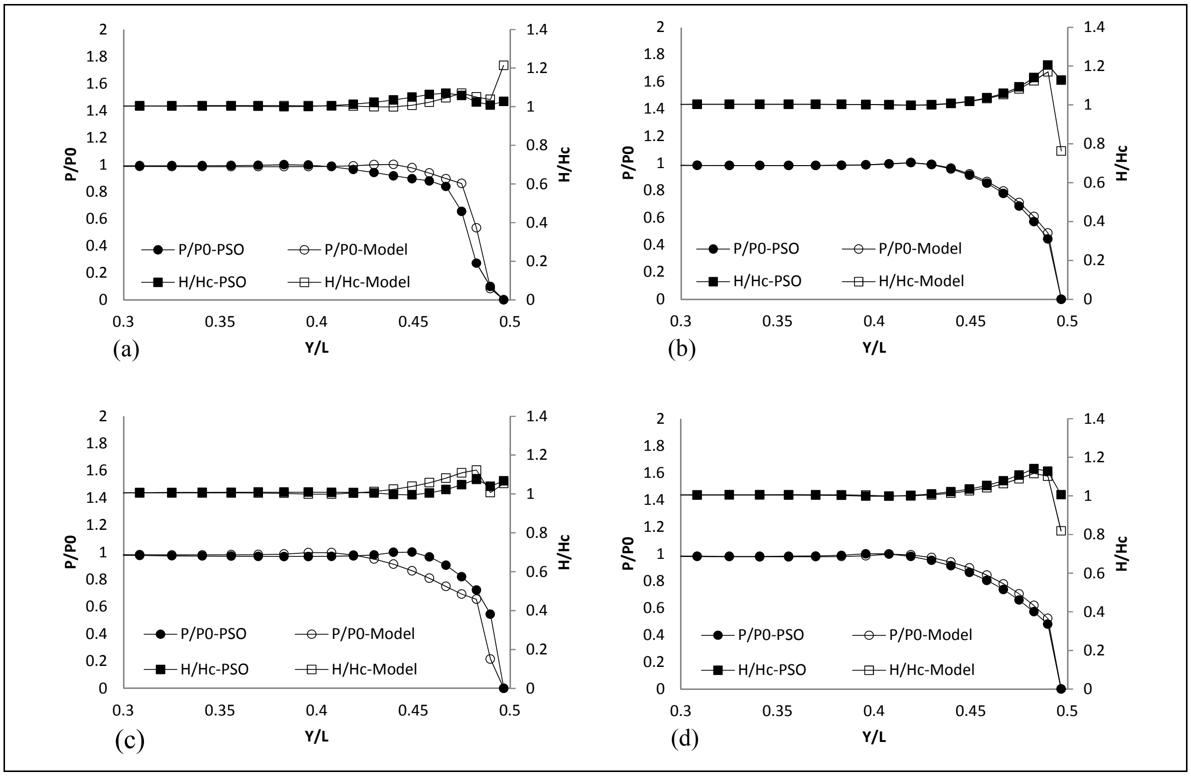

Figure 3.6 Pressure and film thickness, lubricant ISO-VG 100,
(a) Case 1, (b) Case 2, (c) Case 3, (d) Case 4

Table 3.6 presents the results for the four cases and the lubricant ISO-VG 150. The values of r_c are evaluated with a precision greater than 85%. A pattern of deviation similar to the previous one appears for r_r and r_l, with the maximum deviation occurring for r_r. Figure 3.7 presents the pressure and film thickness distributions. Again, all pressure distributions appear to be smooth and practically uniform, while the film thickness reveals no significant reduction at the contact limit. The P_{spike}/P_0 and H_{const}/P_c ratios given in Table 3.6 better illustrate the response quality. In reality, the curves of Figures 3.6 and 3.7 expose the effectiveness of the predicted r_c, r_r and r_l, and what is even more important, reveal the robustness of the model; the established variable values correspond to suitable profile corrections, although they are not exactly equal to the real PSO evaluations.

Table 3.6 Lubricant ISO-VG 150

	Case 1			Case 2			Case 3			Case 4		
	PSO	Model	Devia. (%)	PSO	Model	Devia. (%)	PSO	Model	Devia. (%)	PSO	Model	Devia. (%)
r_c	11310.7	11259.8	-0.5	3039.5	3490.5	14.8	2840.3	2889.0	1.7	2020.8	2089.4	3.4
r_r	101.890	50.001	-50.9	17.005	23.263	36.8	16.615	39.496	137.7	19.401	29.048	49.7
r_l	0.1120	0.0799	-28.7	0.0773	0.0903	16.8	0.0700	0.1157	65.3	0.0949	0.1179	24.2
P_{spike}/P_0	1.000	1.002	-	1.000	1.004	-	1.000	0.998	-	1.000	1.000	-
$H_{const.}/H_c$	1.000	0.999	-	0.999	0.847	-15.2	0.997	0.988	-	0.998	0.999	-

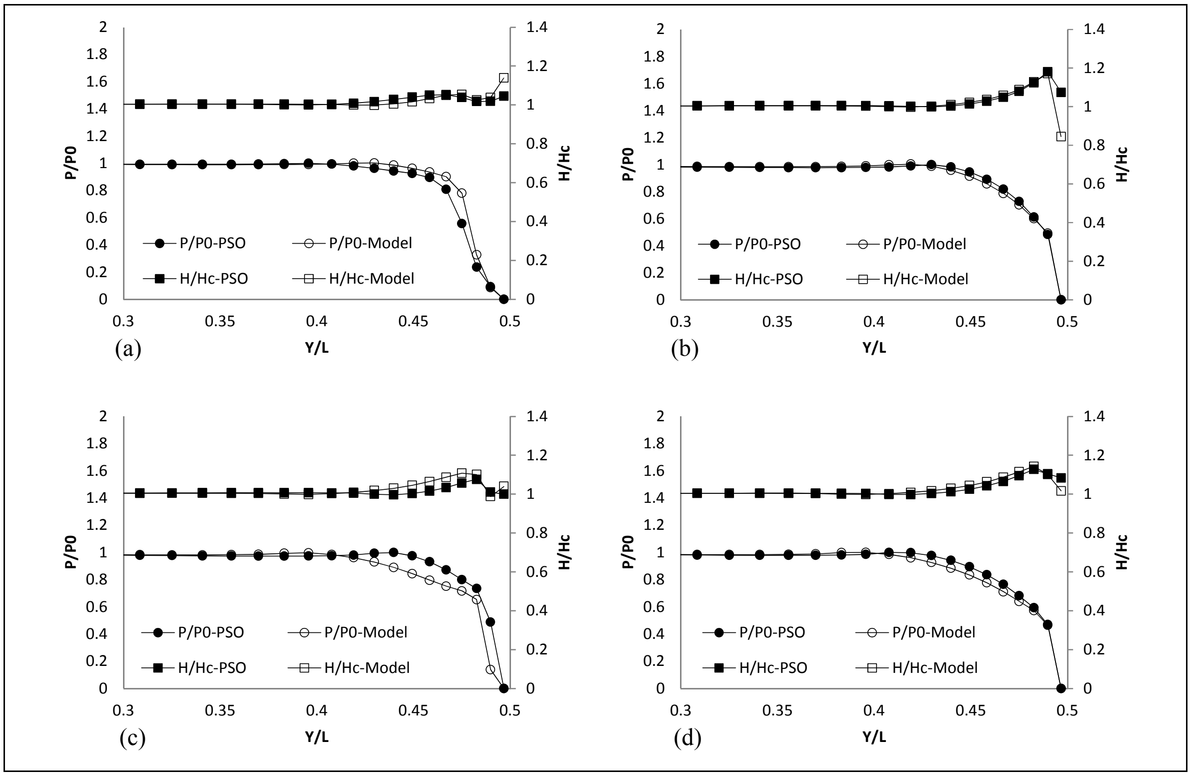

(a) (b) (c) (d)

Figure 3.7 Pressure and film thickness, lubricant ISO-VG 150,
(a) Case 1, (b) Case 2, (c) Case 3, (d) Case 4

Table 3.7 gives the results obtained with the lubricant ISO-VG 320. As before, r_c is evaluated with a better precision (more than 80%). The maximum deviations appear under Case 1 conditions with 240% and 110% for r_r and r_l, respectively. Nevertheless, as for the previous ISO-VG, the pressure and film thickness ratios given in Table 3.7 as well as the pressure distributions and film thicknesses presented in Figure 3.8 demonstrate the effectiveness of the suggested profile corrections. While the agreement between the prediction model and the PSO curves confirm the model robustness, the differences between the predicted r_r and r_l and the real optimal values indicate that r_c is the controlling variable, whereas the rounded corner definition plays a complementing role. Since the precision observed for r_c remained high for all validation tests, it can be concluded that the proposed model offers profile corrections producing optimized forms.

Table 3.7 Lubricant ISO-VG 320

	Case 1			Case 2			Case 3			Case 4		
	PSO	Model	Devia. (%)	PSO	Model	Devia. (%)	PSO	Model	Devia. (%)	PSO	Model	Devia. (%)
r_c	9795.4	11715.3	19.6	3148.6	3550.6	12.8	3111.9	3004.7	-3.4	2119.3	2183.7	3.0
r_r	26.217	89.321	240.7	13.850	20.268	46.3	40.543	41.910	3.4	34.931	35.111	0.5
r_l	0.0544	0.1139	109.4	0.0702	0.0833	18.7	0.1191	0.1216	2.1	0.1295	0.1365	5.4
P_{spike}/P_0	1.000	1.002	-	1.000	1.004	-	1.000	0.999	-	1.000	1.005	-
$H_{const.}/H_c$	1.000	0.999	-	0.998	0.897	-10.1	0.999	0.999	-	0.999	0.998	-

3.9 Conclusion

In the absence of profile correction, cylindrical rolling contacts develop pressure concentrations near the roller extremities. Crowning modifications are therefore often incorporated to eliminate the pressure spikes at the contact limits. However, under heavy loads, this profile modification does not generally generate the desired pressure flattening. Recently, the authors of the present work demonstrated that crowning modifications combined with rounded corners could result in uniform contact pressure distributions. This paper presents formulas for the rapid design of optimal profiles. The proposed analysis assumes that an optimal profile correction maximizes the load capacity and assures uniform contact pressure distributions as well as nearly constant film thicknesses along the contact line. The developed formulas amalgamate effective results obtained from multi-objective particle swarm optimizations (PSO) completed over a five-level dimensionless factorial design, with the factors being the slenderness, the load and the lubricant viscosity.

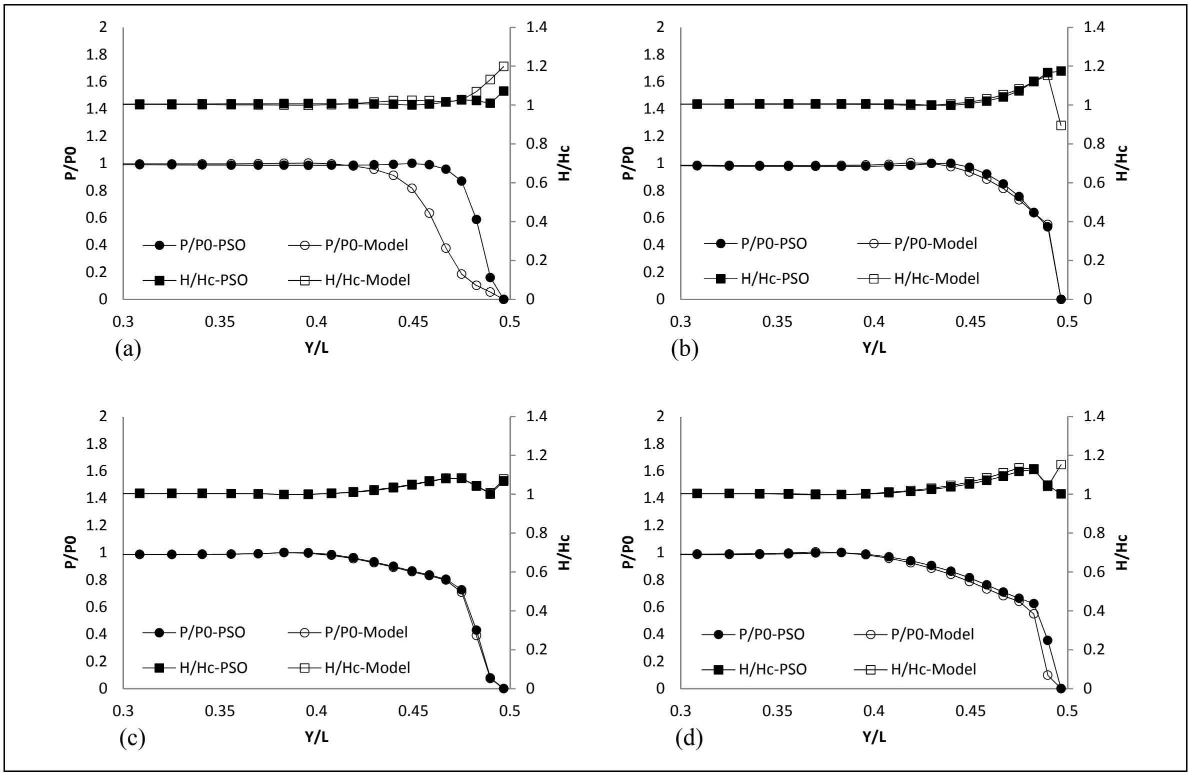

Figure 3.8 Pressure and film thickness, lubricant ISO-VG 320, (a) Case 1, (b) Case 2, (c) Case 3, (d) Case 4

Three dimensionless design variables define the roller profile corrections: the crowning radius (r_c), the rounding radius (r_r) and the length of the rounded corner (r_l). The validation section of the study compared the design variable evaluations produced with the formulas to the real PSO calculated values. Globally, the analysis showed that r_c has a decisive influence on the final pressure and film thickness distributions, while r_r and r_l make complementary contributions. The comparison also demonstrated that, although the r_r and r_l formula predictions and PSO values could be significantly different, the r_c evaluations were in close agreement for all tested conditions. Moreover, considering that the test points were all located at positions chosen in between the formula constituent points, the reported precision estimates virtually describe the lowest accuracy positions of the model. On the other hand, when complemented by the simulated physical response of the corrected rollers, showing that the pressure distributions and film thickness behavior exhibit the desired smoothness, the presented results illustrate the robustness of the design variable estimates, even though no detailed analysis of this aspect was conducted during the present study. In reality, the tested points indicate that the optimal values established with PSO to generate the formulas are presumably situated in low curvature zones of the search space; the optimization algorithm found areas of optimal behavior more than unique positions situated at pointed maxima. Therefore, variations of the predicted r_r and r_l in the optimal areas still guarantee efficient profile corrections. Consequently, the developed prediction model represents a powerful design tool for optimal profile correction of cylindrical rolling contacts.

CONCLUSION

Rolling contact elements, such as gears and bearings are prone to contact fatigue damages. Their non-conforming contact surfaces repeatedly expose to extreme contact pressures, leading to nucleation of fatigue cracks over the surface or subsurface regions, where micro cracks propagate during the course of operation and eventually result in surface material losses. In many of these elements contact happens along a line with finite length. As described at the beginning of this thesis, this type of contact presents stress concentration near the free boundaries which is usually being reduced by providing an axial crowning in order to evenly distribute the load over the complete contact length. Nevertheless, lubricants are used to separate the contact surfaces by a viscous oil film; the so called elastohydrodynamic lubrication (EHL) which is an important controlling agent in surface degradation. Although experimental investigations demonstrated strong influence of free edges on the EHL behavior of finite line contacts, the effects of free boundaries on contact stress distribution and EHL characteristics in such problems remain unknown. Few studies have investigated the EHL of finite line contacts, but their solution was based on half-space theory which is unable to describe the situation near the contact extremities. Therefore, this thesis presents an EHL model integrating a correction procedure extracted from elastic quarter-space model and investigates the edge influence on pressure, oil film thickness and temperature, and stress distribution of finite line contacts.

In terms of first global objective, the present research began with the development of a 3D numerical model for general lubricated contacts which is addressed in chapter 1. The resulting model incorporates finite difference expansion of energy and Reynolds equations over solution domain and solves them simultaneously while accounting for elastic deformation and pressure-dependent lubricant properties. The model also uses the Carreau expression to integrate non-Newtonian lubricant responses. However, computational instability is a major challenge encountered when solving such a system of equations. This problem emerges mainly from high sensitive interconnected pressure-dependent variables, where their rapid fluctuation can lead to divergent iterations especially at high pressures. In order to achieve a stable solution, the model distributes a finite difference expansion of the Couette term of the Reynolds equation over successive iterations during the solution process. This technique provides smooth transition from previous converged iteration to the current step. As a result, a very stable and precise model is obtained which is capable of addressing thermal EHL problems with extreme loads.

As a scientific contribution, the model integrates free boundary influence by means of a corrective procedure that applies a mirrored load multiplied by Guilbault's factor. In fact, the model effectively eliminates shear and normal stresses from traction-free boundaries, while offering a fast and precise simulation of general non-Hertzian lubricated contacts. Furthermore, a comparison with experimental and numerical results obtained from the literature validates the accuracy of the proposed model.

Chapter 1 also presents an investigation of the consequences of profile modifications in the EHL of finite line contacts. In other words, the influence of different roller profile corrections on film thickness, pressure and temperature distributions was established using the developed EHL model. Seven common roller profiles and contact conditions were investigated with and without free-edge correction (i.e., using the corrected and non-corrected model). The fallout of this section revealed the significant consequence of incomplete treatment of free boundaries. A few examples can help clarifying the picture. The non-corrected model predicted a film breakdown and metal-to-metal contact at the contact edge of a chamfered roller; by contrast, under the corrected model, the chamfered roller surface continued to preserve a thin film along the complete contact line even in the context of considerable constriction. When the corrected model is applied to the contact between two straight rollers with non-coincident ends, the evaluated pressure at the constriction position is reduced by approximately 50% as compared to the pressure produced under the non-corrected model. On the other hand, in the case of coincident ends, the non-corrected model produced nearly a 310% overestimation of edge pressure as compared to the corrected model. Eventually, the boundary effects identified in the study suggest that the corrected model is a reliable tool that enhances our ability to accurately describe finite line contacts under the EHL condition.

Among the seven different roller profiles investigated in this study, two profiles—the logarithmic profile and a crowning modification with rounded corners—produce the most uniform pressure distributions along the contact line. Furthermore, a crowned roller with rounded corners offers a more uniform film thickness across the contact line. This latter finding suggests an interesting fact; the most effective profile adjustment would be a large crowning radius combined with a rounding radius at the corners.

In chapter 2, free boundary correction concept is extended to tridimensional contact stress evaluation. The developed model for stress field calculation is on the basis of closed-form expressions from half-space theory, coupled with free-edge correction which offers a rapid and accurate evaluation of surface and subsurface stress distributions. The extended corrective procedure developed for stress field calculations is as follows. By defining the z axis as normal to the contact surface, with y along the axial direction and x along the rolling direction, virtual mirrored pressures were used to account for the free boundary influence on displacement, and were also integrated into the σ_{zz}, σ_{yz} and σ_{yx} evaluations. The normal stress component at the free boundary σ_{yy} was simply set to zero. The proposed procedure also associates the evolution of σ_{yy} from plain strain at mid-section to a plane stress condition close to the free boundary. The analysis of edge contact impacts on surface and subsurface stress distributions demonstrates that the normal stress component σ_{yy} follows an arc-form reduction from its central value towards zero at the free surface. Accordingly, the investigation suggested a radius equal to 15 times the contact width and validated through FEM analyses.

Once the complementary model for stress field evaluations was established, validation was completed through a two-level factorial comparison constructed with three dimensionless factors: contact slenderness, contact length ratio, and load. The domain under consideration included short and long rollers, coincident and non-coincident end conditions, and loads corresponding to maximum Hertzian pressures of 200 and 600 MPa. Comparison of σ_{xx}, σ_{zz} and $\tau_{\max}$ at mid-section revealed a greater-than-96% correspondence between the newly developed model and the FEM reference results, while the correlation for σ_{yy} remained greater than 89%. At the free boundary, distributions of σ_{zz} and $\tau_{\max}$ obtained by the model also showed a greater-than-90% coherence with the FEM simulations. In the case of non-coincident ends, internal stresses σ_{zz} and $\tau_{\max}$ at positions beneath the free edge of the shorter roller presented a minimum value of 88% conformity with FEM results. As a matter of fact, the proposed model provides accuracy and speed at the same time. Since, contact pressure distribution and associated stresses are evaluated at least 125 times faster than when using the FEM.

Developing formulas for rapid design of optimal roller profiles was the final step of this research which is addressed in chapter 3. The study assumes that an optimum profile modification should maximize load-carrying capacity while assuring a uniform distribution of contact pressure as well as near-constant film thickness along the contact line. As concluded in chapter 1, a crowning modification combined with rounded corners can generate uniform film thickness and pressure distribution similar to that of logarithmic profile. Accordingly, chapter 3 concentrates on the crowned form profile which is defined along three dimensionless design variables: crowning radius r_c, rounding radius r_r and rounded corner length r_l. A five-level dimensionless factorial design with the factors *slenderness, load, and lubricant viscosity* was used as the basis for a series of particle swarm optimizations (PSO). The proposed formulas incorporated the effective results obtained from the multi-objective PSO to determine roller profile for any combination of slenderness, load and lubricant viscosity inside the studied domain.

The validation section of the last step compared the design variables evaluated by the proposed formulas to the values obtained from PSO alone. Analyses demonstrated the crucial influence of r_c on final pressure and film thickness distributions, while r_r and r_l were shown to have complementary roles. Actually, the value for r_c predicted for all test conditions by the proposed formulas corresponded closely to the value produced by the PSO, while the values for r_r and r_l showed considerable discrepancy in some cases. On the other hand, comparison of pressure and film thickness distributions for all test cases revealed that, despite some deviation in the values of r_r and r_l, the resultant physical response possessed the desired smoothness; this finding confirms the robustness of the design variable estimation. In fact, primary optimal values from the PSO establishing the formulas are apparently found in low curvature zones of search space. In other words, the optimization algorithm identified an area of optimal values rather than single optima. Thus, variations of r_r and r_l do not detract from the development of efficient profile modifications.

Through accomplished objectives, this research work contributed into understanding the behavior of finite line contacts subjected to EHL conditions. The origin of edge contact effects was studied by numerical modeling. The outcome of this thesis is a novel and powerful model which is capable to describe the EHL characteristics all over the contact zone, including discontinuities. In addition, a new design tool for optimal profile correction of cylindrical rolling elements under EHL regime was also presented. Industries dealing with the applications such as gears, cams, bearings and wheel-rails can be served by the research outline suggested in this thesis.

RECOMMENDATIONS

This section presents some recommendations for future work based on the results obtained in this research.

From the results of Chapter 1, the lubricant temperature is shown to increase rapidly in proportion to slip ratio. Lubricant shear heating induces a heat flux over the contact surface which conducts inward to each roller over the time. Roller surface exposes shortly to the heat flux when passing through contact, where it generates sharp temperature gradient near the contact surface. Thus, materials at the vicinity of contact zone expand more than in depth areas, which might result in a tiny bump. This surface evolution from heat expansion will change pressure and film thickness distribution. Hence, as a next step, the current EHL model could further be developed integrating thermo-elastic effects.

The level of subsurface stresses is also affected by localized thermal expansion of solids. Once a thermo-elastic model establishing the evolved pressure distribution is obtained, it is recommended that the variation of subsurface stresses because of material expansion gradient at different depths be investigated.

The current research has assumed no roughness or surface deteriorations. An interesting topic for future studies is the potential effect of pitting over the contact surface. Surface pits are generated from contact fatigue, and once they grow to a certain size, failure occurs. Therefore, machine elements run with small surface pits before being changed. Further studies are needed to evaluate the impact of pits of different sizes on the EHL characteristics such as pressure distribution and lubricant film shape.

LIST OF BIBLIOGRAPHICAL REFERENCES

Ahmadi, N., L. M. Keer, T. Mura et V. Vithoontien. 1987. « The interior stress field caused by tangential loading of a rectangular patch on an elastic half space ». *Transactions of the ASME. Journal of Tribology,* vol. 109, n° 4, p. 627-9.

Bahadoran, H., et R. Gohar. 1974. « Research note: end closure in elastohydrodynamic line contact ». *Journal of Mechanical Engineering Science,* vol. 16, n° 4, p. 276-278.

Bold, P. E., M. W. Brown et R. J. Allen. 1992. « A review of fatigue crack growth in steels under mixed mode I and II loading ». *Fatigue & Fracture of Engineering Materials & Structures,* vol. 15, p. 965-77.

Chakraborty, I., Vinay K., Shivashankar B. N. et Rajiv T. 2003. « Rolling element bearing design through genetic algorithms ». *Engineering Optimization,* vol. 35, n° 6, p. 649-659.

Chen, X. Y., S. Q. Zhou et J. J. Ma. 1997. « Oil film thickness and shape in Lundberg's profile roller contacts ». In *Tribology Series*, sous la dir. de D. Dowson, C. M. Taylor T. H. C. Childs G. Dalmaz Y. Berthier L. Flamand J. M. Georges, et A. A. Lubrecht. Vol. Volume 32, p. 415-422. Elsevier.

Chen, X., X. Shen, W. Xu et J. Ma. 2001. « Elastohydrodynamic lubrication of logarithmic profile roller contacts ». *Chinese Journal of Mechanical Engineering (English Edition),* vol. 14, n° 4, p. 347-352.

Chen, X., Haoyang S. et Xuejin S. 2006. « Review and Prospects for the Development of EHL of Finite Line Contacts ». In *IUTAM Symposium on Elastohydrodynamics and Micro-elastohydrodynamics*, sous la dir. de Snidle, R. W., et H. P. Evans. Vol. 134, p. 95-106.

Cheng-San, Y., Chuang L., Ke C. et Yang C. 2008. « Comparative particle swarm optimization (CPSO) for solving optimization problems ». In *2008 IEEE International Conference on Research, Innovation and Vision for the Future in Computing and Communication Technologies (RIVF 2008), 13-17 July 2008.* (Piscataway, NJ, USA), p. 86-90.

Cioc, C. 2004. « An elastohydrodynamic lubrication model for helicopter high-speed transmission components ». *PhD thesis, The University of Toledo.*

Clerc, M., et J. Kennedy. 2002. « The particle swarm - explosion, stability, and convergence in a multidimensional complex space ». *IEEE Transactions on Evolutionary Computation,* vol. 6, n° 1, p. 58-73.

de Mul, J. M., J. J. Kalker et B. Fredriksson. 1986. « The contact between arbitrarily curved bodies of finite dimensions ». *Transactions of the ASME. Journal of Tribology Technology,* vol. 108, p. 140-8.

Dong, Z., Ren N. et Q. J. Wang. 2009. « Pitting life prediction based on a 3D line contact mixed EHL analysis and subsurface von mises stress calculation ». *Journal of Tribology,* vol. 131, n° 4, p. 041501 (8 pp.).

Dowson, D., et G. R. Higginson. 1959. « Numerical solution to elasto-hydrodynamic problem ». *Journal of Mechanical Engineering Science,* vol. 1, n° 1, p. 6-15.

Eberhart, R., et J. Kennedy. 1995. « A new optimizer using particle swarm theory ». In *MHS'95. Proceedings of the Sixth International Symposium on Micro Machine and Human Science, 4-6 Oct. 1995*. (New York, NY, USA), p. 39-43.

Elsharkawy, A. A., et B. J. Hamrock. 1991. « Subsurface stresses in micro-EHL line contacts ». *Journal of Tribology,* vol. 113, n° 3, p. 645-655.

Engelbrecht, A.P. 2007. *Computational Intelligence: An Introduction*. Wiley.

Evans, C. R., et K. L. Johnson. 1986a. « Regimes of traction in elastohydrodynamic lubrication ». *Proceedings of the Institution of Mechanical Engineers. Part C. Mechanical engineering science,* vol. 200, p. 313-324.

Evans, C. R., et K. L. Johnson. 1986b. « Rheological properties of elastohydrodynamic lubricants ». *Proceedings of the Institution of Mechanical Engineers. Part C. Mechanical engineering science,* vol. 200, n° C5, p. 303-312.

Gohar, R., et A. Cameron. 1963. « Optical Measurement of Oil Film Thickness under Elasto-hydrodynamic Lubrication ». *Nature,* vol. 200, n° 4905, p. 458-459.

Gohar, R., et A. Cameron. 1967. « The Mapping of Elastohydrodynamic Contacts ». *A S L E Transactions,* vol. 10, n° 3, p. 215-225.

Guilbault, R. 2011. « A fast correction for elastic quarter-space applied to 3D modeling of edge contact problems ». *Journal of Tribology,* vol. 133, (10 pp.).

Guilbault, R. 2013. « A Simplified Thermal Analysis of Elastohydrodynamic Contacts ». *Journal of Tribology,* vol. 135(2).

Gupta, S., Rajiv T. et Shivashankar B. N. 2007. « Multi-objective design optimisation of rolling bearings using genetic algorithms ». *Mechanism and Machine Theory,* vol. 42, n° 10, p. 1418-1443.

Hamrock, B., et William J. 1983. « Rolling element bearings ». *NASA Reference Publication.*

Hartnett, M. J. 1980. « General numerical solution for elastic body contact problems ». *American Society of Mechanical Engineers, Applied Mechanics Division, AMD,* vol. 39, p. 51-66.

Hartnett, M. J., et J. W. Kannel. 1981. « Contact stresses between elastic cylinders: a comprehensive theoretical and experimental approach ». vol. 103, n^o 1, p. 40-5.

Hetenyi, M. 1960. « A Method of Solution for the Elastic Quarter-Plane ». *Journal of Applied Mechanics,* vol. 27, n^o 2, p. 289-296.

Hetényi, M. 1970. « A general solution for the elastic quarter space ». *Transactions of the ASME. Series E, Journal of Applied Mechanics,* vol. 37, p. 70-6.

Hirani, H, K Athre et S Biswas. 2000. « Comprehensive design methodology for an engine journal bearing ». *Proceedings of the Institution of Mechanical Engineers, Part J: Journal of Engineering Tribology,* vol. 214, n^o 4, p. 401-412.

Hsu, C., et Rong-Tsong L. 1994. « Efficient algorithm for thermal elastohydrodynamic lubrication under rolling/sliding line contacts ». *Journal of Tribology,* vol. 116, n^o 4, p. 762-769.

Ioannides, E., G. Bergling et A. Gabelli. 1999. « Analytical formulation for the life of rolling bearings ». *Acta Polytechnica Scandinavica, Mechanical Engineering Series*, n^o 137, p. 6-80.

Johns, P. M., et R. Gohar. 1981. « Roller bearings under radial and eccenteric loads ». *Tribology International,* vol. 14, n^o 3, p. 131-136.

Johnson, K. L. 1987. *Contact mechanics*. Cambridge University Press.

Kalker, J. J. 1986. « Numerical calculation of the elastic field in a half-space ». *Communications in Applied Numerical Methods,* vol. 2, n^o 4, p. 401-410.

Kennedy, J., et R. Eberhart. 1995. « Particle swarm optimization ». In *Proceedings of ICNN'95 - International Conference on Neural Networks, 27 Nov.-1 Dec. 1995*. (New York, NY, USA) Vol. vol.4, p. 1942-8.

Kumar, K. S., R. Tiwari et P. V. V. Prasad. 2009. « An optimum design of crowned cylindrical roller bearings using genetic algorithms ». *Journal of Mechanical Design,* vol. 131, n^o 5, p. 051011 (14 pp.).

Kuroda, S., et K. Arai. 1985. « Elastohydrodynamic lubrication between two rollers (finite width analysis) ». *Bulletin of the Japan Society of Mechanical Engineers,* vol. 28, n^o 241, p. 1367-72.

Kushwaha, M., H. Rahnejat et R. Gohar. 2002. « Aligned and misaligned contacts of rollers to races in elastohydrodynamic finite line conjunctions ». *Proceedings of the Institution of Mechanical Engineers, Part C: Journal of Mechanical Engineering Science,* vol. 216, n^o 11, p. 1051-1070.

Lee, R., et Chao-Ho H. 1993. « Fast method for the analysis of thermal-elastohydrodynamic lubrication of rolling/sliding contacts ». *Wear,* vol. 166, n^o 1, p. 107-117.

Littmann, W. E., et R. L. Widner. 1965. « Propagation of contact fatigue from surface and subsurface origins ». In *ASME Meeting CF-2, Nov 7-11 1965*. (New York, NY, United States), p. 12.

Liu, X., et Peiran Y. 2002. « Analysis of the thermal elastohydrodynamic lubrication of a finite line contact ». *Tribology International,* vol. 35, n^o 3, p. 137-144.

Love, A. E. H. 1929. « Stress produced in a semi-infinite solid by pressure on part of the boundary ». *Philosophical Transactions of the Royal Society of London,* vol. 228, p. 377-420.

Lubrecht, A.A. 1987. « The Numerical Solution of the ElastoHydrodynamically Lubricated Line and Point Contacts, using MultiGrid Techniques ». *Ph.D. Thesis, University of Twente*.

Lugt, P. M., et G. E. Morales-Espejel. 2011. « A Review of Elasto-Hydrodynamic Lubrication Theory ». *Tribology Transactions,* vol. 54, n^o 3, p. 470-496.

Lundberg, G., et A. Palmgren. 1947. « Dynamic capacity of rolling bearings ». *Ingeniors Vetenskaps Akademien - Handlingar*, n^o 196, p. 50.

Lundberg, G., et A. Palmgren. 1949. « Dynamic capacity of rolling bearings ». *Engineers' Digest (British Edition),* vol. 10, n^o 1, 4.

M'Ewen, E. 1949. « XLI. Stresses in elastic cylinders in contact along a generatrix (including the effect of tangential friction) ». *Philosophical Magazine Series 7,* vol. 40, n^o 303, p. 454-459.

Maday, C. J. 1970. « Maximum principle approach to the optimum one-dimensional journal bearing ». vol. 92 Ser F, n^o 3, p. 482-489.

Mostofi, A., et R. Gohar. 1983. « Elastohydrodynamic lubrication of finite line contacts ». *Journal of lubrication technology,* vol. 105, p. 598-604.

Najjari, M., et Guilbault R. 2014. « Edge contact effect on thermal elastohydrodynamic lubrication of finite contact lines ». *Tribology International,* vol. 71, n^o 0, p. 50-61.

Nayak, L., et K. L. Johnson. 1979. « Pressure between elastic bodies having a slender area of contact and arbitrary profiles ». vol. 21, n° 4, p. 237-47.

Nélias, D., F. Champiot, D. Girodin, R. Fougéres, L. Flamand, A. Vincent et M. L. Dumont. 1999. « Role of Inclusions, Surface Roughness and Operating Conditions on Rolling Contact Fatigue ». *Journal of Tribology,* vol. 121, n° 2, p. 240-251.

Nikpur K., et Gohar R. 1975. « Profiled taper rollers ». *Tribology International,* vol. 8, n° 5, p. 203-208.

Olver, A. V. 2005. « The mechanism of rolling contact fatigue: An update ». *Proceedings of the Institution of Mechanical Engineers, Part J: Journal of Engineering Tribology,* vol. 219, p. 313-330.

Park, T., et Kyung-Woong K. 1998. « Elastohydrodynamic lubrication of a finite line contact ». *Wear,* vol. 223, n° 1-2, p. 102-109.

Poli, R., J. Kennedy et T. Blackwell. 2007. « Particle swarm optimization ». *Swarm Intelligence,* vol. 1, n° 1, p. 33-57.

Rahnejat, H., et R. Gohar. 1979. « Design of profiled taper roller bearings ». *Tribology International,* vol. 12, n° 6, p. 269-275.

Rajeswara R., B., et Rajiv T. 2007. « Optimum design of rolling element bearings using genetic algorithms ». *Mechanism and Machine Theory,* vol. 42, n° 2, p. 233-250.

Reusner, H. 1986. « Modern Method of Calculation for Designing and Dimensioning Antifriction Bearings ». *Werkstatt und Betrieb,* vol. 119, n° 4, p. 277-282.

Sackfield, A., et D. A. Hills. 1983. « Some useful results in the classical Hertz contact problem ». *The Journal of Strain Analysis for Engineering Design,* vol. 18, n° 2, p. 101-105.

Sadeghi, F., B. Jalalahmadi, T. S. Slack, N. Raje et N. K. Arakere. 2009. « A review of rolling contact fatigue ». *Journal of Tribology,* vol. 131, (15 pp.).

Sadeghi, F., et P. C. Sui. 1990. « Thermal elastohydrodynamic lubrication of rolling/sliding contacts ». *Journal of Tribology,* vol. 112, n° 2, p. 189-195.

Savsani, V., R. V. Rao et D. P. Vakharia. 2009. « Multi-objective design optimisation of ball bearings using a modified particle swarm optimisation technique ». *International Journal of Design Engineering,* vol. 1, n° 4, p. 412-433.

Schoene, T., S. A. Ludwig et R. J. Spiteri. 2012. « Step-optimized Particle Swarm Optimization ». In *2012 IEEE Congress on Evolutionary Computation (CEC), 10-15 June 2012*. (Piscataway, NJ, USA), p. 9 pp.

Seireg, A. 1972. « A Survey of Optimization of Mechanical Design ». *Journal of Engineering for Industry,* vol. 94, n° 2, p. 495-499.

Seireg, A., et H. Ezzat. 1968. « Optimum design of hydrodynamic journal bearings ». In *ASME Meeting WA/Lub-3, Dec 1-5 1968*. p. 8.

Shi, Y., et R. Eberhart. 1998. « A modified particle swarm optimizer ». In *Evolutionary Computation Proceedings, 1998. IEEE World Congress on Computational Intelligence,* p. 69-73.

Smith, J. O., et C. K. Liu. 1954. « Stresses due to tangential and normal loads on elastic solid ». *American Society of Mechanical Engineers - Transactions - Journal of Applied Mechanics,* vol. 12, n° 1, p. 96.

Sourty, E., J. L. Sullivan et M. D. Bijker. 2002. « Numerical modelling of sub-surface stress in magnetic data tape heads due to the dynamic contact with a tape ». *Tribology International,* vol. 35, n° 3, p. 171-184.

Sun, H., et Xiaoyang C. 2006. « Thermal EHL Analysis of Cylindrical Roller Under Heavy Load». IUTAM Symposium on Elastohydrodynamics and Micro-elastohydrodynamics. In, sous la dir. de Snidle, R. W., et H. P. Evans. Vol. 134, p. 107-120.

Sun, H., Xiaoyang C. et Peiran Y. 2004. « Thermal elastohydrodynamic lubrication of cylindrical rollers with crown profiled ends at heavy load ». *Chinese Journal of Mechanical Engineering,* vol. 40, n° 7, p. 99-104.

W., Changsen. 1991. « Analysis of rolling element bearings ». *Mechanical Engineering Publications Ltd, London.*

Wylie, G. M., et C. J. Maday. 1970. « The Optimum One-Dimensional Hydrodynamic Gas Rayleigh Step Bearing ». *Journal of lubrication technology,* vol. 92, n° 3, p. 504-508.

Wymer, D. G., et A. Cameron. 1974. « Elastohydrodynamic lubrication of a line contact ». *Proceedings of the Institution of Mechanical Engineers (London),* vol. 188, n° Compendex, p. 221-238.

Xu, W., Jiaju M. et Xiaoyang C. 1998. « Elastohydrodynamic lubrication of finite line contact (1). Numerical analysis of elastohydrodynamic lubrication for finite cylindrical roller contact ». *Mocaxue Xuebao/Tribology,* vol. 18, n° 1, p. 39-44.

Xue, Y., Tongshu H. et Haoyang S. 2012. « Experimental investigation for finite line contact edge effect of elastohydrodynamic lubrication ». In *2nd International Conference on Advanced Engineering Materials and Technology, AEMT 2012, July 6, 2012*. (Zhuhai, China) Vol. 538-541, p. 1945-1951.

Zhu, D., Jiaxu W., Ning R. et Q. J. Wang. 2012. « Mixed elastohydrodynamic lubrication in finite roller contacts involving realistic geometry and surface roughness ». *Journal of Tribology,* vol. 134, n^{o} 1.

Zhu, D., et Q. J. Wang. 2011. « Elastohydrodynamic Lubrication: A Gateway to Interfacial Mechanics-Review and Prospect ». *Journal of Tribology,* vol. 133, n^{o} 4, p. 041001-14.